Journal of Applied Mathematics

Inverse Fluid Convection Problems in Enclosures

Guest Editors: Fu-Yun Zhao, Di Liu, and Steve H. L. Yim

Inverse Fluid Convection Problems in Enclosures

Journal of Applied Mathematics

Inverse Fluid Convection Problems in Enclosures

Guest Editors: Fu-Yun Zhao, Di Liu, and Steve H. L. Yim

Editorial Board

Contents

Hindawi Publishing Corporation
Journal of Applied Mathematics
Volume 2012, Article ID 850260, 2 pages
doi:10.1155/2012/850260

Editorial

Inverse Fluid Convection Problems in Enclosures

Fu-Yun Zhao,[1,2] Di Liu,[3] and Steve H. L. Yim[4]

[1] *Faculty of Civil Engineering and Geodesy, Technical University Munich, Arcisstr. 21, 80333 Munich, Germany*
[2] *School of Power and Mechanical Engineering, Wuhan University, Luo-Jia-Shan, Wuchang 430072, China*
[3] *College of Pipeline and Civil Engineering, China University of Petroleum, Changjiang Road 66, Qingdaos 266580, China*
[4] *Department of Aeronautics and Astronautics, Massachusetts Institute of Technology, Massachusetts Avenue 77, Cambridge, MA 02139, USA*

Correspondence should be addressed to Fu-Yun Zhao, zfycfdnet@163.com

Received 20 November 2012; Accepted 20 November 2012

Efficiency, security, and reliability of industrial and domestic processes essentially depend on the deep understanding of their actual processes of fluid flow and heat transfer. Actual processes of fluid flow control and measurements need the development of effect-cause inverse modeling. Extensive investigations on the effect-cause inverse modeling could effectively enhance the efficiency, security, and reliability of these industrial and domestic fluid flow processes.

This special issue on the inverse fluid flow compiles 10 papers, merging from different academic disciplines and engineering application backgrounds. Three branches of inverse modeling and application have been discussed. These include inverse identification of pollutant sources, inverse determination of boundary conditions, and inverse measurement of heating devices.

Inverse identification of pollutant source location was addressed in the paper by S. Abe et al., who extended the quasi-reversibility methodology into the situation of airborne pollutant dispersions in the urban street canyons. Timely identification of these pollutant sources could facilitate occupants to evacuate from the dangerous areas.

Unknown boundary conditions always pose the classic modeling of inverse heat transfer and fluid flow. J. Wu et al. employed the hybrid immersed boundary lattice Boltzmann method to determine the unknown heat source term in the immersed boundary, such that the interpolated temperatures accurately satisfy the thermal boundary conditions.

Comparing with the aforementioned theoretical identifications of unknown boundary condition or source information, monitoring and measurement on the transport processes

could involve the noise data and many uncertainties. C. Solisio et al. applied Tikhonov regularization rules to successfully reconstruct the temperature profiles in the landfills of bioreactor with heat recovery fluids measurements.

In addition to the research papers on the inverse modeling and applications, a few papers concerning the direct modeling of industrial multiphase flows, hydrogen-air detonation, square cylinder flows, and convergent channel flows have also been included in this issue. Outlook optimization and process control on these complicated flows will be investigated in the future.

By compiling these papers, we expect that this special issue on inverse flow problems in the industrial and domestic processes could enrich our readers and researchers.

Fu-Yun Zhao
Di Liu
Steve H. L. Yim

Hindawi Publishing Corporation
Journal of Applied Mathematics
Volume 2012, Article ID 465972, 14 pages
doi:10.1155/2012/465972

Research Article

Direct Simulation of Low-Re Flow around a Square Cylinder by Numerical Manifold Method for Navier-Stokes Equations

Zhengrong Zhang and Xiangwei Zhang

School of Materials and Energy, Guangdong University of Technology, Guangzhou 510643, China

Correspondence should be addressed to Zhengrong Zhang, zzr@gdut.edu.cn

Received 15 January 2012; Accepted 3 August 2012

Academic Editor: Fu-Yun Zhao

Numerical manifold method was applied to directly solve Navier-Stokes (N-S) equations for incompressible viscous flow in this paper, and numerical manifold schemes for N-S equations coupled velocity and pressure were derived based on Galerkin weighted residuals method as well. Mixed cover with linear polynomial function for velocity and constant function for pressure was employed in finite element cover system. As an application, mixed cover 4-node rectangular manifold element has been used to simulate the incompressible viscous flow around a square cylinder in a channel. Numerical tests illustrate that NMM is an effective and high-order accurate numerical method for incompressible viscous flow N-S equations.

1. Introduction

In computational fluid dynamics (CFD), Navier-Stokes (N-S) equations for incompressible viscous flow can be solved by several numerical methods generally, such as finite difference method (FDM), finite element method (FEM), and finite volume method (FVM) [1]. The applications of FDM are affected for unsuitability to complicated structure flow field and inconservation of field variables [2]. The FEM schemes for N-S equations are very complicated, and the computational efficiency of nonstandard FEMs is low [3]. FVM is an effective numerical method for solutions of fluid flow, but exact treatments of the moving boundary are difficult and complicated [4]. Furthermore, fractional step algorithms are used to solve velocity and pressure variables unintegratedly in all these numerical methods, and the continuity equation and momentums equations are satisfied, respectively [5]. All the defects of these numerical methods will affect the computational efficiency and accuracy.

Numerical manifold method (NMM) also known as manifold method or finite cover method (FCM) is a generalized numerical method proposed by Shi in the early 1990s [6, 7]. The method performs numerical computation with finite element cover system, which is composed of two independent cover grids: mathematical cover grid and physical cover grid. Mathematical covers define the accuracy of approximate solution, and physical covers determine the solution domain. High accurate numerical manifold schemes for mathematical physics equations can be constructed by adopting different cover functions and cover-weighted functions for physical variables in finite element cover system [8]. The method has been successfully applied in some complicated engineering problems, such as numerical simulation of crack initiation and propagation, damage evolvement of fractured rock masses, coupling vibration, and potential flow problem, and the advantages have been demonstrated in these fields [9–12]. As to fluid flow problems, direct-numerical-solution coupled velocity and pressure variables can be implemented by adopting manifold schemes with mixed cover for N-S equations. The authors have applied numerical manifold method into analyses of unsteady incompressible viscous flow, and the results have illustrated the validity of NMM [13].

Flow around a square cylinder is a typical model to validate the performance of numerical methods for solution of incompressible viscous N-S equations. The flow structure has been investigated experimentally and numerically. Experimental investigations have shown that the flow characteristic is different at different Reynolds numbers [14]. FVM, FDM, and others numerical methods have been applied to simulate the flow around a square cylinder, the detail results have been obtained and met the experimental results [15–17]. The experimental and numerical results have been employed to validate the numerical methods in CFD as benchmarks.

In this paper, numerical manifold schemes of direct solutions coupled velocity and pressure for N-S equations were constructed and applied to analyze incompressible viscous flow around a square cylinder in a parallel channel. The validations of numerical schemes to steady and unsteady flow were completed.

2. Numerical Manifold Schemes for N-S Equations of Incompressible Viscous Flow

2.1. Galerkin Integration Expressions of N-S Equations

For numerical solution of incompressible viscous flow, the integration expressions for the continuity equation and N-S equations can be obtained by Galerkin weighted residual method, and the weak solution form can be stated as

$$\int_{\Omega} v_j \frac{\partial}{\partial x_j}(\delta p)\mathrm{d}\Omega = \int_{\Gamma_1} \overline{v}_n \delta p \mathrm{d}\Gamma, \tag{2.1a}$$

$$\int_{\Omega}\left[\rho\left(\frac{\partial v_i}{\partial t} + v_j\frac{\partial v_i}{\partial x_j}\right)\delta v_i + \left[-p\delta_{ij} + \mu\left(\frac{\partial v_i}{\partial x_j} + \frac{\partial v_j}{\partial x_i}\right)\right]\frac{\partial}{\partial x_j}(\delta v_i)\right]\mathrm{d}\Omega = \int_{\Gamma_2}\overline{p}_i\delta v_i\mathrm{d}\Gamma + \int_{\Omega}\rho f_i\delta v_i\mathrm{d}\Omega, \tag{2.1b}$$

where t denotes the time variable; ρ is the fluid density; μ is the dynamic viscosity; v_j is the velocity in x_j direction; p is the pressure; f_i is the body force per unit volume in x_i direction; δp is referred to the weight function for continuity equation and δv_i for momentum equation; Ω is the domain of solution; $\overline{v}_n$ is the known normal velocity on boundary Γ_1; $\overline{p}_i$ is the known pressure components in x_i direction on boundary Γ_2.

2.2. Numerical Manifold Schemes for N-S Equations

2.2.1. Element Velocity and Pressure Cover Functions

When NMM is applied into solution of N-S equations, suggested that there are M manifold elements in finite element cover system and each element (e) has n physical covers, and the cover weight functions are $N_j(x,y)$ $(j = 1,2,\ldots,n)$, which meet the requirement of partition of unity $\sum_{j=1}^{n} N_j(x,y) = 1$ $(x,y \in e)$, then the element global velocity and pressure cover functions $v_j(x,y)$ and $p(x,y)$ can be given by weighted summation of the cover functions of every physical cover as the follows:

$$\begin{aligned} v_i(x,y) &= N_j(x,y)v_{ij}(x,y), \\ p(x,y) &= N_j(x,y)p_j(x,y), \end{aligned} \tag{2.2}$$

where $i = 1,2$ for two-dimensional (2D) flow problem; $v_{ij}(x,y)$ are the velocity component cover functions for physical cover U_j of element (e) and $p_j(x,y)$ is the pressure cover function. If polynomial functions are taken as the cover functions of every physical cover, the cover functions can be stated in the form as

$$\begin{aligned} v_{ij}(x,y) &= f_k^v \cdot D_{ijk}^v, \\ p_j(x,y) &= f_l^p \cdot D_{jl}^p, \end{aligned} \tag{2.3}$$

where f_k^v, f_l^p denote the basic series for velocity and pressure cover functions of physical cover U_j; D_{ijk}^v,D_{jl}^p are the cover DOF variables, and the DOF numbers are m_v $(k = 1,2,\ldots,m_v)$ and m_p $(l = 1,2,\ldots,m_p)$.

By substituting (2.3) into (2.2), the global cover functions for velocity and pressure in element (e) can be written as

$$v_i(x,y) = N_j(x,y)v_{ij}(x,y) = N_j(x,y)f_k^v D_{ijk}^v = T_{jk}^v D_{ijk}^v, \tag{2.4a}$$

$$p(x,y) = N_j(x,y)p_j(x,y) = N_j(x,y)f_l^p D_{jl}^p = T_{jl}^p D_{jl}^p, \tag{2.4b}$$

where T_{jk}^v is the element velocity cover basic function; T_{jl}^p is the element pressure cover basic function. The element cover basic functions consist of the basic series of cover functions and cover weight functions, and the element DOF variables are composed of all the cover DOF variables.

In Galerkin integration equations (2.1a) and (2.1b), the weight functions for continuity equation and N-S equations can adopt the element basic functions of velocity components and pressure accordingly, that is,

$$\delta v_i = T^v_{jk}; \qquad \delta p = T^p_{jl}. \tag{2.5}$$

The partial derivatives of element cover functions can be obtained from (2.4a) and (2.4b) as the follows:

$$v_{i,\alpha} = T^v_{jk,\alpha} D^v_{ijk}; \qquad p_{,\alpha} = T^p_{jl,\alpha} D^p_{jl}; \qquad v_{i,t} = T^v_{jk} D^v_{ijk,t} = T^v_{jk} \dot{D}^v_{ijk}, \tag{2.6}$$

where $\alpha = 1, 2$ for 2D problem; $T^v_{jk,\alpha}$, $T^p_{jl,\alpha}$ are the partial derivatives of element velocity and pressure cover basic functions with respect to x_α, respectively; $\dot{D}^v_{ijk}$ are the partial derivatives of element velocity DOF variables with respect to t.

2.2.2. Element Manifold Schemes

For each element (e) in finite element cover system, element manifold equations can be derived by introducing (2.4a), (2.4b), (2.5), and (2.6) into (2.2), and the equations can be stated as

$$\int_{\Omega^e} T^v_{\beta I} D^v_{\alpha\beta I} T^p_{jl,\alpha} \mathrm{d}\Omega = \int_{\Gamma^e_1} \overline{v}_n T^p_{jl} \mathrm{d}\Gamma,$$

$$\int_{\Omega^e} \left[\rho T^v_{\beta I} \dot{D}^v_{i\beta I} T^v_{jk} + \rho T^v_{\beta I} D^v_{\alpha\beta I} T^v_{\gamma J,\alpha} D^v_{i\gamma J} T^v_{jk} - T^p_{\beta K} D^p_{\beta K} \delta_{i\alpha} T^v_{jk,\alpha} + \mu \left(T^v_{\gamma J,\alpha} D^v_{i\gamma J} + T^v_{\gamma J,i} D^v_{\alpha\gamma J} \right) T^v_{jk,\alpha} \right] \mathrm{d}\Omega$$
$$= \int_{\Gamma^e_2} \overline{p}_i T^v_{jk} \mathrm{d}\Gamma + \int_{\Omega^e} \rho f_i T^v_{jk} \mathrm{d}\Omega, \tag{2.7}$$

that is,

$$G^e_{jl\alpha\beta I} D^v_{\alpha\beta I} = H^e_{jl}, \tag{2.8a}$$

$$A^e_{jk\gamma J} \dot{D}^v_{i\gamma J} + B^e_{jk\alpha\beta\gamma IJ} D^v_{\alpha\beta I} D^v_{i\gamma J} + C^e_{ijk\beta K} D^p_{\beta K} + E^e_{jki\alpha\gamma J} D^v_{\alpha\gamma J} = F^e_{ijk}, \tag{2.8b}$$

where $\beta, \gamma = 1, 2, \ldots, n$; $I, J = 1, 2, \ldots, m_v$, $K = 1, 2, \ldots, m_p$; and the coefficients for element manifold equations are

$$A^e_{jk\gamma J} = \int_{\Omega^e} \rho T^v_{\gamma J} T^v_{jk} \mathrm{d}\Omega, \qquad B^e_{jk\alpha\beta\gamma IJ} = \int_{\Omega^e} \rho T^v_{\beta I} T^v_{\gamma J,\alpha} T^v_{jk} \mathrm{d}\Omega,$$
$$C^e_{ijk\beta K} = -\int_{\Omega^e} T^p_{\beta K} \delta_{i\alpha} T^v_{jk,\alpha} \mathrm{d}\Omega, \qquad E^e_{jki\alpha\gamma J} = \int_{\Omega^e} \mu T^v_{jk,s} \left(\delta_{i\alpha} T^v_{\gamma J,s} + \delta_{s\alpha} T^v_{\gamma J,i} \right) \mathrm{d}\Omega,$$
$$F^e_{ijk} = \int_{\Gamma^e_2} \overline{p}_i T^v_{jk} \mathrm{d}\Gamma + \int_{\Omega^e} \rho f_i T^v_{jk} \mathrm{d}\Omega, \qquad G^e_{jl\alpha\beta I} = \int_{\Omega^e} T^v_{\beta I} T^p_{jl,\alpha} \mathrm{d}\Omega, \qquad H^e_{jl} = \int_{\Gamma^e_1} \overline{v}_n T^p_{jl} \mathrm{d}\Gamma. \tag{2.9}$$

Equations (2.8a) and (2.8b) are the nonlinear algebra equations with respect to coupled velocity and pressure DOF variables and first-order linear ordinary differential equations with respect to time.

3. Some Key Techniques

3.1. Mixed Cover Functions for Velocity and Pressure

In FEM, when velocity and pressure field are discretized in the same way, the discrete element can not be ensured to satisfy the Ladyzanskya Babuska Brezzi stability condition (LBB condition), and these kinds of element cannot be applied to directly solve N-S equations coupled velocity and pressure for the spatial oscillation of pressure field. Mixed elements can be built to meet the LBB condition by increasing velocity interpolation node [18], but the elements are inconvenient to apply in practice for the complicated calculation process and difficult element discretization.

In finite element cover system of NMM, the element cover functions are composed of the weight functions and the cover functions of physical covers. Generally, the weight functions will adopt the element shape functions as in FEM, which are usually defined by the element shape and nodes. The cover functions of every physical cover for different physical variables can employ different order functions according to the solving physical equations. When NMM is applied to solve N-S equations for incompressible viscous flow, the velocity and pressure field can be discretized in the same way and the weight functions will employ the same interpolation functions for element velocity and pressure variables. But, the cover functions of every element physical cover can apply different order functions for velocity and pressure variables, so it will form a manifold element with mixed cover functions for velocity and pressure variables, which can meet the requirements of different order approximate functions for velocity and pressure in Galerkin integration expressions (2.1a) and (2.1b) and satisfy the LBB condition for increasing the DOF numbers of velocity variables. The mixed cover manifold elements can be applied in direct solution of incompressible viscous N-S-equations-coupled velocity and pressure variables.

In theory, velocity components and pressure covers can employ very high-order functions, but it will cause a very complicated calculation process, so low-order polynomial functions are favorable. If pressure cover function of every physical cover is defined as constant function, velocity cover functions can adopt linear polynomial functions, and then the basic series in (2.3) can be given by the following localized series for 2D problem:

$$\left[f_k^v\right] = \left[1 \quad \eta_1(x - x_c) \quad \eta_2(y - y_c)\right]; \qquad \left[f_l^p\right] = [1], \tag{3.1}$$

where (x, y) is the coordinate variables; (x_c, y_c) is the center coordinates of physical cover; η_1, η_2 are the coefficients of cover functions.

3.2. Solution of Manifold Equations for Steady N-S Equations

As to 2D steady N-S equations, element manifold equations (2.8a) and (2.8b) can be reformatted as

$$B^e_{jk\alpha\beta\gamma IJ} D^v_{\alpha\beta I} D^v_{1\gamma J} + C^e_{1jk\beta K} D^p_{\beta K} + E^e_{jk1\alpha\gamma J} D^v_{\alpha\gamma J} = F^e_{1jk},$$

$$B^e_{jk\alpha\beta\gamma IJ} D^v_{\alpha\beta I} D^v_{2\gamma J} + C^e_{2jk\beta K} D^p_{\beta K} + E^e_{jk2\alpha\gamma J} D^v_{\alpha\gamma J} = F^e_{2jk},$$
$$G^e_{jl\alpha\beta I} D^v_{\alpha\beta I} = H^e_{jl}, \tag{3.2}$$

where $j, k, l, \alpha, \beta, \gamma, I, J$ are similar to (2.8a) and (2.8b); $D_{1\gamma J}$, $D_{2\gamma J}$, and $D_{\beta K}$ are the unknown variables. The equations can be written in the matrix form as

$$\begin{bmatrix} B^e_{jk1\beta\gamma IJ} D^v_{1\beta I} + E^e_{jk11\gamma J} & B^e_{jk2\beta\gamma IJ} D^v_{1\beta I} + E^e_{jk12\gamma J} & C^e_{1jk\beta K} \\ B^e_{jk1\beta\gamma IJ} D^v_{2\beta I} + E^e_{jk21\gamma J} & B^e_{jk2\beta\gamma IJ} D^v_{2\beta I} + E^e_{jk22\gamma J} & C^e_{2jk\beta K} \\ G^e_{jl1\gamma J} & G^e_{jl2\gamma J} & 0 \end{bmatrix} \begin{Bmatrix} D^v_{1\gamma J} \\ D^v_{2\gamma J} \\ D^p_{\beta K} \end{Bmatrix} = \begin{Bmatrix} F^e_{1jk} \\ F^e_{2jk} \\ H^e_{jl} \end{Bmatrix}, \tag{3.3a}$$

that is,

$$[K^e]\{D^e\} = \{F^e\}, \tag{3.3b}$$

where $[K^e]$ is the element flow matrix with respect to unknown velocity DOF variables; $\{D^e\}$ is the element DOF variables; $\{F^e\}$ is the element generalized loads.

The manifold equations (3.3a) and (3.3b) are nonlinear algebra equations and can be solved by two methods of directly linearizing alternate iteration and Newton-Raphson iterative in general.

3.3. Solution of Manifold Equations for Steady N-S Equations

As to 2D unsteady N-S equations, the first-order linear ordinary differential equation (2.8b) with respect to time need be translated into linear algebra equations by time difference replacing the derivative. At any discrete time step t_i, the nonlinear manifold equations can be solved by implicit iterative methods or explicit methods. If implicit iterative methods are used, the derivative of velocity DOF variables for every physical cover with respect to time in (2.8b) will be discretized by time difference as

$$\dot{D}^v_{ijk} = \frac{\left(D^{v(i+1)}_{ijk} - D^{v(i)}_{ijk}\right)}{\Delta t}, \tag{3.4}$$

where Δt is time step; $D^{v(i)}_{ijk}$ and $D^{v(i+1)}_{ijk}$ are the velocity DOF variables at time step t_i and t_{i+1}, respectively. Then as to every manifold element (e), the element manifold equations (2.8b) can be reformulated as the follows:

$$\begin{aligned} &A^e_{jk\gamma J} D^{v(i+1)}_{i\gamma J} + \Delta t B^e_{jk\alpha\beta\gamma IJ} D^{v(i+1)}_{\alpha\beta I} D^{v(i+1)}_{i\gamma J} + \Delta t C^e_{ijk\beta K} D^{p(i+1)}_{\beta K} + \Delta t E^e_{jki\alpha\gamma J} D^{v(i+1)}_{\alpha\gamma J} \\ &\quad = \Delta t F^e_{ijk} + A^e_{jk\beta I} D^{v(i)}_{ijk}. \end{aligned} \tag{3.5}$$

Equations (3.5) uniting (2.8a) can be stated in matrix form as

$$\begin{bmatrix} A^e_{jk\gamma J} + \Delta t\left(B^e_{jk1\beta\gamma IJ}D^{v(i+1)}_{1\beta I} + E^e_{jk11\gamma J}\right) & \Delta t\left(B^e_{jk2\beta\gamma IJ}D^{v(i+1)}_{1\beta I} + E^e_{jk12\gamma J}\right) & \Delta tC^e_{1jk\beta K} \\ \Delta t\left(B^e_{jk1\beta\gamma IJ}D^{v(i+1)}_{2\beta I} + E^e_{jk21\gamma J}\right) & A^e_{jk\gamma J} + \Delta t\left(B^e_{jk2\beta\gamma IJ}D^{v(i+1)}_{2\beta I} + E^e_{jk22\gamma J}\right) & \Delta tC^e_{2jk\beta K} \\ G^e_{jl1\gamma J} & G^e_{jl2\gamma J} & 0 \end{bmatrix} \cdot \begin{Bmatrix} D^{v(i+1)}_{1\gamma J} \\ D^{v(i+1)}_{2\gamma J} \\ D^{p(i+1)}_{\beta K} \end{Bmatrix} = \begin{Bmatrix} \Delta tF^e_{1jk} + A^e_{jk\gamma J}D^{v(i)}_{1\gamma J} \\ \Delta tF^e_{2jk} + A^e_{jk\gamma J}D^{v(i)}_{2\gamma J} \\ H^e_{jl} \end{Bmatrix}, \tag{3.6}$$

that is,

$$[k^e]\left\{D^{e(i+1)}\right\} = \{F^e\}, \tag{3.7}$$

where $\{D^{p(i+1)}_{\beta K}\}$ is the pressure cover DOF variables at time step t_{i+1}; $\{D^{e(i+1)}\}$ is the element unknown cover DOF variables at time step t_{i+1}; $[k^e]$ is the element flow matrix with respect to the unknown velocity DOF variables at time step t_{i+1}; $\{F^e\}$ is the element generalized loads with respect to the boundary conditions and the known velocity DOF variables at time step t_i.

The manifold equations (3.7) for unsteady flow can be solved by iterative methods. In this paper, Newton-Raphson iterative method is also used here for solution of unsteady flow manifold equations.

4. Numerical Example of Flow around a Square Cylinder in a Channel

To illustrate the validity of the present numerical manifold method, low-Re incompressible viscous flow around a square cylinder in a channel and flow past a step are investigated in details through direct solution of N-S equations in dimensionless form in this paper as two numerical examples. In numerical manifold analysis, standard rectangular finite element cover system with 4-node manifold element as show in Figure 1 is used, the mixed cover functions of physical covers with the basic series equations (3.1) are adopted, and the shape functions of rectangular element are employed as the cover weight functions in (2.2), that is,

$$N_1(x,y) = \frac{1}{4}\left(1 - \frac{x-x_0}{a}\right)\left(1 - \frac{y-y_0}{b}\right), \qquad N_2(x,y) = \frac{1}{4}\left(1 + \frac{x-x_0}{a}\right)\left(1 - \frac{y-y_0}{b}\right),$$
$$N_3(x,y) = \frac{1}{4}\left(1 + \frac{x-x_0}{a}\right)\left(1 + \frac{y-y_0}{b}\right), \qquad N_4(x,y) = \frac{1}{4}\left(1 - \frac{x-x_0}{a}\right)\left(1 + \frac{y-y_0}{b}\right), \tag{4.1}$$

where (x_0, y_0) are the coordinates of element (e) center point; $2a \times 2b$ are the side lengths.

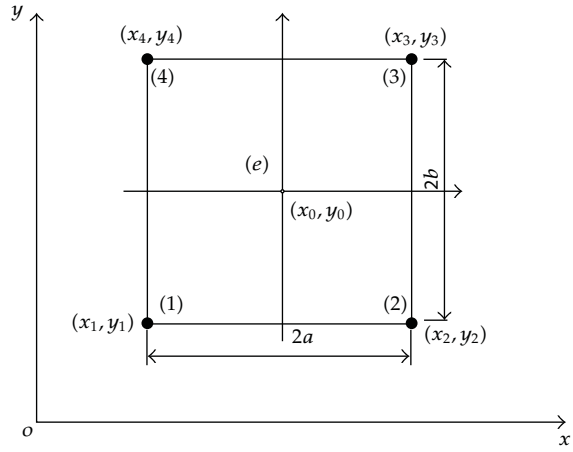

Figure 1: 4-node rectangular manifold element.

4.1. Analysis for Steady Flow past a Step

In numerical analysis of flow past a step, finite element cover system and boundary conditions are shown in Figure 2(a), the characteristic velocity of the flow field inlet is $u = 1$ and $v = 0$, the fluid density is $\rho = 1$, and three dynamic viscosities of fluid are μ =0.01, 0.005, 0.0025, and so Re numbers are known as Re =100, 200, 400, respectively. All the flow field is meshed into 196 elements and 229 nodes by 0.1 × 0.1 rectangular grids.

The streamline and pressure distribution in flow field past a step at Re = 200 are shown in Figure 2(b). The streamline patterns obtained from direct numerical solutions have revealed the vortex structure at the step of flow field, and high accurate pressure distributions have been obtained as well. The numerical solutions from FVM are shown in Figures 2(c) and 2(d) comparatively, which obtained from 0.1 × 0.1 and 0.05 × 0.05 rectangular grids, respectively. The NMM results from 0.1 × 0.1 grids are nearly coincident with the FVM results from 0.05 × 0.05 grids. The comparative analyses illustrate that numerical manifold schemes with mixed cover are stable numerical schemes for incompressible viscous flow, can implement direct numerical solution of N-S equations coupled velocity and pressure variables and can improve the solution accuracy at the same grids compared with FVM.

4.2. Analysis for Steady Flow around a Square Cylinder in a Channel

The flow field configuration and boundary conditions of flow around a square cylinder in a channel are shown in Figure 3. The length of the channel is $L = 4$, the width is $W = 1$. The size of square cylinder is $d \times d = 0.25 \times 0.25$, its horizontal axis coincides with the channel's centerline, and its vertical axis is perpendicular to the channel's centreline. The velocity condition of the inlet AD is $u/u_{\text{av}} = 1.5\ [1 - (1 - y/y_m)^2]$ ($u_{\text{av}} = 1$ is the average flow velocity in the channel, $y_m = 0.5$ is the channel centerline) and $v = 0$, the pressure condition of outlet BC is $p = 0$, and the nonslip boundary conditions are set on other fixed walls, that is, $u = v = 0$.

The flow field is meshed by three mixed grids, one is that 32 × 16 uniform element grid is used for the domain from $x = 0$ to $x = 2$ and 20 × 16 element grid for the domain from $x = 2$

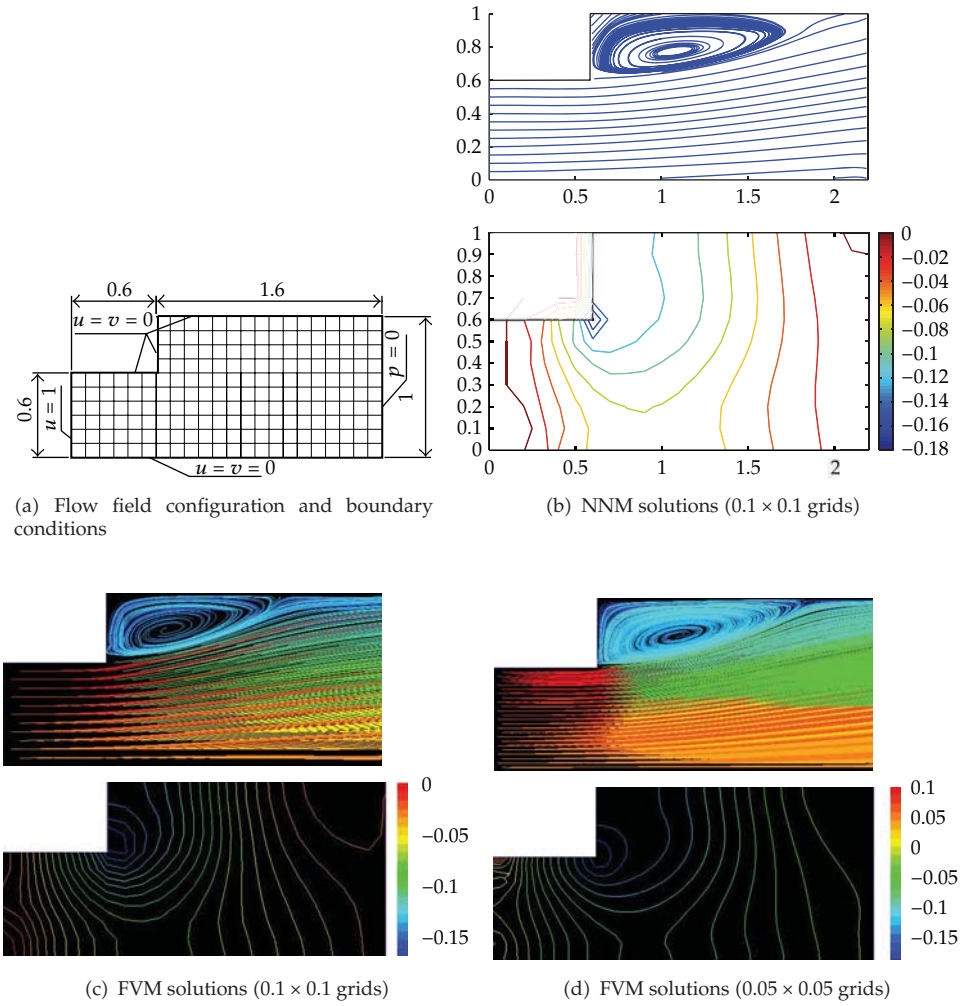

Figure 2: The streamline patterns and pressure distributions for flow field past a step.

to $x = 4$, the entire flow field is meshed by $52 \times 16 = 832$ elements and $53 \times 17 = 901$ nodes; the second one is that 64×32 uniform element grid is used for $x = 0 \sim 2$ and 40×32 element grid for $x = 2 \sim 4$, the flow field is meshed by $104 \times 32 = 3328$ elements and $105 \times 33 = 3465$ nodes; the third one is that 96×48 uniform element grid is used for $x = 0 \sim 2$ and 64×48 element grid for $x = 2 \sim 4$, the flow field is meshed by $160 \times 48 = 7680$ elements and $161 \times 49 = 7889$ nodes.

The numerical analyses of steady flow at different Re numbers (Re = 25, 50, 75, 100, 150) are performed by the NMM solutions of steady N-S equations. The streamline patterns and variables distributions of flow field at Re = 100 from three different element grids are compared. The results from the first element grid are different to these from two other grids, but the results from the second grid are closely similar to these from the third one, and the average difference of velocity and pressure on the channel centreline is less than 5%, so the second element grid is enough for flow at Re < 100, and the third element grid or finer element grid is more reasonable for flow at Re = 100 and 150.

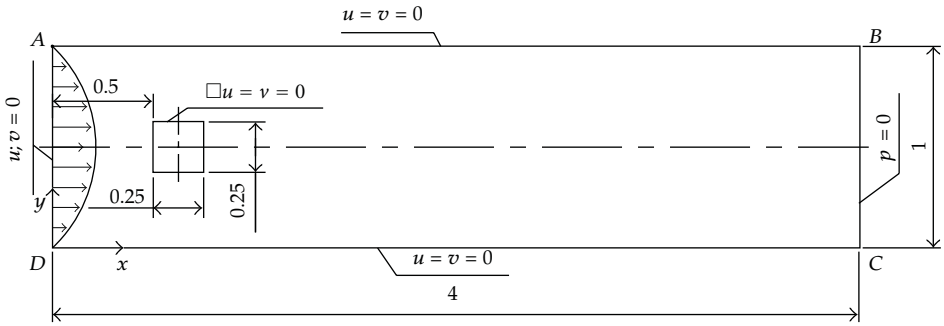

Figure 3: Flow field configuration and boundary conditions of flow around a square cylinder.

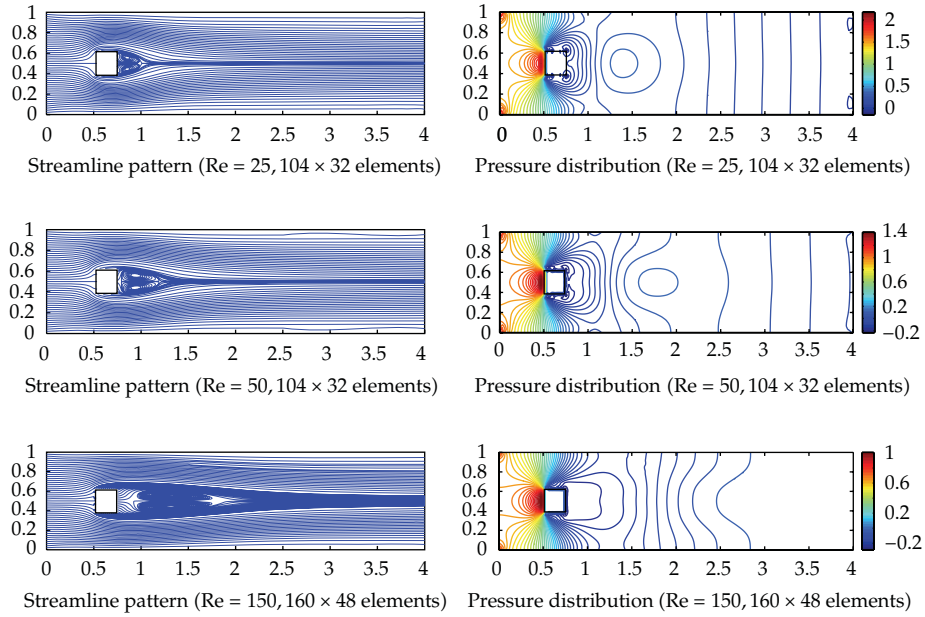

Figure 4: Streamline pattern and pressure distribution for flow field at different Re numbers.

The streamline patterns and pressure distributions at different Re numbers are shown in Figure 4. At Re = 25 and 50, there are two stable symmetrical vortexes behind the square cylinder, and the flow patterns are similar to the numerical solutions of Mukhopadhyay et al. [15]. As Re number increases to Re ≈ [50, 200], Cherry's results show that two vortexes become unsymmetrical and Karman vortex street is formed behind the square cylinder gradually [14], but the stable convergent results are obtained from NMM solutions of steady N-S equations at Re = 75, 100, and 150, and there are also two stable symmetrical vortexes behind the square cylinder. The distances from back flow point of the vortexes to square cylinder at Re = 25, 50, 75, 100, 150 are 1.0, 1.2, 1.4, 1.6, 1.8, respectively, which are approximately linear with Re numbers. These results illustrate that numerical manifold schemes for steady N-S equations have the strong-stability-preserving property.

In NMM analysis unlike FVM and FEM analysis, the pressure distributions of flow field are obtained from direct numerical solutions of N-S equations and continuity equation,

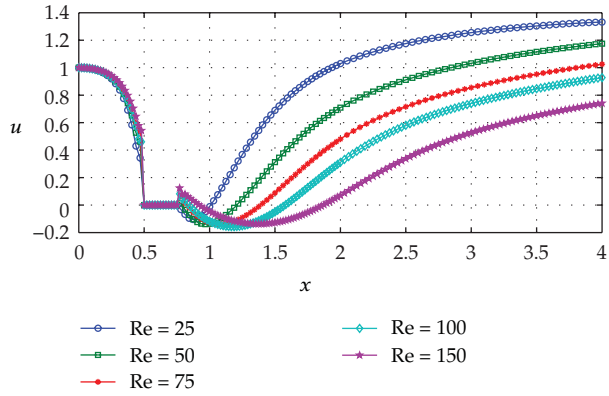

Figure 5: Comparison of velocity u along horizontal lines through geometric center of flow field.

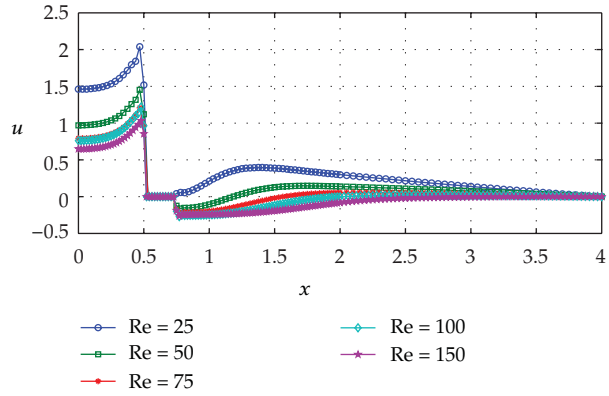

Figure 6: Comparison of pressure along horizontal lines through geometric center of flow field.

so it can improve the solution accuracy of pressure field. The pressure distributions of flow field show that high-pressure area is formed in frontage of the square cylinder for flow blockage, low pressure areas are formed near behind two front corner points for flow separating, and large pressure gradient is produced near the corner points. The pressure distributions are symmetrical, and the pressure of flow field will decrease as Re number increasing.

The velocity u distributions along horizontal lines through geometric center of flow field are shown in Figure 5. The velocity u drops rapidly from inlet to the square cylinder for flow blockage. Negative velocity appears behind the cylinder for back flow, and the velocity will rise gradually with away from the cylinder, and the velocity restoring becomes slow as Re number increases. The pressure distributions along horizontal lines through geometric center of flow field are shown in Figure 6. The pressure rises gradually from inlet to the square cylinder. Positive pressure appears behind the cylinder at low Re number, negative pressure appears at comparatively high Re number, and the pressure will drops or rises to zero at outlet of flow field.

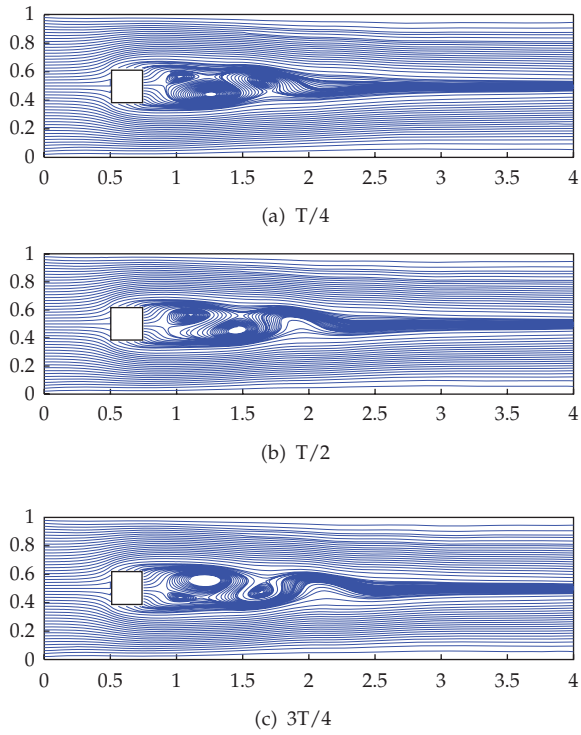

Figure 7: The streamline patterns for flow field from 48×160 element grid and $\Delta t = 0.01$ s time step at Re = 150.

4.3. Analysis for Unsteady Flow around a Square Cylinder in a Channel

The flow field configuration and boundary conditions of unsteady flow around a square cylinder in a channel are the same as these of steady flow, and the flow field is meshed by the third mixed grids. The unsteady flows at different Re numbers (Re = 50, 75, 100, 150) are also analyzed through NMM solutions of N-S equations in this paper, where numerical solutions for steady flow at Re = 50 are adopted as the initial conditions, the total computational time is 10 s, and the time step is 0.01 s.

When $\mathrm{Re} \leq 50$, numerical solutions from unsteady flow analyses are closely similar to the results from steady flow analyses, and there are two steady symmetrical vortexes behind the square cylinder. As Re number increasing, two vortexes become unsymmetrical, and Karman Vortex Street is formed behind the square cylinder gradually. The streamline patterns for flow field at Re = 150 are shown in Figure 7, and the periodical change process of appearing, developing, moving, separating of the vortexes are clearly displayed in the streamline patterns. The Strouhal number is 0.2438, the difference is 2.2% and 6.5% to [15, 16]. The flow patterns are similar to Mukhopadhyay's and Yutaka's results, which is obtained from very fine element grid [15, 17].

The pressure contours for flow field at Re = 150 are show in Figure 8. The pressure distributions beside and in frontage of the square cylinder are almost identical to the results from steady flow analyses and are different behind the cylinder, which will change with the moving of vortexes.

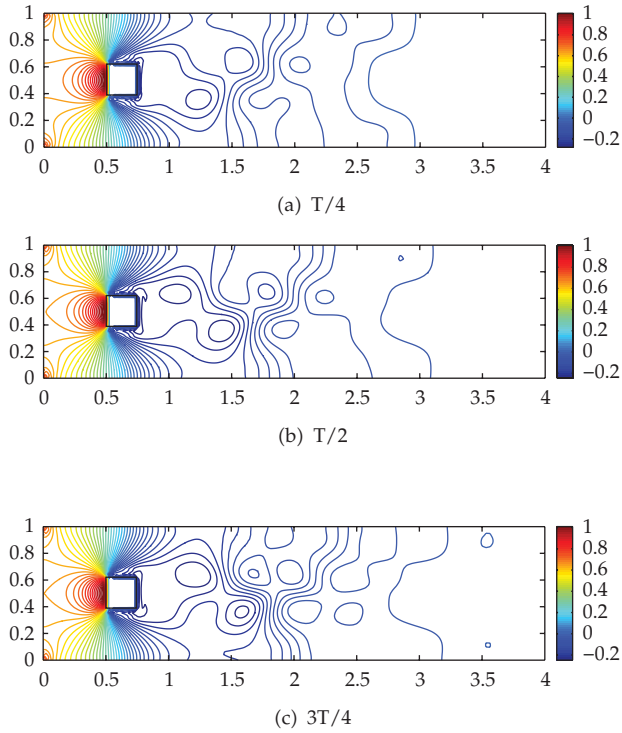

Figure 8: The pressure contours for flow field from 48 × 160 element grid and $\Delta t = 0.01$ s time step at Re = 150.

5. Summary

Numerical manifold method for direct coupled solution of incompressible viscous flow N-S equations has been developed in this paper. Numerical manifold schemes integrated velocity and pressure were derived based on Galerkin-weighted residuals method as well. Mixed cover with linear polynomial function for velocity and constant function for pressure was adopted in finite element cover system. Compared with FVM and FEM, in NMM for incompressible viscous flow, the accuracy of velocity variables approximation can be improved by adopting high-order cover function, direct numerical solution of N-S equations, and continuity equation coupled velocity and pressure variables can be implemented by adopting finite cover system with mixed cover manifold element, so it can improve the solution accuracy of velocity and pressure variables.

As an application, mixed cover 4-node rectangular manifold element has been used to simulate flow around a square cylinder in a channel and past a step at low Re numbers. As to flow around a square cylinder in a channel, accurate numerical results have been presented for steady flow at Re = 25, 50, 75, 100, 150 and for unsteady flow at Re = 100, 150. The rules on streamline patterns and pressure distributions were analyzed in details. Numerical solutions were in very good agreement with the published data from very fine element meshes. Numerical tests indicate that manifold method is an effective and high-order accurate numerical method for incompressible viscous flow Navier-Stokes equations.

Acknowledgment

Financial support for this project was provided by the National Natural Science Foundation of China (no. 50975050).

References

[1] J. H. Ferziger and M. Perić, *Computational Methods for Fluid Dynamics*, Springer, New York, NY, USA, 3rd edition, 1996.

[2] J. Nordström, J. Gong, E. van der Weide, and M. Svärd, "A stable and conservative high order multi-block method for the compressible Navier-Stokes equations," *Journal of Computational Physics*, vol. 228, no. 24, pp. 9020–9035, 2009.

[3] L. Zhang and Z. Chen, "A stabilized mixed finite element method for single-phase compressible flow," *Journal of Applied Mathematics*, vol. 2011, Article ID 129724, 16 pages, 2011.

[4] S. Boivin, F. Cayré, and J. M. Hérard, "A finite volume method to solve the Navier-Stokes equations for incompressible flows on unstructured meshes," *International Journal of Thermal Sciences*, vol. 39, no. 8, pp. 806–825, 2000.

[5] P. Pořízková, K. Kozel, and J. Horáček, "Numerical simulation of unsteady compressible flow in convergent channel: pressure spectral analysis," *Journal of Applied Mathematics*, vol. 2012, Article ID 545120, 9 pages, 2012.

[6] G. H. Shi, "Manifold method," in *Proceedings of the 1st International Forum on Discontinuous Deformation Analysis & Simulation of Discontinuous Media*, pp. 52–204, Berkeley, Calif, USA, 1996.

[7] G. H. Shi, "Manifold method of material analysis," in *Proceedings of the 9th Army Conference on Applied Mathematics and Computing*, pp. 51–76, Minneapolis, Minn, USA, 1992.

[8] K. Terada and M. Kurumatani, "Performance assessment of generalized elements in the finite cover method," *Finite Elements in Analysis and Design*, vol. 41, no. 2, pp. 111–132, 2004.

[9] K. Terada and M. Kurumatani, "An integrated procedure for three-dimensional structural analysis with the finite cover method," *International Journal for Numerical Methods in Engineering*, vol. 63, no. 15, pp. 2102–2123, 2005.

[10] K. Terada, T. Ishii, T. Kyoya, and Y. Kishino, "Finite cover method for progressive failure with cohesive zone fracture in heterogeneous solids and structures," *Computational Mechanics*, vol. 39, no. 2, pp. 191–210, 2007.

[11] H. Y. Liu, S. R. Lv, and S. Q. Qin, "Simulation of rock shock damage evolution law with numerical manifold method," *Engineering Science*, vol. 19, no. 1, pp. 392–396, 2007 (Chinese).

[12] G. F. Wei and W. Feng, "Incompatible numerical manifold method based on heat exchange problem," *Chinese Quarterly of Mechanics*, vol. 26, no. 3, pp. 451–454, 2005 (Chinese).

[13] Z. R. Zhang, X. W. Zhang, and J. H. Yan, "Manifold method coupled velocity and pressure for Navier-Stokes equations and direct numerical solution of unsteady incompressible viscous flow," *Computers & Fluids*, vol. 39, no. 8, pp. 1353–1365, 2010.

[14] N. J. Cherry, R. Hillier, and M. E. M. P. Latour, "Unsteady measurements in a separated and reattaching flow," *Journal of Fluid Mechanics*, vol. 144, pp. 13–46, 1984.

[15] A. Mukhopadhyay, G. Biswas, and T. Sundararajan, "Numerical investigation of confined wakes behind a square cylinder in a channel," *International Journal for Numerical Methods in Fluids*, vol. 14, no. 12, pp. 1473–1484, 1992.

[16] Z. Dang, G. Xi, and S. J. Wang, "Application of the piso method in simulation of unsteady wakes behind a square cylinder," *Journal of Engineering Thermophysics*, vol. 20, no. 3, pp. 317–321, 1999 (Chinese).

[17] Y. Yoshida and T. Nomura, "A transient solution method for the finite element incompressible Navier-Stokes equations," *International Journal for Numerical Methods in Fluids*, vol. 5, no. 10, pp. 873–890, 1985.

[18] O. C. Zienkiewicz, S. Qu, R. L. Taylor, and S. Nakazawa, "The patch test for mixed formulations," *International Journal for Numerical Methods in Engineering*, vol. 23, no. 10, pp. 1873–1883, 1986.

Hindawi Publishing Corporation
Journal of Applied Mathematics
Volume 2012, Article ID 502979, 16 pages
doi:10.1155/2012/502979

Research Article

Exergy Analysis in Hydrogen-Air Detonation

Abel Rouboa,[1,2] Valter Silva,[1] and Nuno Couto[1]

[1] *CITAB/Engineering Department, School of Science and Technology of University of UTAD, Vila Real 5001-801, Portugal*
[2] *MEAM Department, University of Pennsylvania, Philadelphia, PA 19104, USA*

Correspondence should be addressed to Valter Silva, vbrsilva@utad.pt

Received 16 December 2011; Accepted 10 April 2012

Academic Editor: Fu-Yun Zhao

The main goal of this paper is to analyze the exergy losses during the shock and rarefaction wave of hydrogen-air mixture. First, detonation parameters (pressure, temperature, density, and species mass fraction) are calculated for three cases where the hydrogen mass fraction in air is 1.5%, 2.5%, and 5%. Then, exergy efficiency is used as objective criteria of performance evaluation. A two-dimensional computational fluid dynamic code is developed using Finite volume discretization method coupled with implicit scheme for the time discretization (Euler system equations). A seven-species and five-step global reactions mechanism is used. Implicit total variation diminishing (TVD) algorithm, based on Riemann solver, is solved. The typical diagrams of exergy balances of hydrogen detonation in air are calculated for each case. The energy balance shows a successive conversion of kinetic energy, and total enthalpy, however, does not indicate consequent losses. On the other hand, exergy losses increase with the augment of hydrogen concentration in air. It obtained an exergetic efficiency of 77.2%, 73.4% and 69.7% for the hydrogen concentrations of 1.5%, 2.5%, and 5%, respectively.

1. Introduction

The Ramjet propulsion principle was invented at the beginning of the 20th century by Rene Lorin [1, 2], who published it in the technical review "Aérophile" in 1913. A Ramjet is an air-breathing jet engine which uses the engine's forward motion to compress incoming air, without a rotary compressor. The development of this propulsion method was slow and was practically started only from the 1950s. Some years later appeared the pulsed detonation engine (PDE), which is a type of propulsion system that uses detonation waves to combust the fuel and oxidizer mixture [3, 4].

The excitement about pulse detonation engines (PDEs) stems from the fact that, theoretically at least, they can operate at thermal efficiencies about 30% higher than

conventional combustion processes. This is due to the high detonation velocities between $1500\,\mathrm{m\cdot s^{-1}}$ and $2200\,\mathrm{m\cdot s^{-1}}$ in a hydrocarbon fuel/air mixture; for example, its thermodynamic cycle is effectively a constant volume or Humphrey cycle [5–7]. The Humphrey cycle can be considered a modification of the Brayton cycle in which the constant-pressure heat addition process of the Brayton cycle is replaced by a constant-volume heat addition process [8].

Due to this thermodynamic efficiency and mechanical simplicity, the PDE technology is more efficient when compared with current engine types. Additionally, the PDE can also provide static thrust for a ramjet or scramjet engine or operate in combination with turbofan systems showing an enormous potential to be applied in many sectors of the aerospace, aeronautic, and military industries. However, there are still engineering challenges that must be overcome, such as to improve methods for initiating the detonation process and develop materials able to withstand with extreme conditions of heat and pressure.

In the PDE technology the combustion takes place in an open-ended tube in which fuel is mixed with air and detonated. As the detonation wave travels down the tube at supersonic speed, a refraction wave propagates into the combustor, and exhaust products leave the chamber. Pressure within the chamber jumps down to charging conditions, which draws in fresh fuel and air, and the cycle is repeated. Each pulse lasts only milliseconds [9, 10]. Detonation is initiated by a predetonator, containing a more readily detonable mixture of fuel air, or by DDT (deflagration detonation transition), a process by which a flame, initiated at the closed end of a duct by a weak spark, accelerates to speeds on the order of $1000\,\mathrm{m\cdot s^{-1}}$ at which point a detonation wave is initiated within the flame-shock complex [11–13].

The existence of flames for problems with complex chemistry in the combustion approximation has been considered by many authors; see, for example, [14–18]. It has been pointed out in [19], that reaction mechanisms including chain branching can lead to significant qualitative differences in the initiation of detonations in comparison to single step reactions. The use of the exergy concept can be used with advantage to best understand the detonation problem [20]. The exergy gives a quantitative and illustrative description of the convertibility of different energy forms and is a function of the system and environment, whereas entropy is a function only of the system. Total exergy, thermomechanical and chemical, has been defined as the work which can be obtained by taking the system, by means of reversible processes, from its initial state to a state of total equilibrium (dead state), thermal, mechanical, and chemical ("unrestricted equilibrium"), with the environment. This definition entails that the system is in a state of internal equilibrium (uniformity of all intensive properties) and that the environment is in a state which is in internal equilibrium and does not change during time. The exergy of a fluid stream depends upon the choice of the reference environment. This choice, which seems obvious according to some authors [20–22], is, on the contrary, problematic, since every usual environment is a chemical state of nonequilibrium.

A simplified model of adiabatic detonation process in gases was considered by Petela [20] using the concept of exergy. The exergy loss for high pressure shock is larger than that for reactions of combustion. On the other hand, the total exergy loss for deflagration is also larger than that for detonation. Huntchins and Metghalchi [21] analyzing the thermal efficiency show that the Humphrey cycle reveals good advantage compared with Brayton cycle using the same fuel. They also compare the effectiveness of both cycles and conclude that the results using the Humphrey cycle have significant advantage comparing with a Brayton cycle based on the same fuel (methane). Also, the research work of Wintenberger and Shepherd [22] finds that this efficiency cannot be precisely translated into propulsive efficiency. Indeed, the results are only useful in comparing detonations with other combustion modes. They also find that

the efficiency of cycles based on detonation and constant-volume combustion is very similar and superior to a constant-pressure combustion (Brayton) cycle when compared on the basis of pressure at the start of the combustion process.

This paper reports an exergy analysis on the detonation wave between the pulse shock wave to the end of the rarefaction wave for various concentrations of the hydrogen in air. Numerical simulation of a two-dimensional detonation of the hydrogen-air mixture is considered. The coupled hydrodynamical model and chemical model integrating the Euler system equations are combined with a detailed chemical reaction model.

2. Numerical Method

Supersonic combustion, called detonation, occurs coupled to a shock wave traveling at supersonic speed. If premixed gases inside a tube closed at both ends are ignited at one end, a laminar flame first develops, traveling pushed by the expanding hot products behind. The inverted small pressure jump across the flame generates local pressure pulses that wrinkle the flame, create turbulence, extend the burning area, and increase the burning rate, with a positive feedback that, if positively combined with pressure pulses reflected from the other end, might compress the fresh mixture to the autoignition temperature.

2.1. Chemical Model

Consider the reaction of hydrogen with oxygen to yield water that is usually written as

$$H_2 + \frac{1}{2}O_2 \longrightarrow H_2O. \tag{2.1}$$

The detonation of hydrogen in air must start by dissociation of a hydrogen molecule (it requires less energy than oxygen dissociation):

$$H_2 + M \longrightarrow H + H + M, \tag{2.2}$$

where M stands for an unspecified molecule (hydrogen, oxygen, a hot wire). The following basic reactions take place:

$$\begin{aligned} H_2 + M &\longrightarrow H + H + M, \\ H + O_2 &\longrightarrow OH + O, \\ O + H_2 &\longrightarrow OH + H, \\ OH + H_2 &\longrightarrow H_2O + H, \\ H + OH + M &\longrightarrow H_2O + M. \end{aligned} \tag{2.3}$$

The chemical kinetic scheme involves seven species, H_2, O_2, H_2O, OH, O, H, and N_2 and the above-described 5 elementary reversible reactions. The mechanism is the one proposed by Balakrishnan and Williams [23], and the empirical parameters from each one

Table 1: Empirical values for reactions in the combustion of hydrogen with air [24].

Reaction	A ($cm^3 \cdot gmol \cdot s^{-1}$)	b	E_A ($MJ \cdot mol^{-1}$)	Temperature range
$H + H + M \rightarrow H_2 + M$	$6.4 \cdot 0^{17}$	−1.00	0.0	300–2500 K
$H + O_2 \rightarrow OH + O$	$1.2 \cdot 10^{17}$	−0.91	69.1	300–2500 K
$O + H_2 \rightarrow OH + H$	$1.5 \cdot 10^{7}$	2.00	31.6	300–2500 K
$H + OH + H_2O \rightarrow 2H_2O$	$1.4 \cdot 10^{23}$	−2.00	0.0	1000–3000 K
$H_2O + M \rightarrow H + OH + M$	$1.6 \cdot 10^{17}$	0.00	478.0	2000–5000 K

of the reactions [24] are depicted in Table 1. $k(T,p)$ is the "rate coefficient," which generally depends on temperature (T), and activation energy and can be defined as follows:

$$k(T) = AT^b e^{-(E_a/RT)}, \tag{2.4}$$

where A is the preexponential factor as in Arrhenius law and E_a is the activation energy. The three parameters A, b, and E_a are determined in practice experimentally.

The chemical production rates are computed using the methodology suggested by Warnatz [25]. In general, for the reaction $A + B \rightarrow$ products not just to species A, it can be defined:

$$\frac{dc_A}{dt} = \frac{dc_B}{dt} = -c_A c_B A T^b \exp\left(\frac{-E_A}{RT}\right). \tag{2.5}$$

2.2. Euler System Equations

The contributions of pressure-driven diffusion, bulk viscosity, and radiative heat transport can be neglected; then the balance equations of mass, momentum, and energy for the two-dimensional unsteady flow for a multicomponent chemically reacting gas mixture are written in the integral form as

$$\begin{aligned} \frac{\partial}{\partial t}\iiint_{\Omega} \rho dV + \oiint_{\partial\Omega} \rho\left(\vec{V}\cdot\vec{n}\right) dS &= 0, \\ \frac{\partial}{\partial t}\iiint_{\Omega} \rho\vec{V} dV + \oiint_{\partial\Omega} \left(\rho\vec{V}\left(\vec{V}\cdot\vec{n}\right) + p\vec{n}\right) dS &= \vec{0}, \\ \frac{\partial}{\partial t}\iiint_{\Omega} \rho E dV + \oiint_{\partial\Omega} (\rho E + p)\left(\vec{V}\cdot\vec{n}\right) dS &= 0. \end{aligned} \tag{2.6}$$

The state equation can be defined as follows:

$$p = (\gamma - 1)\cdot\left[\rho E - \frac{1}{2}\rho\vec{V}^2\right]. \tag{2.7}$$

In these system equations the density $\rho(M,t)$ is the total density of the whole gas in the position M, and at time t. $\rho(M,t)$ is calculated as sum of mass fraction (Y_i) and density (ρi) of each species:

$$\rho = \sum_{i=1}^{k} Y_i \rho_i. \tag{2.8}$$

The above equation system is rewritten in a control volume as follows:

$$\frac{\partial \vec{U}}{\partial t} + \frac{\partial F\left(\vec{U}\right)}{\partial x} + \frac{\partial G\left(\vec{U}\right)}{\partial y} = \vec{W}, \tag{2.9}$$

where

$$\vec{U} \equiv \begin{pmatrix} \rho \\ \rho u \\ \rho v \\ \rho E \\ \rho Y_1 \\ \rho Y_2 \\ \vdots \\ \rho Y_{k-1} \end{pmatrix}; \quad \overrightarrow{F(U)} \equiv \begin{pmatrix} \rho u \\ \rho u^2 + P \\ \rho uv \\ u(\rho E + P) \\ \rho Y_1 u \\ \rho Y_2 u \\ \vdots \\ \rho Y_{k-1} u \end{pmatrix}; \quad \overrightarrow{G(U)} \equiv \begin{pmatrix} \rho v \\ \rho uv \\ \rho v^2 + P \\ v(\rho E + P) \\ \rho Y_1 v \\ \rho Y_2 v \\ \vdots \\ \rho Y_{k-1} v \end{pmatrix}; \quad \overrightarrow{W} \equiv \begin{pmatrix} 0 \\ 0 \\ 0 \\ 0 \\ \dot{w}_1 \\ \dot{w}_2 \\ \vdots \\ \dot{w}_{k-1} \end{pmatrix}. \tag{2.10}$$

In these equations u and v are the velocity vector components in the directions x and y, T the mixture temperature, ρ the mixture density, p the pressure, e and E are the internal and total energies, respectively. For each of the k chemical species, Y_k is the mass fraction, M_k is the molecular, and h_i is the specific enthalpy. Then, the following equations of state can be also defined:

$$\begin{aligned} Y_k &= 1 - \sum_{i=1}^{k-1} Y_i, \\ P &= \rho RT \sum_{i=1}^{k} \frac{Y_i}{M_k}, \\ h_i &= h^0 + \int_{T_0}^{T} c_{p_i} dT = e_i + \frac{P}{\rho}, \\ E &= e + \frac{1}{2}\left(u^2 + v^2\right) = \sum_{i=1}^{k} Y_i e_i + \frac{1}{2}\left(u^2 + v^2\right). \end{aligned} \tag{2.11}$$

2.3. The Solution Procedure

The numerical methods that have been developed in this code for hydrogen and combustion are detailed in [26, 27]. These include lumped parameters, CFD-type codes, and also the

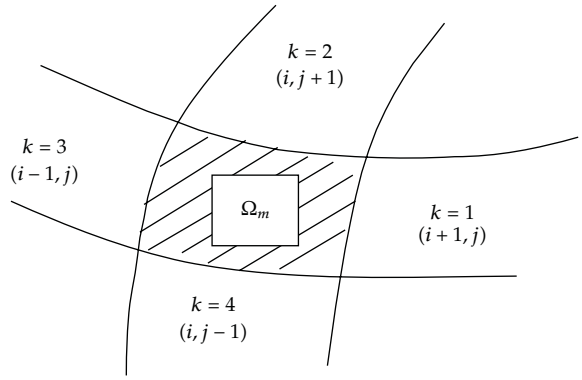

Figure 1: Structured mesh.

CAST3M code [28] developed at the French Atomic Centre Energy (CEA). CAST3M is a general finite-element/finite-volume code for structural and fluid mechanics and heat transfer.

The CAST3M code is used to model both hydrogen dispersion and combustion phenomena over a very wide range of flow regimes, from nearly incompressible flow to compressible flow with shock waves. This could be done by developing a most suitable (i.e., accurate and efficient) numerical method for each type of flow or developing a single method suitable for all flow regimes. We are not aware of any single numerical method able to treat accurately and efficiently flow regimes which range from slowly evolving nearly incompressible buoyant flow to fast transient supersonic flow. However, in practice, for detonation simulation, the use of shock-capturing methods is preferred. In the hydrogen risk analysis tools CEA is developing; the choice was made to develop in the same computational platform CAST3M code for distribution calculations, an efficient pressure-based solver using a semi-implicit incremental projection algorithm which allows the use of "large" time steps, for combustion calculations, a robust and accurate density-based solver using a shock-capturing conservative method.

A brief description of the method we used here, typical for such hyperbolic system equations, follows. Consider the system of hyperbolic conservation laws, (2.10), with the initial conditions:

$$u(x,y,0) = u_0(x,y). \tag{2.12}$$

Given a uniform grid with time step Δt and spatial mesh size $(\Delta x, \Delta y)$, we define an approximation of U at the point $xi = i\Delta x$, $yj = j\Delta y$, $tn = n\Delta t$ by the finite volume formula:

$$U_{i,j}^{n+1} = U_{i,j}^{n+1} - \frac{\Delta t}{\Delta x}\left[F_{i+1/2,j}^{n} - F_{i-1/2,j}^{n}\right] - \frac{\Delta t}{\Delta y}\left[G_{i,j+1/2}^{n} - G_{i,j-1/2}^{n}\right] + W^{n}. \tag{2.13}$$

Figure 1 shows the structured mesh used in this problem. Finding the exact solution to the Riemann problem for the equation system (2.9) is complex. Even if we would find it, it would be too complex to use it at each cell boundary, as it needed in (2.13). Therefore, we have to look for some approximate Riemann solver. Here, we adopt the approach described

in [29], which we have already considered in case of conservation laws. Let us rewrite the homogeneous hyperbolic system (2.9) in primitive variables for one direction:

$$\frac{\partial U}{\partial t} + \frac{\partial F(U)}{\partial x} = \frac{\partial U}{\partial t} + A(U)\frac{\partial U}{\partial x} = 0. \tag{2.14}$$

Consider the Riemann problem for (2.14) at each cell boundary $j + 1/2$, that is, with the following initial data:

$$U(x,0) = \begin{cases} U_j, & x \le x_{j+1/2} \\ U_{j+1}, & x \ge x_{j+1/2}. \end{cases} \tag{2.15}$$

Following [10, 11], we calculate the Jacobian matrix $A(U)$ in the average state:

$$v_{j+1/2} = \frac{v_j + v_{j+1}}{2}. \tag{2.16}$$

The intermediate state in the solution of the Riemann problem is

$$v^*_{j+1/2} = v_j + \sum_{\lambda_i<0} a_i r_i, \tag{2.17}$$

where the eigenvalues λ_i and the eigenvectors r_i of the Jacobian matrix $A(v_j + 1/2)$ and a_i are the coefficients of eigenvector decomposition of $(v_j + 1 - v_j)$:

$$v_{j+1/2} - v_j = \sum_{i=0}^{6} a_i r_i. \tag{2.18}$$

With the choice of the primitive variables, they are given by the following expressions:

$$\begin{pmatrix} a_0 \\ a_1 \\ a_2 \\ a_3 \\ a_4 \\ a_5 \\ a_6 \end{pmatrix} = \begin{pmatrix} \dfrac{\Delta_1}{r_{01}} \\ \dfrac{\left[-\Delta_3\rho_a c_a + \Delta_4 + a_0\left(r_{03}\rho_a c_a - r_{04}\right)\right]}{2\rho_a c_a^2} \\ \Delta_2 - a_0 r_{02} - \rho_a(a_1 + a_2) \\ \dfrac{\left[\Delta_3\rho_a c_a + \Delta_4 - a_0\left(r_{03}\rho_a c_a + r_{04}\right)\right]}{2\rho_a c_a^2} \\ \dfrac{\left[-\Delta_6\rho_b c_b + \Delta_7 + a_0\left(r_{06}\rho_b c_b - r_{07}\right)\right]}{2\rho_b c_b^2} \\ \Delta_5 - a_0 r_{05} - \rho_b(a_4 + a_6) \\ \dfrac{\left[\Delta_6\rho_b c_b + \Delta_7 - a_0\left(r_{06}\rho_b c_b + r_{07}\right)\right]}{2\rho_b c_b^2} \end{pmatrix}, \tag{2.19}$$

where r_{0k} are the components of r_0 and Δk is the k th component of $(v_j + 1 - v_j)$. Recalculating $v_j + 1/2$ into the conservative vector $uj + 1/2$, we fully determine the Godunov-type scheme (2.17) for the homogeneous system (2.14).

3. Exergy Calculation

A practical definition of exergy (E) for a closed system is the maximal work that can be obtained when a thermodynamic system is allowed to attain equilibrium with an environment defined as the "dead state," typically defined as the system ambient. If that ambient is at temperature T_0 and pressure, p_0, the exergy is

$$E = (U - U_0) + p_0(V - V_0) - T_0(S - S_0), \tag{3.1}$$

where U, V, and S denote, respectively, the internal energy, volume, and entropy of the system, and U_0, V_0 and S_0 are the values of the same properties in the system which were called dead state.

The exergy expression can be generalized considering Q as a heat transfer across a system boundary where the temperature is constant at T_b and taking in account the mass flow across the boundary of a control. The exergy rate balance for a control can be derived using these described approaches, where the control volume forms of mass and energy rate balances are obtained by transforming the closed system forms. The exergy accompanying mass flow and heat transfer can be written as

$$\frac{dE}{dt} = \sum_j \left(1 - \frac{T_0}{T}\right) \cdot Q_j + \sum_{\text{exit}} \dot{m}_e \varepsilon_e - \sum_{\text{inlet}} \dot{m}_i \varepsilon_i, \tag{3.2}$$

where ε_e e and ε_i are the exit and inlet specific exergy and Q_j is the heat transport rate. The sum of the thermomechanical and chemical exergies is the total exergy associated with a given system at a specified state, relative to a specified exergy reference environment. The chemical exergy is defined as

$$\varepsilon^{ch} = \left(\sum_i n_r \cdot \overline{h}_r - \sum_i n_p \cdot \overline{h}_p\right)_{(T_0,P_0)} - T_0\left(\sum_i n_r \cdot \overline{S}_r - \sum_i n_p \cdot \overline{S}_p\right)_{(T_0,P_1)} \tag{3.3}$$

or in the following form, when the entropy at (T_0, P_1) is calculated:

$$\varepsilon^{ch} = \left(\sum_i n_r \cdot \overline{h}_r - \sum_i n_p \cdot \overline{h}_p\right)_{(T_0,P_0)} - T_0\left(\sum_i n_r \cdot \overline{S}_r - \sum_i n_p \cdot \overline{S}_p\right)_{(T_0,P_0)} + RT_0 \ln\left(\frac{\prod_i^{n_r} \Upsilon_i}{\prod_i^{n_p} \Upsilon_i}\right), \tag{3.4}$$

where Υ_r, Υ_p, are the mass fraction of reactants and products of involved reactions and h_r, S_r, h_p, and S_p are the specific enthalpy and specific entropy for the reactants and products, respectively. The specific enthalpy terms are determined using the enthalpy of formation for respective substances. The specific entropy appearing in the above equation is absolute entropy. Even if the logarithmic term normally contributes a few percent, it will not be

Table 2: Standard chemical exergies [30].

Species	Standard chemical exergy (kJ·mol^{-1})
O_2	3.900
N_2	0.640
H_2O	8.635
H_2	235.250

neglected in the present paper. The Gibbs function for each one of the components could be expressed as follows:

$$\varepsilon^{ch} = \left(\sum_i n_r \cdot \overline{g}_r - \sum_i n_p \cdot \overline{g}_p \right) + RT_0 \ln \left(\frac{\prod_i^{n_r} Y_i}{\prod_i^{n_p} Y_i} \right). \tag{3.5}$$

The energy associated with a specific state of a system is the sum of two contributions: the thermomechanical contribution and the chemical contribution. On unit mass, the total exergy is:

$$\varepsilon = \underbrace{(U - U_0) + p_0(V - V_0) - T_0(S - S_0)}_{(1)} + \underbrace{\varepsilon^{ch}}_{(2)}, \tag{3.6}$$

where (2.1) is the thermo mechanical contribution and (2.2) is the chemical contribution.

The molar exergy of each reactant and product, at temperature T_1, is given by

$$\varepsilon_1 = \varepsilon_O + (\Delta h_{O \to 1} - T_O \Delta s_{O \to 1}). \tag{3.7}$$

The standard chemical exergies of the reactants and products are given in Table 2.

The specific chemical exergy of a material stream is that part of the exergy that results from the sum of the chemical potential differences between the pure reference substances and the pure material stream components at T_0 and P_0. The specific mixing exergy of a material stream is that part of the exergy resulting from the sum of two contributions.

(i) The differences in potential between the exergies of the environmental components in environmental concentrations and pure environmental components at T_0 and P_0.

(ii) The difference in potential of the exergy due to mixing of the pure components into a mixed material stream at T_0 and P_0.

The different exergy components are listed in Table 3.

Finally, it can be defined as a "performance factor" the ratio of outlet exergy to inlet exergy:

$$\phi_{\text{eff}} = \frac{\varepsilon_{\text{out}}}{\varepsilon_{\text{inl}}}. \tag{3.8}$$

Table 3: Subdivision of the exergy.

Environment	
Change in concentrations of the environment components at T_o and P_o	(Mixture exergy)
Exergy of the pure environment components at T_o and P_o	
Chemical reaction of the pure environment components at T_o and P_o	(Chemical exergy)
Exergy of the pure components at T_o and P_o	
Mixing of the pure components at T_o and P_o	(Mixture exergy)
Change in temperature and pressure at constant composition	
Exergy of the mixed components at T_o and P_o	(Thermo mechanical exergy)
Exergy of the mixed components at T_o and P_o	

4. Results and Discussion

The structure of the pulse detonation and the shock tube is depicted in Figures 2 and 3, respectively.

The detonation field parameters in this work were computed by using the Euler multispecies equations of detonation of H_2-air mixture. They were solved using the first author's solution procedure [26, 27]. Analyses were carried out for different hydrogen concentrations in air optimum pressure with corresponding temperatures; species concentrations were determined and given first case in figures as function of time. As an example, for first case where the mass fraction of H_2 is equal to 1.5%, peak detonation and end rarefaction density of the selected location were taken at 1.4 kg·m^{-3} and 1.1 kg·m^{-3}, respectively. As a result, optimum shock and rarefaction temperatures were found to be 1930 K and 700 K, respectively. At the same time, the optimum pressures were found to be 18 bar and 6 bar, respectively for the same concentration of hydrogen in air.

As seen in Figure 4 representing the pressure distribution along the tube at 0.003 ms, the optimum pressure at the peak of detonation was found to be 18 bar, 22 bar, and 36 bar for 1.5%, 2.5%, and 5% of hydrogen mass fractions, respectively. Figure 5 shows the result of the temperature at 0.003 ms corresponding to the end of reactions for the case of hydrogen concentration equal to 1.5%. Optimum values vary from 1930 K for the peak of detonation to 700 K for the end of rarefaction. These results show that the structure of the detonation wave is dependent on hydrogen concentration.

Figure 6 shows the shock pressure variation with time for the three different concentrations of hydrogen in air.

The first case considers a hydrogen-air mixture at an initial pressure $P_0 = 1$ bar and initial temperature $T_0 = 298$ K. On the left side of the tube (Figure 3) a pressure pulse (10 bars) is considered to initialize the shock wave. At $t = 0$ s, the shock wave moves from the left to the right side of the tube and initiates the reactions. Shock waves generated due to the formation of a new reaction front are called "reaction shocks" [20]. The reaction shock overtakes the shock front at around 27 μs, strengthening it and sharply increasing its propagation speed; that is, a detonation wave is formed. Subsequently, the detonation wave speed decreases gradually and a high-frequency, low-amplitude propagation mode is established. In this study no reaction delay is considered, so when the shock wave is initialized, the reactions produced energy. Generally, chemical reactions behind the shock front start generating weak shock waves after approximately 20 μs [31]. The plots show the variation in shock front speed with time. Initially the shock wave travels at a constant speed (determined by the

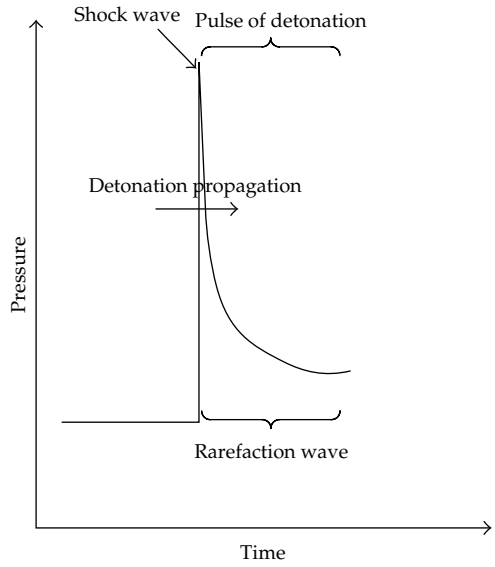

Figure 2: Structure of the pulse detonation.

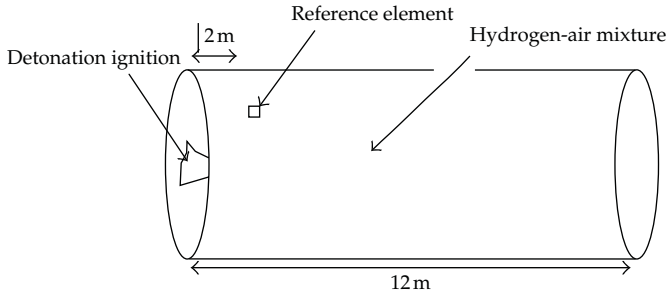

Figure 3: Shock tube.

initial conditions) slightly greater than 1500 $m \cdot s^{-1}$, 1800 $m \cdot s^{-1}$, and 2200 $m \cdot s^{-1}$ for respective hydrogen concentrations of 1.5%, 2.5%, and 5%.

Figures 6 and 7 show the variation with time of pressure and density as function of time and for mass fraction of hydrogen in air: 1.5%, 2.5%, and 5%. As can be seen from these figures, the peak of detonation is characterized by the high-pressure values followed by the rarefaction wave. During the rarefaction wave, the pressure, temperature, and density decrease; this decrease is stopped by the reflected wave from the end of the tube. The most detonation energy is absorbed by the shock when the wave is reflected. This is because by assuming that the detonation is instantaneous and all hydrogen is consumed in the first way of the shock wave, then the energy is completely kinetic, and, as a result, the density and pressure decrease.

Figure 8 shows the mass fraction of H_2O, calculated as function of time for the three studied cases: 1.5%, 2.5%, and 5% of hydrogen concentration. This figure gives us a good idea about mass fraction of H_2O during the detonation for each of hydrogen concentration in air. In fact, the contribution of H_2O in exergy calculation is not negligible since the

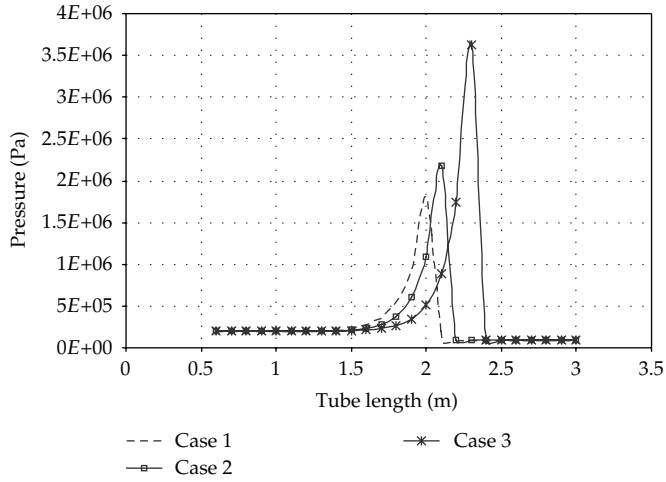

Figure 4: Pressure evolution along shock tube and as function of hydrogen mass fraction in air (case 1: 1.5%, case 2: 2.5%, case 3: 5%).

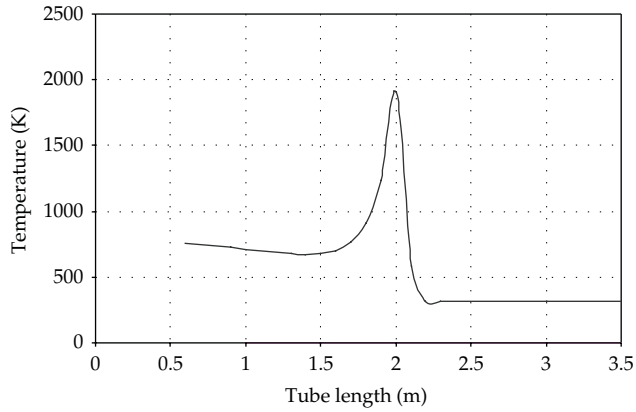

Figure 5: Temperature distribution along the tube length for case 1.

standard chemical exergy of H_2O, O_2, and N_2 are, respectively, 8.63 kJ·mol^{-1}, 3.90 kJ·mol^{-1}, and 0.60 kJ·mol^{-1}.

Mass fraction for the H_2, OH, and H_2O system is plotted in Figure 9. Here, the energy levels were chosen to be consistent with those realized in the detonation calculation. As seen in this figure the hydrogen, radical OH, and product H_2O as function of time for the referent element shown on Figure 3, optimum values at the end of reactions, were found to be 0.04%, 0.7%, and 1.2% carried out for species H_2, OH, and H_2O. These results are presented for the case when the initial mass fraction of hydrogen in air is assumed to be equal to 2.5%.

It is possible to consider the shock and rarefaction processes as the separate successive steps. Therefore, the exergy loss due to the irreversible detonation and the end of rarefaction can be calculated as the product of the initial temperature and the difference between entropies in the start of the shock wave and the end of rarefaction wave. The typical diagrams of exergy balances of hydrogen detonation in air are shown in Figure 10 as function of hydrogen concentration (1.5%, 2.5%, and 5%). Data were calculated for the point of

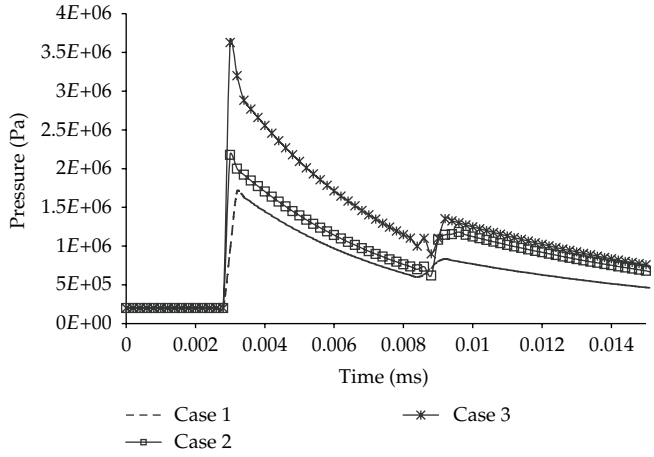

Figure 6: Pressure evolution as function of time with hydrogen mass fraction cases.

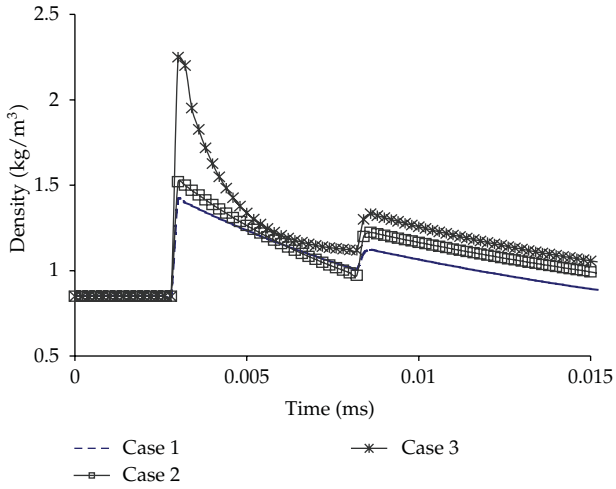

Figure 7: Density evolution for each hydrogen mass fraction in air.

steady detonation. It was shown that exergy losses increase with the augment of hydrogen concentration in air; consequently low hydrogen concentrations in air achieve slight higher efficiencies. It was also verified that the exergy efficiency decreases for all the hydrogen concentrations as a function of the time. It was obtained an exergetic efficiency of 77.2%, 73.4%, and 69.7% for the hydrogen concentrations of 1.5%, 2.5% and 5%, respectively.

On the other hand, the energy balance shows a successive conversion of kinetic energy and total enthalpy, however, does not indicate consequent losses.

5. Conclusions

The CFD code was developed using finite volume discretization method coupled with implicit scheme for the time discretization. The code solves the Euler system equations

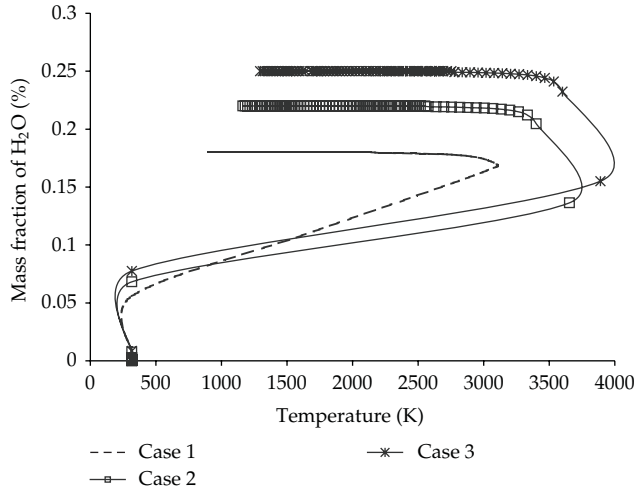

Figure 8: Mass fraction as function of temperature for each hydrogen concentration in air.

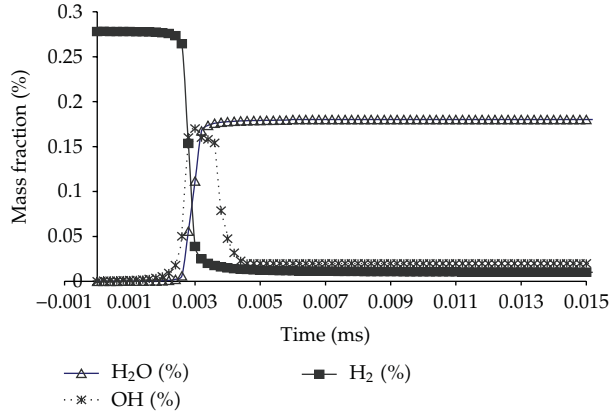

Figure 9: Mass fraction profile of the H_2, OH^- and products H_2O.

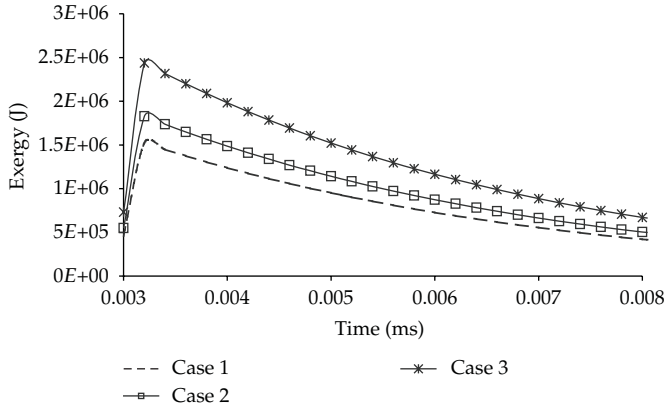

Figure 10: Exergy evolution as function of time with hydrogen mass fraction in air.

including a chemistry model, with 5 reactions and 7 species, using an implicit total variation diminishing (TVD) algorithm based on Riemann solver.

There exists a large literature about the numerical discretization of the detonation of hydrogen-air mixture problems: Eulerian schemes, Lagrangian schemes, front tracking techniques, and level set methods, among others. Our main goal, in the present work, is to use detonation parameters, from the beginning to the end of detonation of hydrogen-air mixture to calculate and analyze the exergy loss and the efficiency. The main steps of H_2-air mixture detonation calculation were explained. The developed program is able to calculate the pressure, temperature, density, and mass fraction, for each species from the chemical model. The exergy efficiency was used as objective criteria of performance evaluation.

We conclude in this work that the exergy losses increase with the augment of hydrogen concentration in air, and the efficiency of hydrogen detonation, with low concentration in air, is slightly elevated than the detonation using high hydrogen concentration.

Acknowledgments

The authors would like to express our gratitude to the Portuguese Foundation for Science and Technology (FCT) for the given support to the grant SFRH/BPD/71686 and to the project PTDC/AAC-AMB/103119/2008 and also to The French Atomic Centre Energy (CEA) for all the provided help.

References

[1] R. S. Fry, "A century of ramjet propulsion technology evolution," *Journal of Propulsion and Power*, vol. 20, no. 1, pp. 27–58, 2004.

[2] A. Davenas, "History of the development of solid rocket propellant in France," AIAA Paper 93-1785, 1993.

[3] K. Kailasanath, "Review of propulsion applications of detonation waves," *AIAA Journal*, vol. 39, no. 9, pp. 1698–1708, 2000.

[4] G. D. Roy, S. M. Frolov, A. A. Borisov, and D. W. Netzer, "Pulse detonation propulsion: challenges, current status, and future perspective," *Progress in Energy and Combustion Science*, vol. 30, no. 6, pp. 545–672, 2004.

[5] T. Bussing and G. Papas, "An introduction to pulse detonation engines," AIAA Paper 1994-263, 1994.

[6] S. Eidelman, W. Grossmann, and I. Lottati, "A review of propulsion applications of the pulsed detonation engine concept," AIAA Paper 89-2446, 1989.

[7] S. Eidelman, W. Grossmann, and I. Lottati, "Air-breathing pulsed detonation engine concept—a numerical study," AIAA Paper 90-2420, 1990.

[8] W. H. Heiser and D. T. Pratt, "Thermodynamic cycle analysis of pulse detonation engines," *Journal of Propulsion and Power*, vol. 18, no. 1, pp. 68–76, 2002.

[9] S. Eidelman, I. Lottati, and W. Grossmann, "A parametric study of airbreathing Pulsed Detonation Engine," AIAA Paper 90-2420, 1990.

[10] A. Wortman, P. Othmer, and W. Rostafinski, "Detonation duct gas generator demonstration program," AIAA Paper 92-3174, 1992.

[11] S. P. Medvedev, S. V. Khomik, H. Olivier, A. N. Polenov, A. M. Bartenev, and B. E. Gelfand, "Hydrogen detonation and fast deflagration triggered by a turbulent jet of combustion products," *Shock Waves*, vol. 14, no. 3, pp. 193–203, 2005.

[12] S. P. Medvedev, B. E. Gel'fand, A. N. Polenov, and S. V. Khomik, "Flammability limits for hydrogen-air mixtures in the presence of ultrafine droplets of water (Fog)," *Combustion, Explosion and Shock Waves*, vol. 38, no. 4, pp. 381–386, 2002.

[13] E. S. Oran, J. W. Weber, E. I. Stefaniw, M. H. Lefebvre, and J. D. Anderson, "A numerical study of a two-dimensional H_2–O_2–Ar detonation using a detailed chemical reaction model," *Combustion and Flame*, vol. 113, no. 1-2, pp. 147–163, 1998.

[14] H. Berestycki, B. Nicolaenko, and B. Scheurer, "Traveling wave solutions to combustion models and their singular limits," *SIAM Journal on Mathematical Analysis*, vol. 16, no. 6, pp. 1207–1242, 1985.
[15] A. Bonnet, "Travelling waves for planar flames with complex chemistry reaction network," *Communications on Pure and Applied Mathematics*, vol. 45, no. 10, pp. 1271–1302, 1992.
[16] P. C. Fife, S. P. Hastings, and C. Lu, "An asymptotic and rigorous study of flames with reversible chain branching," *Asymptotic Analysis*, vol. 5, no. 1, pp. 1–26, 1991.
[17] S. P. Hastings, C. Lu, and Y. H. Wan, "Existence of a traveling flame front in a model with no cold boundary difficulty," *SIAM Journal on Applied Mathematics*, vol. 47, no. 6, pp. 1229–1240, 1987.
[18] G. Joulin, A. Liñán, G. S. S. Ludford, N. Peters, and C. Schmidt-Lainé, "Flames with chain-branching/chain-breaking kinetics," *SIAM Journal on Applied Mathematics*, vol. 45, no. 3, pp. 420–434, 1985.
[19] J. W. Dold and A. K. Kapila, "Comparison between shock initiations of detonation using thermally-sensitive and chain-branching chemical models," *Combustion and Flame*, vol. 85, no. 1-2, pp. 185–194, 1991.
[20] R. Petela, "Application of exergy analysis to the hydrodynamic theory of detonation in gases," *Fuel Processing Technology*, vol. 67, no. 2, pp. 131–145, 2000.
[21] T. E. Hutchins and M. Metghalchi, "Energy and exergy analyses of the pulse detonation engine," *Journal of Engineering for Gas Turbines and Power*, vol. 125, no. 4, pp. 1075–1080, 2003.
[22] E. Wintenberger and J. E. Shepherd, "Thermodynamic analysis of combustion process for propulsion systems," AIAA Paper 2004-1033, 2004.
[23] G. Balakrishnan and F. A. Williams, "Turbulent combustion regimes for hypersonic propulsion employing hydrogen-air diffusion flames," *Journal of Propulsion and Power*, vol. 10, no. 3, pp. 434–436, 1994.
[24] D. L. Baulch, C. J. Cobos, R. A. Cox et al., "Evaluated kinetic data for combustion modeling," *Journal of Physical Chemistry*, vol. 21, no. 3, 324 pages, 1992.
[25] J. Warnatz, *Combustion Chemistry*, Edited by W.C. Gardiner Jr., Springer, New York, NY, USA, 1984.
[26] A. Rouboa, *Simulation of the detonation of Hydrogen-air Mixture in confined structure*, Ph.D. thesis, University of Paris VI, CEA, (Centre de l'Energy Atomique a Saclay), 1994.
[27] A. Rouboa, G. Poissant, A. Forestier, and R. J. Gibert, *Detonation Wave in 2-D Geometry*, vol. 337 of *Fluid-Structure Interaction*, American Society of Mechanical Engineers, Pressure Vessels and Piping Division (Publication) PVP, 1996.
[28] Castem, "Finite Elements and Finite Volume Code Developed inCEA," Atomic Energy Center, Saclay, France, 2000, http://www-cast3m.cea.fr/.
[29] B. Van Leer, W. Lee, and P. L. Roe, "Characteristic time-stepping or local preconditioning of Euler equations," AIAA Paper 97-1828, 1997.
[30] M. J. Moran, H. N. Shapiro, D. D. Boettner, and M. B. Bailey, *Fundamentals of Engineering Thermodynamics*, John Wiley & Sons, New York, NY, USA, 7th edition, 2010.
[31] D. Bradley, C. G. W. Sheppard, I. M. Suardjaja, and R. Woolley, "Fundamentals of high-energy spark ignition with lasers," *Combustion and Flame*, vol. 138, no. 1-2, pp. 55–77, 2004.

Hindawi Publishing Corporation
Journal of Applied Mathematics
Volume 2012, Article ID 738082, 21 pages
doi:10.1155/2012/738082

Research Article

Analysis of Mechanical Energy Transport on Free-Falling Wedge during Water-Entry Phase

Wen-Hua Wang,[1,2] Yi Huang,[2,3] and Yan-Ying Wang[3]

[1] *State Key Laboratory of Structural Analysis for Industrial Equipment, Dalian University of Technology, Dalian 116024, China*
[2] *Deepwater Engineering Research Center, Dalian University of Technology, Dalian 116024, China*
[3] *School of Naval Architecture, Dalian University of Technology, Dalian 116024, China*

Correspondence should be addressed to Wen-Hua Wang, wangwenhua0411@yahoo.cn

Received 19 January 2012; Accepted 25 March 2012

Academic Editor: Di Liu

For better discussing and understanding the physical phenomena and body-fluid interaction of water-entry problem, here mechanical-energy transport (wedge, fluid, and each other) of water-entry model for free falling wedge is studied by numerical method based on free surface capturing method and Cartesian cut cell mesh. In this method, incompressible Euler equations for a variable density fluid are numerically calculated by the finite volume method. Then artificial compressibility method, dual-time stepping technique, and Roe's approximate Riemann solver are applied in the numerical scheme. Furthermore, the projection method of momentum equations and exact Riemann solution are used to calculate the fluid pressure on solid boundary. On this basis, during water-entry phase of the free-falling wedge, macroscopic energy conversion of overall body-fluid system and microscopic energy transformation in fluid field are analyzed and discussed. Finally, based on test cases, many useful conclusions about mechanical energy transport for water entry problem are made and presented.

1. Introduction

Water-entry phenomena are very common and important in many practical projects, so it is clear that researches on various water-entry models are always the focus in the field of ship and ocean engineering. For better discussing and understanding the physical phenomena and body-fluid interaction during water-entry phase, this paper mainly discusses and studies the mechanical energy transport from two aspects, which are macroscopic energy conversion of overall wedge-fluid system and microscopic energy transformation in fluid field, respectively.

However, it is a hard task for water-entry problem to deal with moving free surface and solid boundary simultaneously. Furthermore, the body-fluid interaction during water

impact should increase the difficulty and complexity of accuracy calculation as discussed by Bunnik and Buchner [3]. Thus here an effective and available numerical method based on free surface capturing method and Cartesian cut cell mesh as studied by W. H. Wang and Y. Y. Wang [4] can be used to well handle the difficulty of moving free surface and solid boundary.

In this numerical method, by using free surface capturing method as discussed in [4–7], the incompressible Euler equations for a variable density fluid are taken as governing equations, and free surface should be captured as a contact discontinuity in the density field. On the other hand, Owing to its advantage of conveniently updating a few cells locally near solid boundary rather than remeshing the whole flow domain, Cartesian cut cell mesh system as shown [8–10] is applied to treat the moving body. Then, finite volume method is used to numerically discretize governing equations. In the numerical method, Roe's approximate Riemann solver as discussed by Roe [11] is introduced for flux evaluation at each edge of fluid cell, and the exact Riemann discontinuous solution as studied by W. H. Wang and Y. Y. Wang [4] is taken to achieve the flux on the solid boundary. Besides, dual-time stepping technique with artificial compressibility method as discussed by Soh and Goodrich [12] is applied in time advancing. Furthermore, the body-fluid interaction is calculated by means of a fully body-fluid coupled method as described by Kelecy and Pletcher [13].

On this basis, the theory of energy transport as demonstrated by Bird et al. [14] is introduced in the water-entry model to analyze and discuss the regularity about macroscopic energy conversion of overall wedge-fluid system and microscopic energy transformation in fluid field during water-entry phase. Finally, by taking water-entry model of free-falling wedge as test cases, many useful conclusions about mechanical energy transport for water-entry problem are made and presented.

2. Numerical Computational Method for Water-Entry Model

2.1. Governing Equations and Boundary Condition

Here, free surface capturing method is applied to treat water surface. For the 2D incompressible, unsteady, inviscid fluid system with a variable density field, the fixed x- and y-coordinate axes are along and vertical to free surface, respectively, so the governing equations can be written in the conservation form as follows.

The mass conservation equation:

$$\frac{\partial \rho}{\partial t} + \frac{\partial (\rho u)}{\partial x} + \frac{\partial (\rho v)}{\partial y} = 0, \tag{2.1}$$

the x-direction momentum equation:

$$\frac{\partial (\rho u)}{\partial t} + \frac{\partial (\rho u u + p)}{\partial x} + \frac{\partial (\rho u v)}{\partial y} = \rho B_x, \tag{2.2}$$

the y-direction momentum equation:

$$\frac{\partial(\rho v)}{\partial t} + \frac{\partial(\rho v u)}{\partial x} + \frac{\partial(\rho v v + p)}{\partial y} = \rho B_y, \tag{2.3}$$

and the incompressibility constraint equation:

$$\frac{\partial u}{\partial x} + \frac{\partial v}{\partial y} = 0, \tag{2.4}$$

where ρ is the fluid density, u, v represent the x- and y-directional fluid velocities, p is the fluid pressure, and B_x and B_y are the x and y-directional accelerations of body force, respectively.

In the current method, two kinds of boundary conditions should be used and described as

(1) outlet or open boundary: a zero gradient condition is applied to the velocity and density, and the pressure at this boundary is fixed to be static pressure, which allows fluid to enter or leave the computational domain freely according to the local flow velocity and direction;

(2) solid body boundary: the density is assumed to have a zero normal gradient, and the no-penetration condition can be applied to the velocity. For the case that a free rigid body moves with one degree (up or down) by referring to W. H. Wang and Y. Y. Wang [4], the projection method for momentum (2.2)-(2.3) is used to define the pressure boundary condition $\nabla p = [0, -\rho \partial v_S / \partial t - \rho g]$, here v_S^n is the vertical velocity of free-falling wedge with positive direction upwards.

2.2. Cartesian Cut Cell Mesh System

In the present study, Cartesian cut cell mesh is applied in spatial discretization of computational domain, which can be generated by cutting solid bodies out of a background Cartesian mesh. As a result, three kinds of cells (solid, fluid, and cut cell) are formed, in which geometric and fluid information can be stored. Moreover, the further detail about the mesh generation can be referred to the studies of Yang et al. [8, 9] and Causon et al. [10].

2.3. Numerical Discretization Scheme

Based on the Cartesian cut cell mesh, here a cell-central finite volume method is applied in numerical discretization. Therein, Roe's approximate Riemann solver is adopted to calculate the numerical flux on each edge of fluid cell, where fluid variables are reconstructed by using a piecewise linear upwind scheme, and then a least-square method as discussed by W. H. Wang and Y. Y. Wang [4] and Superbee limiter as shown by Qian et al. [5] are used to achieve variable gradients and control spurious oscillations, respectively. Besides, the flux on solid boundary can be achieved by means of exact Riemann discontinuous solution by referring to W. H. Wang and Y. Y. Wang [4]. Then dual-time stepping technique with artificial compressibility method is taken for time advancing. Finally, here an approximate

LU factorization (ALU) scheme as mentioned by Pan and Lomax [15] is applied to solve linear equations. The more details about the above numerical scheme can be further found from the study of W. H. Wang and Y. Y. Wang [4].

2.4. Interactive Fluid-Body Motion

Here for the water-entry model of free-falling wedge, a fully body-fluid coupled velocity method as discussed elsewhere [4, 13] is used to calculate the fluid-body motion.

Firstly, the new body velocity can be obtained by

$$\left(v_S^{n+1}\right)^{k+1} = \omega\left(v_S^n + \frac{\Delta t F_{\text{body}}^k}{m}\right) + (1-\omega)\left(v_S^{n+1}\right)^k, \tag{2.5}$$

where Δt is the physical time interval, m is the mass of wedge, v_S^n is the vertical body velocity at the physical time n, and ω is a relaxation parameter to control the stability of subiteration. The larger the ω is, the faster the convergence rate of subiteration is.

As shown in (2.5), a subiterative process should be carried out at each physical moment, and the convergence standard is $(v_S^{n+1})^{k+1} - (v_S^{n+1})^k < 10^{-3}$. Then the final convergent $(v_S^{n+1})^{k+1}$ can be taken as the new velocity boundary condition v_S^{n+1} for the next physical time step $n+1$.

Subsequently, by using the calculated v_S^{n+1}, the new vertical displacement of solid body can be achieved by

$$y_S^{n+1} = \frac{\Delta t\left(v_S^n + v_S^{n+1}\right)}{2}, \tag{2.6}$$

where y_S^{n+1} is the new displacement condition of solid body for the next physical time step $n+1$.

3. Theory of Mechanical Energy Transport in Fluid Field

3.1. The Equation of Mechanical Energy

In order to be convenient for describing the equation of mechanical energy, here (2.2) and (2.3) should be rewritten in vector form firstly:

$$\frac{\partial(\rho\mathbf{v})}{\partial t} = -\left[\nabla\cdot\rho\mathbf{v}\mathbf{v}\right] - \nabla p + \rho\mathbf{B}, \tag{3.1}$$

where $\mathbf{v} = u\mathbf{i} + v\mathbf{j}$ is the fluid velocity, $\mathbf{B} = B_x\mathbf{i} + B_y\mathbf{j}$ is the fluid acceleration of body force, and $\nabla p = \partial p/\partial x\mathbf{i} + \partial p/\partial y\mathbf{j}$ is the gradient of fluid pressure.

Then by taking the dot product of fluid velocity vector $\mathbf{v}$ with (3.1), the final result is the equation of change for kinetic energy as discussed by Bird et al. [14]:

$$\frac{\partial}{\partial t}\left(\frac{1}{2}\rho v^2\right) = -\left(\nabla \cdot \left(\frac{1}{2}\rho v^2\right)\mathbf{v}\right) - (\nabla p \cdot \mathbf{v}) + \rho(\mathbf{v} \cdot \mathbf{B}). \tag{3.2}$$

In this equation, $\partial(\rho v^2/2)/\partial t$ is increase rate of kinetic energy per unit volume, $-(\nabla p \cdot \mathbf{v})$ is rate of work done by pressure of surroundings on the fluid, $-(\nabla \cdot (\rho v^2/2)\mathbf{v})$ is the rate of kinetic energy addition by convective transport, and $\rho(\mathbf{v} \cdot \mathbf{B})$ is rate of work done by body-fluid force.

With the introduction of the potential energy, (3.2) assumes the following form, and the equations of change for mechanical and potential energy can be written as

$$\frac{\partial}{\partial t}\left(\frac{1}{2}\rho v^2 + \rho g y\right) = -\left(\nabla \cdot \left(\frac{1}{2}\rho v^2 + \rho g y\right)\mathbf{v}\right) - (\nabla p \cdot \mathbf{v}), \tag{3.3}$$

$$\frac{\partial}{\partial t}(\rho g y) = -(\nabla \cdot (\rho g y)\mathbf{v}) - \rho(\mathbf{v} \cdot \mathbf{B}), \tag{3.4}$$

where $\partial(\rho g y)/\partial t$ is the increase rate of potential energy per unit volume, and $-(\nabla \cdot (\rho g y)\mathbf{v})$ is the rate of potential energy addition per unit volume by convective transport.

3.2. The Macroscopic Balance of Mechanical Energy in Fluid Field

The most important use of microscopic kinetic plus potential energy (3.3) is for the development of the macroscopic mechanical energy balance, which can be integrated in whole fluid field:

$$\int_{V(t)} \frac{\partial}{\partial t}\left(\frac{1}{2}\rho v^2 + \rho g y\right) dV = -\int_{V(t)} \left[\nabla \cdot \left(\frac{1}{2}\rho v^2 + \rho g y\right)\mathbf{v}\right] dV - \int_{V(t)} (\nabla p \cdot v) dV. \tag{3.5}$$

Next based on the Leibniz equation and Gauss law as shown by Bird et al. [14], (3.5) can be rewritten as

$$\frac{d}{dt}\int_{V(t)} \left(\frac{1}{2}\rho v^2 + \rho g y\right) dV = -\int_{S(t)} \left[\mathbf{n} \cdot \left(\frac{1}{2}\rho v^2 + \rho g y\right)(\mathbf{v} - \mathbf{v_B})\right] dS - \int_{S(t)} (\mathbf{n} \cdot p\mathbf{v}) dS, \tag{3.6}$$

where $\mathbf{v_B}$ represents the boundary velocity of fluid field.

4. Results of Test Case and Discussions

4.1. Verification of the Present Numerical Method

In this section, two kinds of water-entry models of 2D free-falling wedge are created and numerically simulated to validate the present method by comparing the calculated results with experimental data of Zhao and Faltinsen [1] and Sun et al. [2].

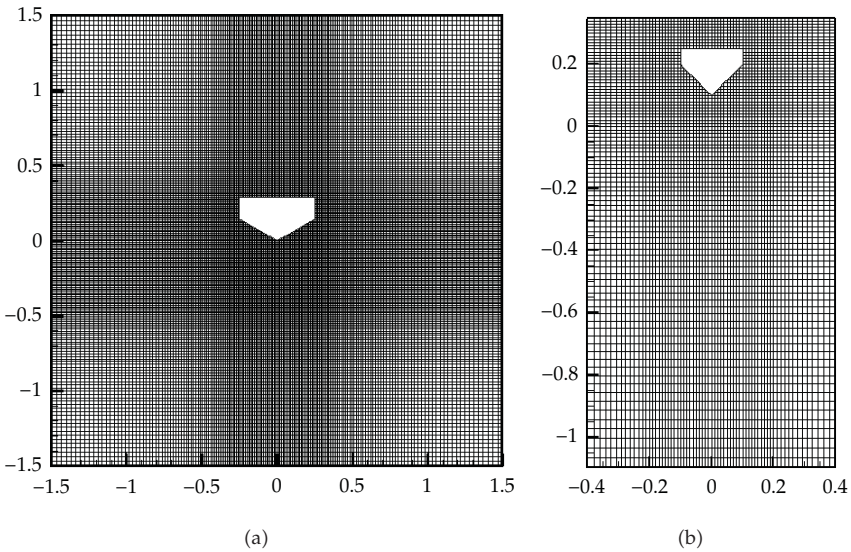

Figure 1: Global mesh of test model 1 (a) and test model 2 (b) in fluid field.

The first test model was created on a square domain of 3 m×3 m half occupied by water and half by air, and the wedge with 30° was 0.5 m wide, 0.29 m high, and 241 kg weight. The zero time ($t = 0$) of this case was selected as the moment that the apex of wedge contacts the initial calm free surface. Here for the comparison with experimental data as described by Zhao and Faltinsen [1], the initial velocity of wedge was prescribed as −6.15 m/s. On the other hand, for the second test model, the computational domain was a square of 0.8 m × 1.45 m, and the water depth was 1.1 m. Furthermore, the wedge with 45° was 0.6 m long, 0.2 m wide, and 7.787 kg weight. The zero physical time ($t = 0$) was the moment that the apex of wedge is 0.1 m up from the initial free surface, and then the wedge begun to fall freely.

In numerical calculation, the physical time Δt was 0.0001 s, the fictitious time $\Delta\tau$ was 0.01 s, the artificial compressibility coefficient β was 500, ω was taken as 0.8, and the gravity acceleration was 9.81 m/s^2.

Furthermore near solid boundary, the local meshes with equal spacing $\Delta x = \Delta y =$ 0.01 m were refined and regular, and then the mesh size gradually enlarged away from boundary. Thus, the inhomogeneous meshes (180 × 190 for model 1 and 66 × 90 for model 2) were generated in fluid field as shown in Figure 1.

In Figure 2, the time histories of hydrodynamic and acceleration versus numerical results and experiment are described and compared, F_h is the hydrodynamic on wedge, a is the acceleration of wedge, and t is the physical time. From the figure, it can be found that the numerical results of the present method are in good agreement with the experimental data of Zhao and Faltinsen [1] and Sun et al. [2]. Furthermore, it should be noted that there is a little difference about peak value in acceleration curve of Figure 2(b), which may be caused by the decrease of wedge velocity on the initial water-entry moment due to the resistance of experimental equipment.

Thus, the present method in this paper can be verified to be available and feasible for the study of free-falling wedge during water-entry phase. Furthermore, in order to make a long-time analysis on the energy transport and control the reflection of left and right

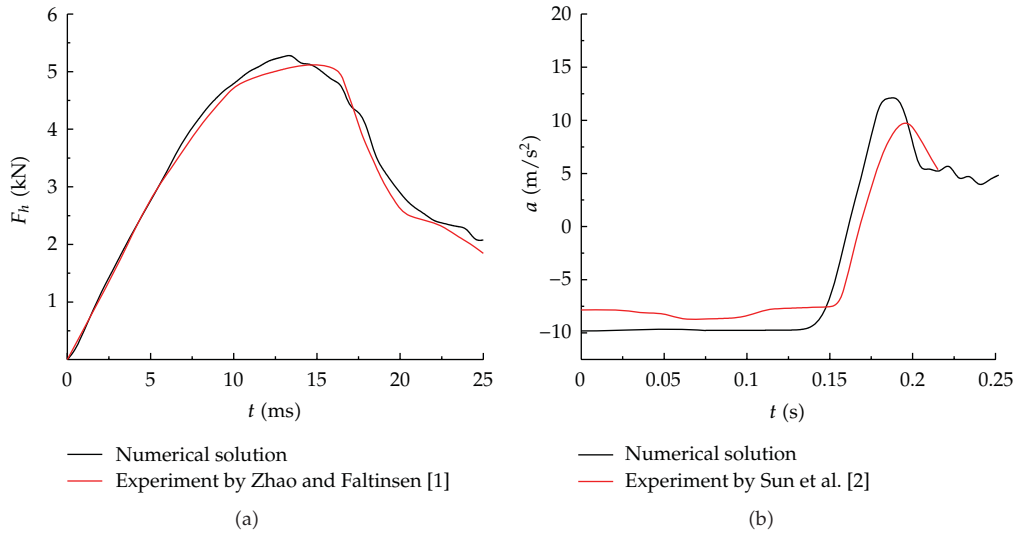

Figure 2: Comparison between numerical solutions of hydrodynamic (a); wedge acceleration (b) and experiment data of Zhao and Faltinsen [1] and Sun et al. [2].

boundaries, based on the test model 2, the width of computational domain is broaden from 0.8 m to 1.65 m in the following numerical simulation.

4.2. Macroscopic Energy Conversion of Overall Wedge-Fluid System

4.2.1. Change of Mechanical Energy for Free-Falling Wedge

At the initial moment, the wedge is 0.1 m up from the calm free surface and then begins to fall freely. During the whole motion process, the total mechanical energy (kinetic and potential energy) of wedge continuously changes as follows:

$$\begin{aligned} \frac{d}{dt}\left(\frac{1}{2}m{v_S}^2 + mgy_S\right) &= \mathbf{F}_h \cdot \mathbf{v_S}, \\ \frac{d}{dt}\left(\frac{1}{2}m{v_S}^2\right) &= m\mathbf{g} \cdot \mathbf{v_S} + \mathbf{F}_h \cdot \mathbf{v_S}, \\ \frac{d}{dt}(mgy_S) &= -m\mathbf{g} \cdot \mathbf{v_S}, \end{aligned} \tag{4.1}$$

where y_S is the vertical coordinate of wedge center, $\mathbf{v_S} = v_S\mathbf{j}$ is the velocity vector of wedge, $\mathbf{F}_h$ is the hydrodynamic on wedge, $\mathbf{g} = g\mathbf{j}$ is the vector of gravity acceleration, $mv_S{}^2/2$ is the kinetic energy of wedge, and mgy_S is the potential energy of wedge (here $y = 0$ is selected as zero position of potential energy).

In Figure 3, the time histories of variation rate for total mechanical energy, hydrodynamic and velocity of free-falling wedge are shown, dE/dt is the variation rate of total energy, and v_S is the body velocity. From the figure, it can be found that based on the movement characteristic of wedge at various time intervals, the whole motion process can be classified into three phases. Firstly, before the wedge impacts water surface, the hydrodynamic on

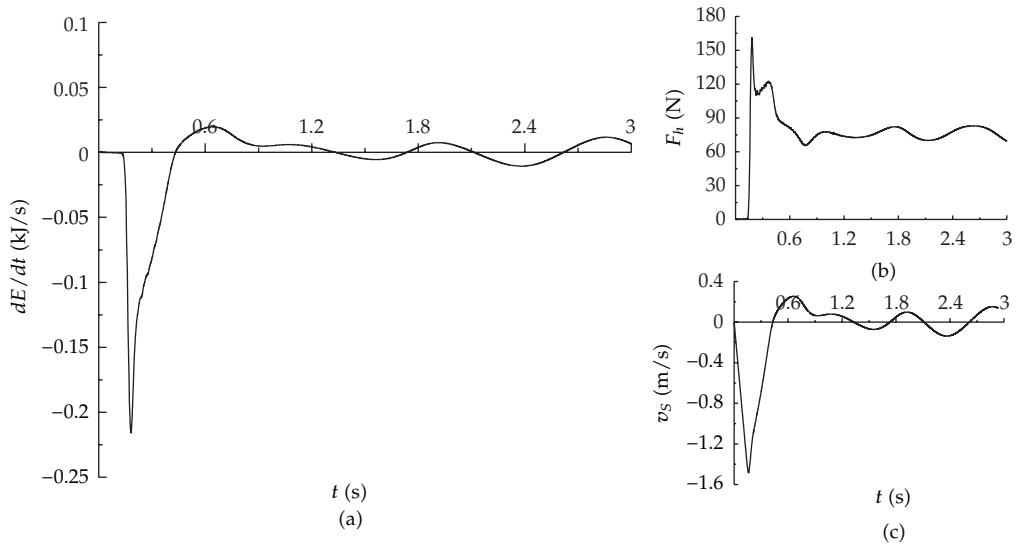

Figure 3: Time histories of variation rate for total energy (a), hydrodynamic (b), and velocity (c) of free-falling wedge.

wedge is very small and can be neglected. Thus, wedge keeps accelerating downward in air. Meanwhile, the total mechanical energy of wedge basically remains unchanged. Secondly, wedge affects free surface and then enters water. On this time interval, the hydrodynamic on solid boundary suddenly and rapidly heightens, which cause the wedge to reduce the speed. Hence, the mechanical energy of wedge gradually decrease and transfer to fluid field. As the wedge further travels in water, by hydrodynamic on wedge, the body velocity becomes less and less. Thirdly, until time advances to about 0.43 s, the velocity of wedge reduces to zero and will become opposite direction. From then on, the wedge moves up and down with small amplitude, which causes the mechanical energy of overall system to alternately convert between wedge and fluid field.

Here time histories of accumulative variation of energy and its ratio for free-falling wedge are shown in the Figure 4, dE is the accumulative variation of energy, work done by fluid is the accumulative energy transport from wedge to fluid field. The energy conversion of wedge during the whole motion process can be well described in this figure. For the first phase of wedge moving in air, the potential energy of wedge becomes basically kinetic energy of body. Then in the second stage of initial water-entry, the decrease of potential is equal to the sum of kinetic energy addition of wedge and increase of fluid energy. Finally, in the third time interval the wedge moves up and down. From the figure, it can be found that the kinetic energy of wedge tends to zero, and the potential energy of wedge and fluid energy can change each other. Therefore, it can be concluded that during the water-entry phase the variation of potential energy of free-falling wedge is the essential source of energy transport of overall system.

4.2.2. Macroscopic Energy Transport for Whole Fluid Field

In order to study the macroscopic energy transport of fluid field, here based on (3.6) the various boundaries of fluid field for water-entry model should be discussed firstly.

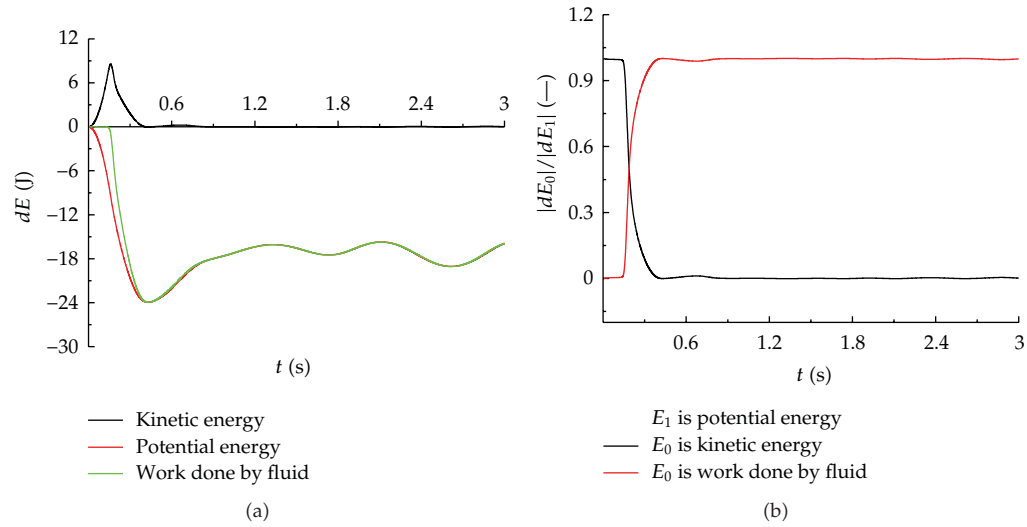

Figure 4: Time histories of accumulative variation of energy (a) and its ratio (b) for free-falling wedge.

For the computation domain, up edge is open and outlet boundary, solid edges of wedge are moving wall boundary, and left, down, and right edges are fixed wall boundary. Thus, on the up boundary $v_B = 0$, on the solid boundaries of wedge $\mathbf{n} \cdot \mathbf{v} = \mathbf{n} \cdot \mathbf{v_S} \neq 0$, and on the fixed boundary (left, down, and right edges) $\mathbf{n} \cdot \mathbf{v} = \mathbf{n} \cdot \mathbf{v_B} = 0$ should be used. On this basis, (3.6) related to water-entry model can be simplified as

$$\frac{d}{dt}\int_{V(t)}\left(\frac{1}{2}\rho v^2 + \rho g y\right)dV = -\int_{\text{up}}\left[\mathbf{n}\cdot\left(\frac{1}{2}\rho v^2 + \rho g y\right)\mathbf{v}\right]dS - \int_{\text{up}}(\mathbf{n}\cdot p\mathbf{v})dS - \int_{\text{rigid}}(\mathbf{n}\cdot p\mathbf{v_S})dS. \tag{4.2}$$

In this equation, $d[\int_{V(t)}(\rho v^2/2 + \rho g y)dV]/dt$ is the increase rate of kinetic plus potential energy in fluid field, $-\int_{\text{up}}[\mathbf{n}\cdot(\rho v^2/2 + \rho g y)\mathbf{v}]dS$ is the rate of kinetic and potential energy addition of fluid field from up boundary by convection, $-\int_{\text{up}}(\mathbf{n}\cdot p\mathbf{v})dS$ is the rate of work done by pressure on up boundary, and $-\int_{\text{rigid}}(\mathbf{n}\cdot p\mathbf{v_S})dS$ is the rate of work done by pressure on solid boundary of wedge.

Based on the Helmholtz velocity decomposing theorem, the fluid velocity can be written as

$$V_x = V_{xO} + \varepsilon_x dx + \gamma dy - \omega dy, \tag{4.3}$$

$$V_y = V_{yO} + \varepsilon_y dy + \gamma dx + \omega dx, \tag{4.4}$$

where V_{xO} and V_{yO} are the x- and y-translational fluid velocities versus point O, $\varepsilon_x = \partial V_x/\partial x$ and $\varepsilon_y = \partial V_y/\partial y$ are x and y-linear deforming velocities of fluid, $\gamma = (\partial V_x/\partial y + \partial V_y/\partial x)/2$ is the shearing deformation velocity of fluid, $\omega = (\partial V_y/\partial x - \partial V_x/\partial y)/2$ is the rotation angular velocity around point O, and $\mathbf{r} = dx\mathbf{i} + dy\mathbf{j}$ is the position vector to point O.

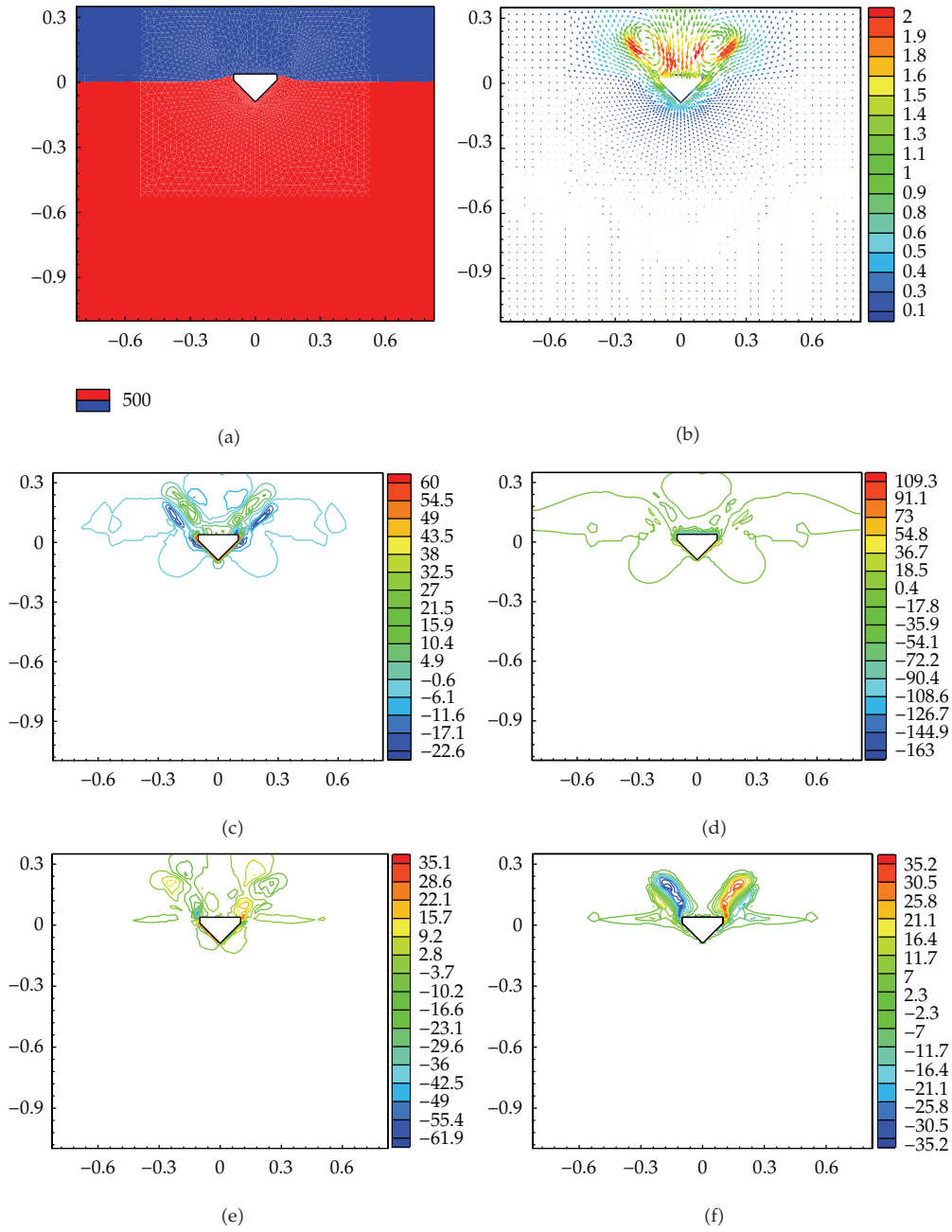

Figure 5: Information of fluid motion at the moment of 0.21 s. (a) free surface; (b) velocity vector; (c) x- and (d) y-linear-deforming velocities; (e) shearing deformation velocity; (f) rotation angular velocity.

In order to accurately and reasonably calculate the $d[\int_{V(t)}(\rho v^2/2 + \rho g y)dV]/dt$, here the fluid motion for water-entry model of free-falling wedge should be discussed.

In Figure 5, the free surface, velocity vector, x- and y-linear deforming, shearing deformation, and rotation angular velocity at the moment of 0.21 s are demonstrated. From

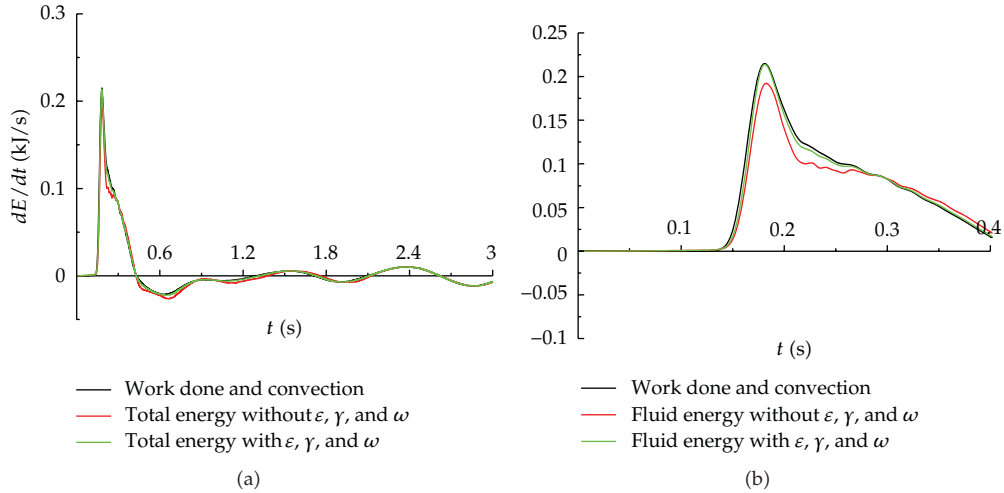

Figure 6: Time histories of numerical solutions for rate of work done and convection addition to fluid field and increase of fluid energy without or with consideration of ε, γ and ω during the whole and initial water-entry phase.

this figure, it can be found that for the water-entry model with air and water, the fluid is not only rotational motion, but also includes linear and shearing deformation.

Besides, Figure 6 shows the time histories of numerical solutions for rate of work done and convection in addition to fluid field and increase of fluid energy without or with consideration of ε, γ and ω during the whole and initial water-entry phase, ε_x and ε_y are x and y-linear deforming, γ is the shearing deformation, and ω is rotation angular velocity. As shown in this figure, the results shows that in the calculation of fluid energy by finite volume method for the water-entry model with both water and air, neglecting the influence of ε, γ, and ω may produce numerical error. Thus in order to more accurately predict the energy variation of entire fluid filed, fluid rotational motion and deformation should be taken into account in the numerical FVM method.

In Figure 7, time histories of accumulative variation of energy and its ratio in fluid field are demonstrated, and the increase of total energy in fluid field comes from the work done and convection on boundaries. Here the accumulative variation of energy and its ratio are also analyzed in three time intervals. In the first stage, the wedge has not yet entered water. It can be found that the potential energy in fluid field still remain unchanged from the figure. Next for the second phase, the wedge moves through water surface. Increase of total energy all become kinetic and potential energy in fluid field. Finally, in the third time interval, with the time advancing the wedge moves up and down, which cause the ratio of kinetic and potential to total energy to have a little oscillation around 25% and 75%, respectively.

Moreover, it should be noted that in the third phase the variation of fluid energy is repeated plus-minus oscillation, so in order to clearly and definitely discuss and analyze the transport phenomena of fluid energy for water-entry model of free-falling wedge, in the following study the calculation time range is selected from 0–0.4 s, which is the time interval of fluid energy monotonously increasing.

Figure 8 demonstrates time histories versus ratio (a) and rate (b) of energy variation in fluid field during the initial water-entry moment. From Figure 8(a), it can be obtained that the ratio of work done by wedge to increase fluid energy is approximately equal to 1.0, which

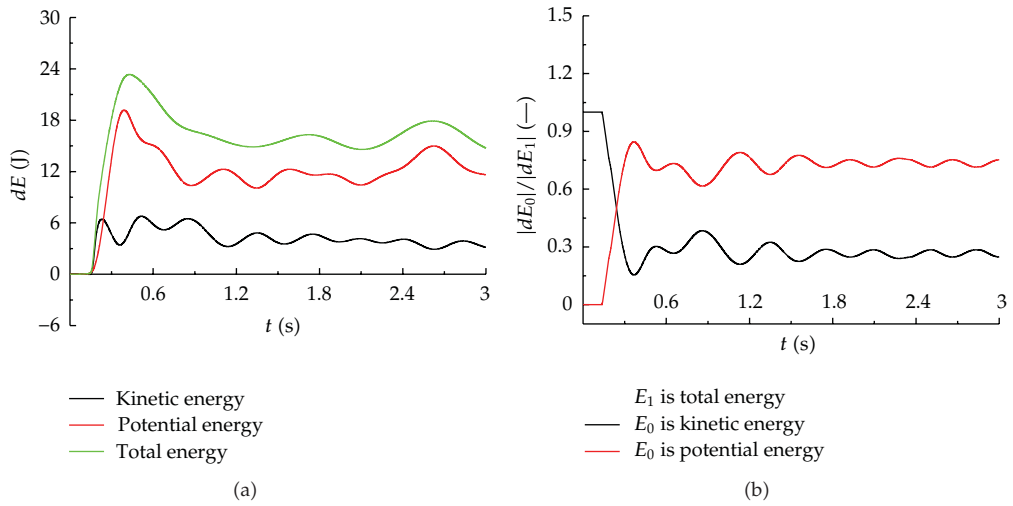

Figure 7: Time histories of accumulative variation of energy (a) and its ratio (b) in fluid field.

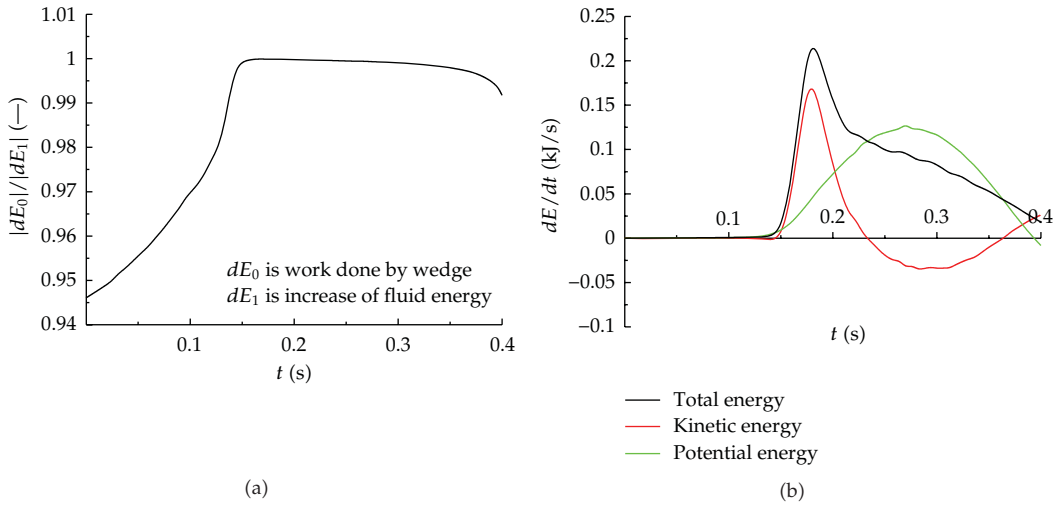

Figure 8: Time histories versus ratio (a) and rate (b) of energy variation in fluid field during the initial water-entry moment.

shows that work done by wedge is the main origin and reason for the change and transport of fluid energy.

Furthermore, the variation rates versus kinetic, potential and total energy are drawn in Figure 8(b), which can describe the transport phenomena of fluid energy by combining with fluid motion. During the time interval of wedge moving in air, the hydrodynamic on wedge is very small, so the rates of kinetic, potential, and total energy in fluid field are minute and approximate to zero. In the initial phase of water-entry, impulse hydrodynamic with high-pressure peaks on wedge causes fluid particle near solid boundary to accelerate and free surface to rise up, which will result in the rapid increase of kinetic and steadily enhancement of potential energy. As the wedge pieces through free surface, the pressuring effect of wedge on fluid reduces, and the rate of kinetic energy in fluid field gradually decreases. With

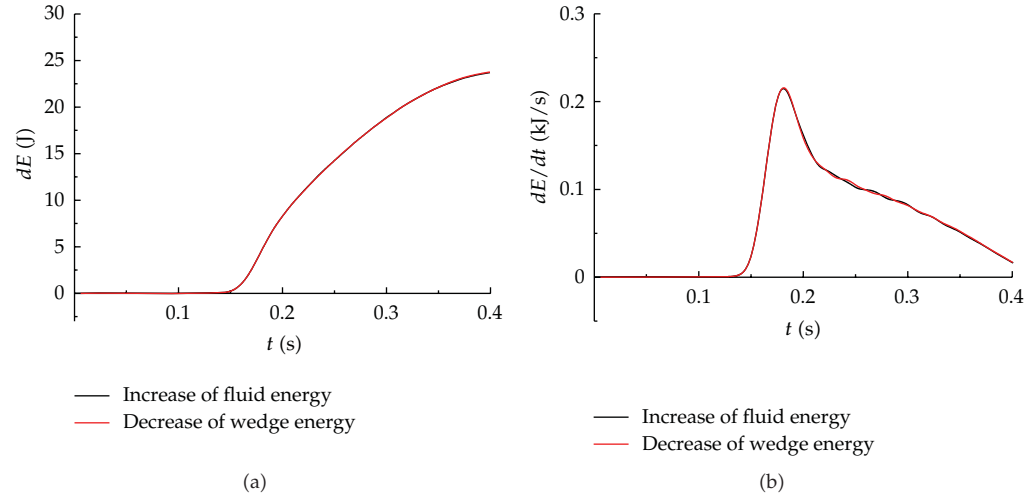

Figure 9: Comparison of value and its rate versus increase of fluid energy and decrease of wedge energy during the initial water-entry phase.

physical time advancing, due to the further reduction of fluid pressure and decelerating effect of gravity, the rate of kinetic energy becomes negative. However, at this moment the global direction of fluid velocity near free surface is still upward, which cause the potential energy to continuously heighten. As the wedge further travels into water, for the sake of gravity, the fluid near free surface ultimately will fall down, the rate of potential energy in fluid field will be negative, and meanwhile the kinetic energy will accordingly improve.

4.2.3. Validity of Energy Conservation of Overall Body-Fluid System

The increase and its rate of fluid energy and decrease of wedge energy are compared in Figure 9. From the figure, it is obvious that both variations of fluid and wedge energy are almost the same, and a very little difference may be caused by the minute work done or convection on up boundary. Therefore, it can be concluded that energy conservation of overall system can be satisfied in current numerical method.

4.3. Microscopic Energy Transformation in Fluid Field

In this section, for further and better studying how fluid energy changes and transports, some microscopic details in fluid field (such as velocity vector, pressure gradient, and distribution of transient variation for kinetic and potential energy) are discussed at three classic moments (t = 0.06, 0.18, and 0.27 s), which are chosen from Figure 8.

At t = 0.06 s, the wedge has not contacted and affected free surface yet, and the information about the change of fluid energy in air can be described and studied as in Figure 10 .

In Figure 10, microscopic details of fluid energy at t = 0.06 s are described. Firstly based on (3.2) and (3.4), various influential factors on the change of fluid energy are shown in Figures 10(c)–10(j), respectively, which are successively the convective transport of kinetic energy $-(\nabla \cdot (\rho v^2/2)\mathbf{v})$, convective vector of kinetic energy (from high to low) $-\nabla \cdot (\rho v^2/2)$,

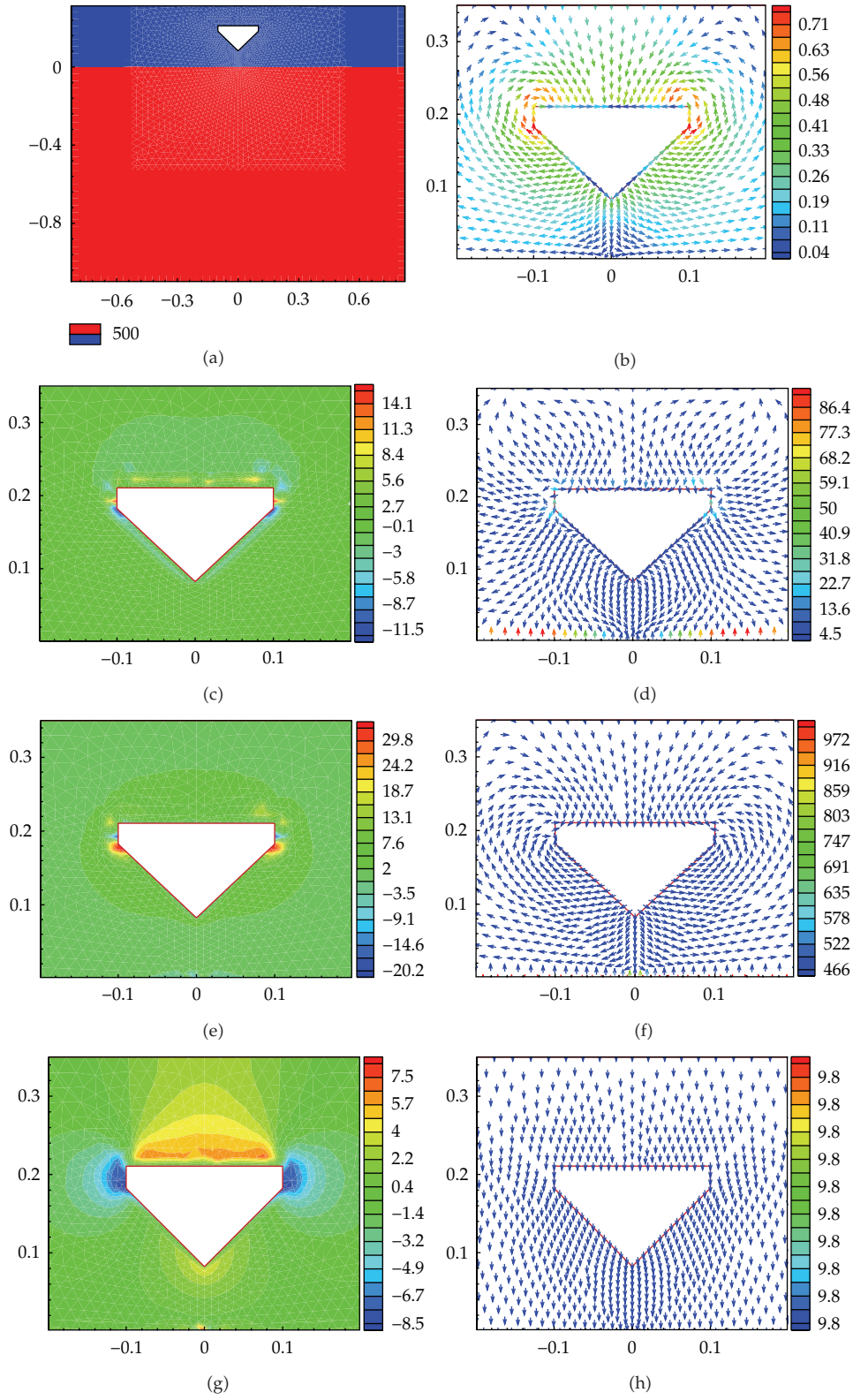

Figure 10: Continued.

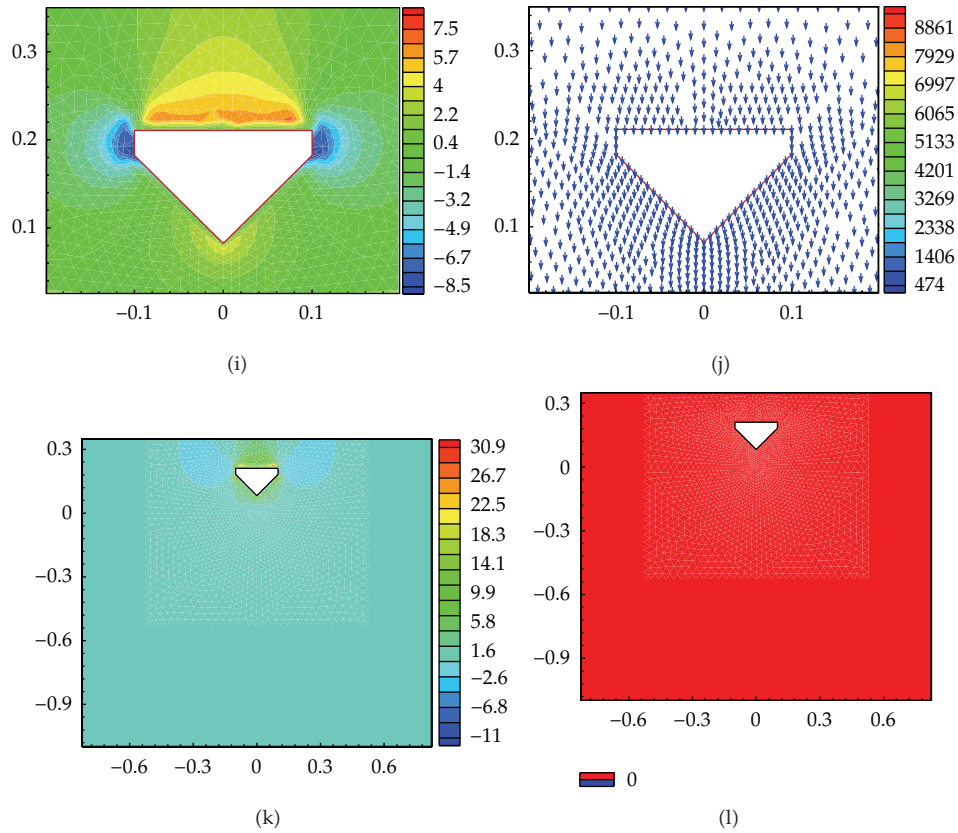

Figure 10: Microscopic details of fluid energy at $t = 0.06$ s. (a) free surface profile; (b) velocity vector; (c) convection of kinetic energy; (d) convective vector of kinetic energy (high to low); (e) work done by pressure; (f) convective vector of pressure; (g) work done by gravity; (h) gravity vector; (i) convection of potential energy; (j) convective vector of potential energy; (k) transient change of kinetic energy; (l) transient change of potential energy.

work done by pressure $-(\nabla p \cdot \mathbf{v})$, convective vector of pressure $-\nabla p$, work done by gravity $\rho(\mathbf{v} \cdot \mathbf{B})$, gravity vector $\mathbf{B}$, convection of potential energy $-(\nabla \cdot (\rho g y)\mathbf{v})$, and convective vector of potential energy $-\nabla \cdot (\rho g y)$. From the figure, it can be found that the effect of these above-mentioned factors on change of fluid energy is related to the direction and value of fluid velocity. Now take Figures 10(e) and 10(f) for example, and Figure 10(f) shows the convective direction of fluid pressure (from high to low). By comparing convective vector of pressure with the velocity vector of Figure 10(b), it is obvious that the directions versus the above two kinds of vectors are the same in most areas, except a small local zone near both straight edges of wedge, which results in the regional distribution about the increase or decrease of fluid energy in Figure 10(e). Besides as shown in Figure 10(b), the fluid velocities are up to maximum on the both corners of wedge. Thus in Figure 10(e), there are two deep red zones with highest rate of energy addition by work done by pressure on the corners of wedge according to fluid velocity. By synthetically analyzing all influential factors, the transient changes of kinetic energy $\partial(\rho v^2/2)/\partial t$ and potential energy $\partial(\rho g y)/\partial t$ can be described in Figures 10(k) and 10(l). From the figure, because the convection of potential energy and work done by gravity is almost the same, the potential energy will remain unchanged as shown

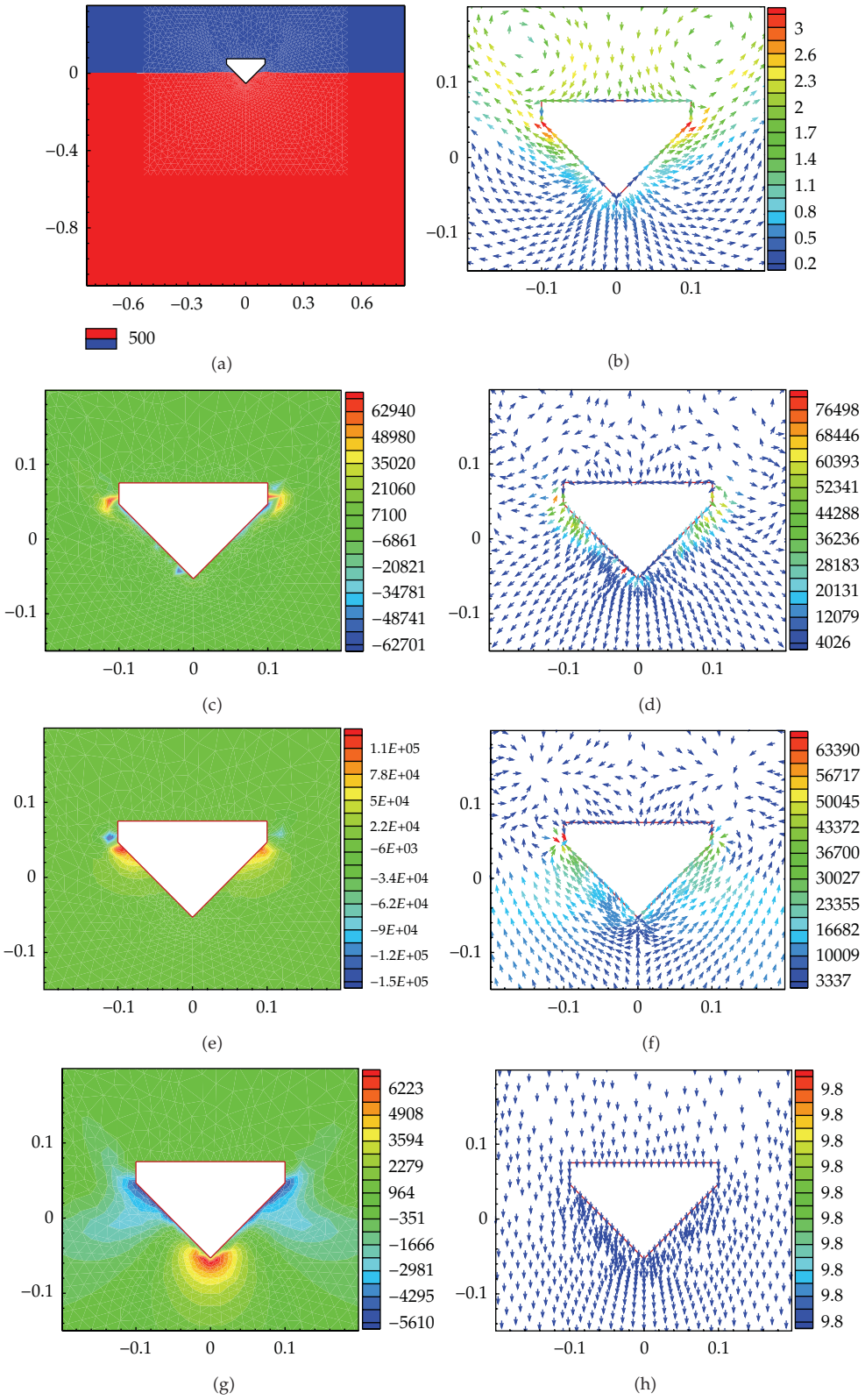

Figure 11: Continued.

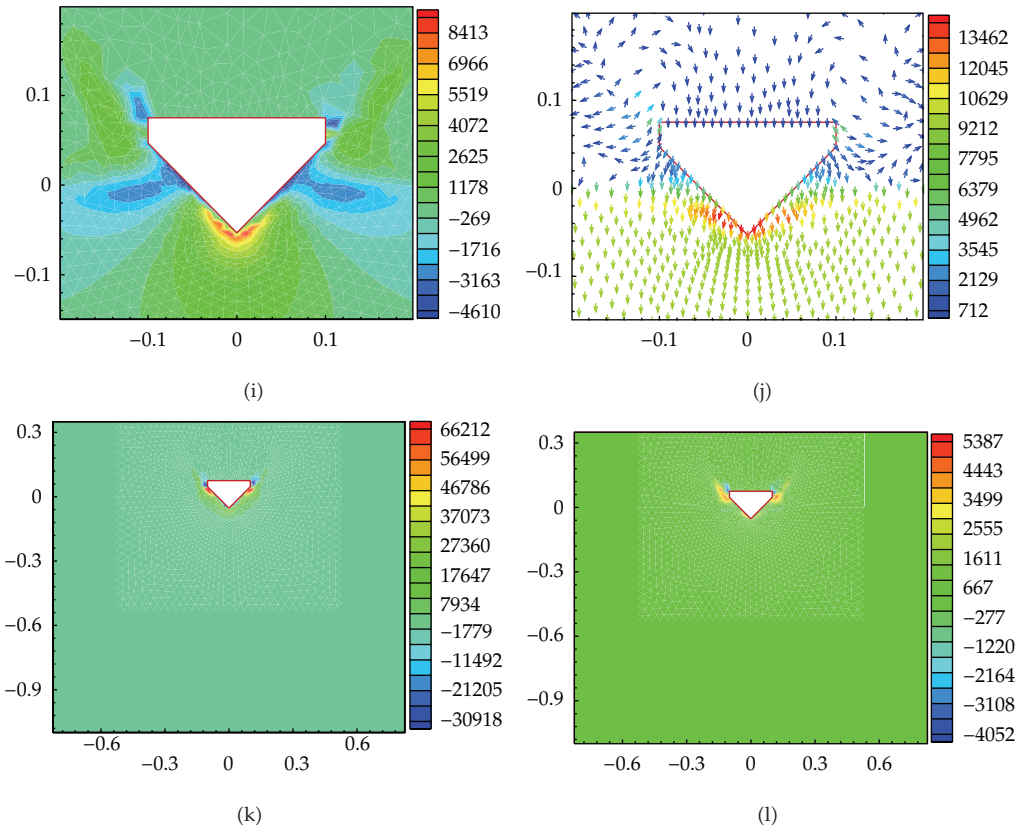

Figure 11: Microscopic details of fluid energy at $t = 0.18$ s. (a) free surface profile; (b) velocity vector; (c) convection of kinetic energy; (d) convective vector of kinetic energy (high to low); (e) work done by pressure; (f) convective vector of pressure; (g) work done by gravity; (h) gravity vector; (i) convection of potential energy; (j) convective vector of potential energy; (k) transient change of kinetic energy; (l) transient change of potential energy.

in Figure 10(l). On the other hand, due to the influence of convective transport and work done by pressure and gravity, the kinetic energy will vary just near the solid boundary of wedge. Furthermore, only in very minute area on the both straight edges of wedge, the color of Figure 10(k) is deep blue, where the kinetic energy of fluid field will most quickly reduce. But in other zones near wedge the kinetic energy will more or less increase.

Figure 11 demonstrates microscopic information of fluid energy at $t = 0.18$ s. From Figures 11(a) and 11(b), it can be found that on this moment the wedge is piercing the free surface, and water rises up along the slope edges, and the displacement waves are formed. Meanwhile, the air between the body and free surface escapes and separates at the corner of wedge to form a pair of symmetric vortices. All influential effects on the change of fluid energy are shown in Figures 11(c)–11(j), respectively and then studied to achieve the distribution of transient changes of kinetic and potential energy as shown in Figures 11(k) and 11(l). At $t = 0.18$ s, the wedge has entered water and forces free surface to rise upward, which results in the increase of potential energy along both slope edges of wedge in Figure 11(l). Furthermore, according to the convection and work done in Figures 11(c), 11(e), and 11(g), it can be obtained that the work done of pressure is main reason of energy variation

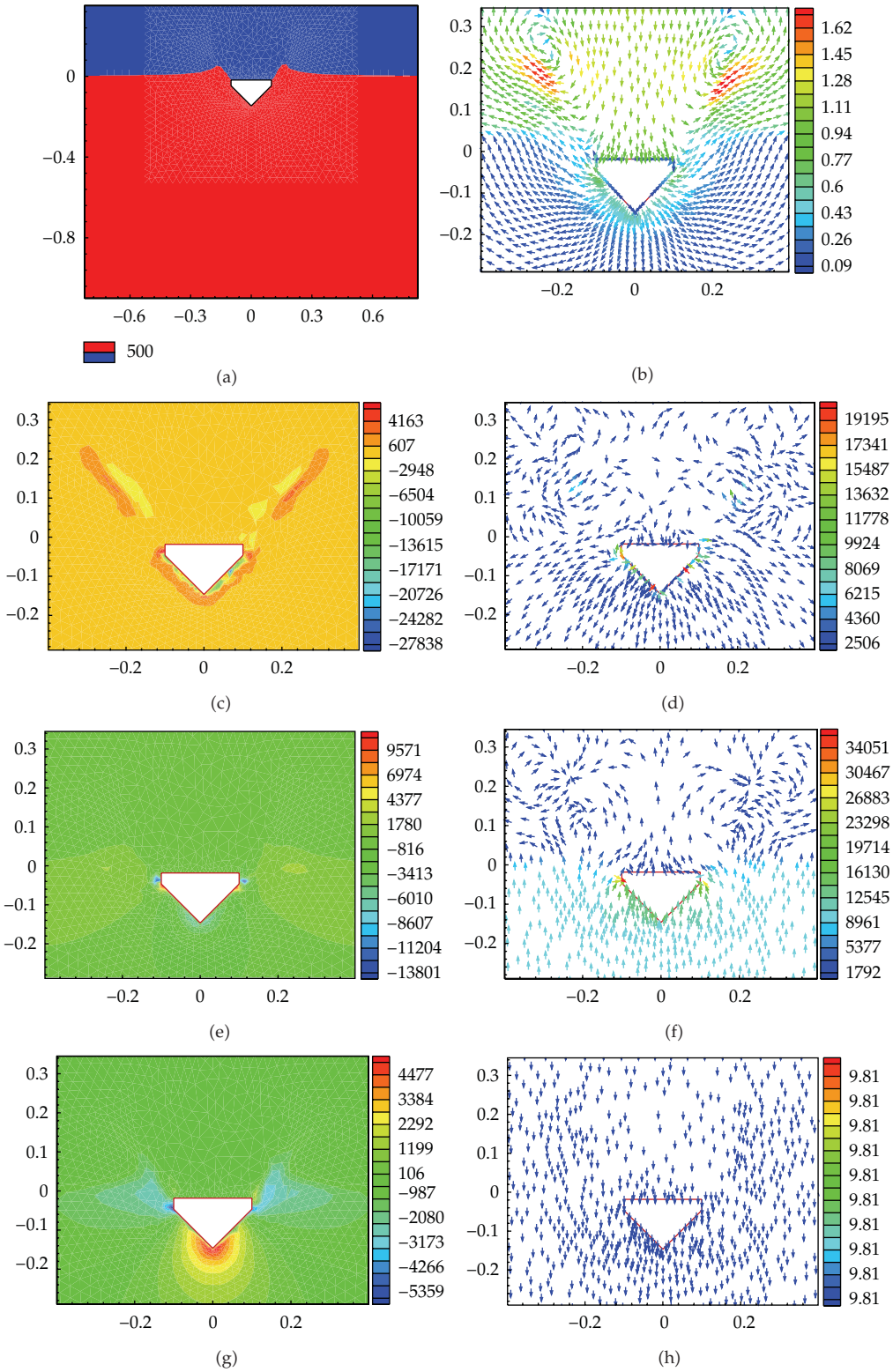

Figure 12: Continued.

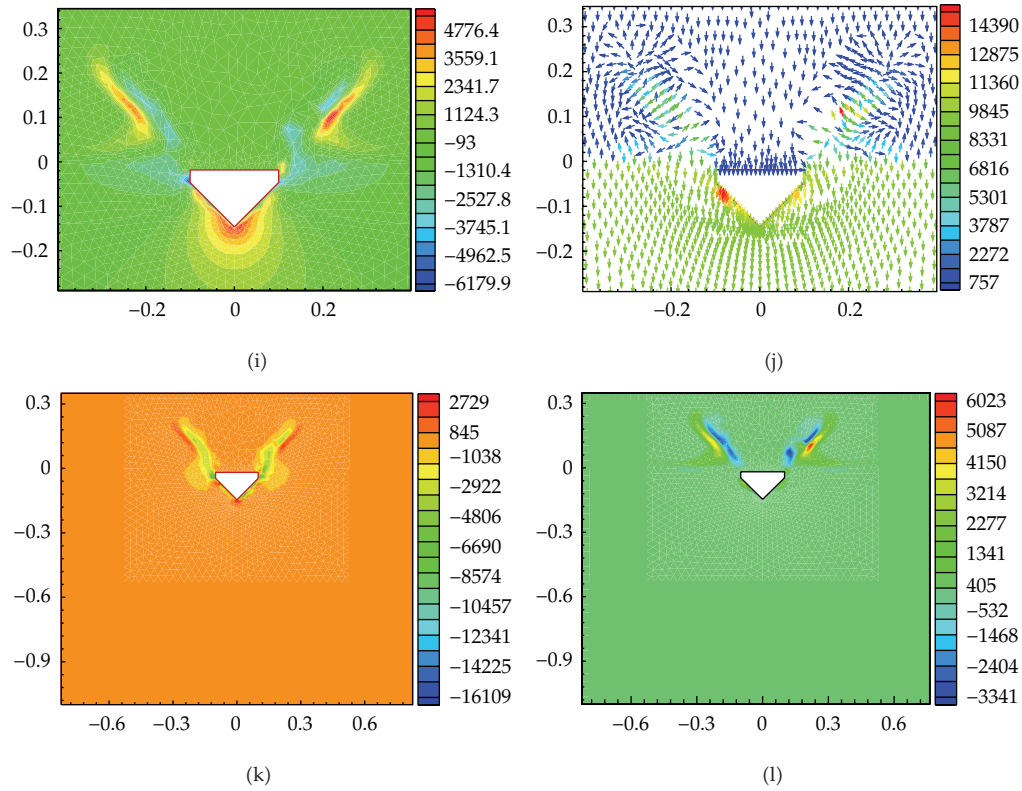

Figure 12: Microscopic details of fluid energy at $t = 0.27$ s. (a) free surface profile; (b) velocity vector; (c) convection of kinetic energy; (d) convective vector of kinetic energy (high to low); (e) work done by pressure; (f) convective vector of pressure; (g) work done by gravity; (h) gravity vector; (i) convection of potential energy; (j) convective vector of potential energy; (k) transient change of kinetic energy; (l) transient change of potential energy.

for kinetic energy. In Figure 11(f), due to the motion characteristic of free-falling wedge at $t = 0.18$ s, there are two prominent low-pressure zones at both corners of wedge, which cause remarkable increase on both slope edges and great decrease on both straight edges for the work done by pressure and kinetic energy versus Figures 11(e) and 11(k), respectively.

The fluid details about kinetic and potential energy at $t = 0.27$ s are drawn in Figure 12. At this time, the two intersections between wedge and free surface have been to the highest point of both straight sides, and the two air vortices are far away from wedge. In the same way, various influential effects on the variation of fluid energy can be achieved in Figures 12(c)–12(j), and on this basis the distribution of transient transformation of kinetic and potential energy are demonstrated in Figures 12(k) and 12(l). As shown in these figures, the present location and movement trend of free surface determine the color distribution of transient change for kinetic and potential energy, that is, the zone with yellow-green color in Figure 12(k) or blue color of Figure 12(l) represents the present location of free surface which will move toward the area with red color in Figure 12(k) or red-yellow color of Figure 12(l). Furthermore, by analyzing the difference of value among various contours, it can be found that at this moment the free surface will move up and outwards with less and less velocity, which causes the increase of potential energy and decrease of kinetic energy.

Finally by synthetically analyzing Figures 10–12, it can be concluded that in fluid field the variation of kinetic and potential energy just locally takes place near wedge and free surface. Furthermore, by comparing Figures 10–12 with each other, the rate of variation for kinetic and potential energy at $t = 0.06$ s is relatively minute. Next, at $t = 0.18$ s, the kinetic and potential energy present a fast growth tendency, and the rate of variation for kinetic energy is relatively maximum. Finally, on the moment of $t = 0.27$ s, the rate of potential energy is positive and relatively maximum, but the kinetic energy in fluid field globally appears to be a downward trend. Thus, the microscopic information of fluid energy in Figures 10, 11, and 12 can well verify and support the macroscopic variation trend of kinetic and potential energy of fluid field in Figure 8.

5. Conclusions

In this paper, a free surface capturing method and Cartesian cut cell mesh are used to numerically simulate the water-entry model of free-falling wedge. By means of the calculated results, the physical phenomena and mechanical energy transports of body-fluid interactive system are studied from macroscopic energy conversion of overall body-fluid system and microscopic energy transformation in fluid field. Finally some useful conclusions can be made as follows:

(1) by the present method of this paper, energy conservation is always satisfied in the whole phase of numerical calculation;

(2) for water-entry model of free-falling wedge with both air and water, the fluid motion includes not only rotation angular velocity but also linear and shearing deformation, which will have an influence on the numerical calculation of fluid energy by finite volume method and should be taken into account;

(3) during the initial phase of water-entry, for the overall system the variation of potential energy of free-falling wedge is the essential source of energy transport, which should change the kinetic energy of wedge, kinetic energy, and potential energy of fluid;

(4) during the initial phase of water-entry of free-falling wedge, compared with the work done by wedge, the energy transport from open boundary can be neglected for the variation of fluid energy. Furthermore, the gradient of fluid pressure caused by wedge is the basic and original cause of fluid motion and energy transport in fluid field;

(5) during the initial phase of water-entry of free-falling wedge, the change regularities of kinetic and potential energy in fluid field are studied and successfully associated with the fluid motion.

Furthermore, in the future research other water-entry problems (such as water-entry with constant velocity and water-entry of elastic body) should be studied and analyzed.

References

[1] R. Zhao and O. M. Faltinsen, "Water entry of arbitrary two-dimensional sections with and without flow separation," in *Twenty-first Symposium. On Naval Hydrodynamics*, National Academy, Washington, DC, USA, 1997.

[2] H. Sun, Z. H. Lu, and Y. S. He, "Experimental research on the fluid-structure interaction in water entry of 2D elastic wedge," *Journal of Hydrodynamics*, vol. 18, no. 1, pp. 104–109, 2003.
[3] T. Bunnik and B. Buchner, "Numerical prediction of wave loads on subsea structures in the splash zone," in *Proceedings of the 14th International Offshore and Polar Engineering Conference*, pp. 284–290, Toulon, France, 2004.
[4] W. H. Wang and Y. Y. Wang, "An improved free surface capturing method based on Cartesian cut cell mesh for water-entry and exit problems," *Proceedings of the Royal Society A*, vol. 465, no. 2106, pp. 1843–1868, 2009.
[5] L. Qian, D. M. Causon, D. M. Ingram et al., "A free-surface capturing method for two fluid flows with moving bodies," *Proceedings of the Royal Society A*, vol. 462, no. 2065, pp. 21–42, 2006.
[6] F. J. Kelecy and R. H. Pletcher, "The development of a free surface capturing approach for multidimensional free surface flows in closed containers," *Journal of Computational Physics*, vol. 138, no. 2, pp. 939–980, 1997.
[7] D. Pan and C. H. Chang, "The capturing of free surfaces in incompressible multi-fluid flows," *International Journal for Numerical Methods in Fluids*, vol. 33, no. 2, pp. 203–222, 2000.
[8] G. Yang, D. M. Causon, D. M. Ingram, R. Saunders, and P. Batten, "A Cartesian cut cell method for compressible flows. Part A. Static body problems," *Aeronautical Journal*, vol. 101, no. 1002, pp. 47–56, 1997.
[9] G. Yang, D. M. Causon, D. M. Ingram, R. Saunders, and P. Battent, "A Cartesian cut cell method for compressible flows. Part B. Moving body problems," *Aeronautical Journal*, vol. 101, no. 1002, pp. 57–65, 1997.
[10] D. M. Causon, D. M. Ingram, and C. G. Mingham, "A Cartesian cut cell method for shallow water flows with moving boundaries," *Advances in Water Resources*, vol. 24, no. 8, pp. 899–911, 2001.
[11] P. L. Roe, "Approximate Riemann solvers, parameter vectors, and difference schemes," *Journal of Computational Physics*, vol. 43, no. 2, pp. 357–372, 1981.
[12] W. Y. Soh and J. W. Goodrich, "Unsteady solution of incompressible Navier-Stokes equations," *Journal of Computational Physics*, vol. 79, no. 1, pp. 113–134, 1988.
[13] F. J. Kelecy and R. H. Pletcher, "The development of a free surface capturing approach for multidimensional free surface flows in closed containers," *Journal of Computational Physics*, vol. 138, no. 2, pp. 939–980, 1997.
[14] R. B. Bird, W. E. Stewart, and E. N. Lightfoot, *Transport Phenomena*, John Wiley & Sons, 2nd edition, 2001.
[15] D. Pan and H. Lomax, "A new approximate LU factorization scheme for the Reynolds-averaged Navier-Stokes equations," *American Institute of Aeronautics and Astronautics*, vol. 26, no. 2, pp. 163–171, 1988.

Hindawi Publishing Corporation
Journal of Applied Mathematics
Volume 2012, Article ID 747410, 15 pages
doi:10.1155/2012/747410

Research Article

Inverse Estimation of Temperature Profiles in Landfills Using Heat Recovery Fluids Measurements

C. Solisio, A. P. Reverberi, A. Del Borghi, and V. G. Dovi'

Department of Chemical and Process Engineering "G. B. Bonino", University of Genova, Via Opera Pia 15, 16145 Genova, Italy

Correspondence should be addressed to V. G. Dovi', dovi@istic.unige.it

Received 8 December 2011; Accepted 4 March 2012

Academic Editor: Fu-Yun Zhao

In addition to leachate and gas emission analysis, temperature variations in municipal solid waste landfills are routinely monitored for safety and health reasons, such as the increased production of biogas or the danger of spontaneous combustion phenomena if the temperature exceeds 70–75°C. The increasing constraints on greenhouse gas emissions and the convenience of fuel and heat recovery have helped develop a global approach to landfills' operation and maintenance, generally referred to as bioreactor landfill management. The heat recovery piping we are presently designing can be a significant part of this approach. The heat gained by a fluid circulated in a closed network through the landfill is transferred to an external heat exchanger or used directly as warm water. Additionally, it can help reduce landfill temperature levels and control biogas generation. Since the pipes diameter is large enough to allow for a radial temperature gradient, this information can be used for an inverse estimation of the temperature profile in the landfill which constitutes the boundary conditions of the resulting heat transfer problem. In this paper, we describe an algorithm for regularising the resulting ill-posed free boundary estimation problem using sampled data of the heat recovery fluid on exiting the landfill.

1. Introduction

A new approach to landfills' operation and maintenance, generally referred to as "bioreactor landfill management," is expected to reduce the amount of leachate and to increase the production of biogas, while reducing the amount of necessary land.

For the achievement of this result, leachate and gas emissions of municipal solid waste landfills are accurately analysed, whereas temperature variations are routinely monitored for safety and health reasons, such as the increased production of biogas or the danger of spontaneous combustion phenomena if the temperature exceeds 70–75°C [1].

Significant amounts of heat are produced in municipal landfills due to decomposition of organic solid wastes. While leachate and gas emissions have been the object of several

studies [2–4], less information is available on heat recovery technologies. However, they could be a significant part in the general bioreactor landfill management, as the heat gained by a fluid circulated in a closed network through the landfill can be transferred to an external heat exchanger or used directly as warm water adding to the overall energy saving strategy. Additionally, the heat removed can contribute to a reduction of temperature levels inside the landfill and to an alleviation of spontaneous combustion risks.

Since the diameter of the pipes carrying the heat recovery fluid is large enough to allow for a radial temperature gradient, this information can be used for an inverse estimation of the temperature profile in the landfill which constitutes the boundary conditions of the resulting heat transfer problem. This information can be combined with the measurements provided by *in situ* sensors (including thermocouples, thermistors, and vibrating wire piezometers) which have to withstand a corrosive aggressive environment and strong mechanical stresses. The simultaneous use of direct measurements provided by sensors and of estimates resulting from inverse temperature profile reconstructions can improve the overall thermal control in landfills.

The inverse estimation of the boundary conditions of a partial differential equations is known to be an ill-posed problem which requires suitable regularisation techniques to obtain stable and physically acceptable solutions.

In this paper, we employ a piecewise linear approximation to the unknown profile combined with a traditional Tikhonov regularisation technique [5]. The piecewise linear approximation of a boundary condition was first employed by the authors in the estimation of diffusivities in solids [6], where it was used in conjunction with separable least squares. In this paper, the method is extended to the thermal energy transfer of a fluid in stationary motion.

Exact simulated data are generated from an assumed smooth temperature profile with a spike to indicate the presence of a hot spot which might turn into a landfill fire. A Gaussian distributed error with zero mean and a standard deviation equal to the measurement precision is added to the exact data.

The reconstructions obtained by using different values for the number of intervals of the piecewise linear approximation and Tikhonov's regularisation parameter show the usefulness and the limitations of the method developed.

2. Theoretical Development

The temperature profile inside the pipes is determined by the transfer of heat from the soil to the fluid flowing in the pipes.

Assuming radial symmetry about the axis of the pipe and a flat velocity distribution across the section of pipe (which is a reasonable assumption due to the turbulent motion of the fluid), the energy balance can be written as [7]

$$\rho c_p u \frac{\partial T}{\partial x} = K \frac{1}{r} \frac{\partial}{\partial r}\left(r \frac{\partial T}{\partial r} \right), \tag{2.1}$$

$$\left(\frac{\partial T}{\partial r} \right)_{r=0} = 0, \tag{2.2}$$

$$T(0, r) = T_0, \tag{2.3}$$

$$-K \left(\frac{\partial T}{\partial r} \right)_{r=R} = H\left[T(x, R) - \varphi(x) \right], \tag{2.4}$$

where ρ is the density, c_P is the specific heat at constant pressure, u is the speed, and K is the conductivity of the fluid. R is the radius of the pipe, and x indicates the direction of motion. H is the heat transfer coefficient from the soil to the fluid (including wall resistance), and $\varphi(x)$ is the unknown temperature profile of the soil.

Setting $k = K/(\rho\ c_P\ u)$, (2.1) becomes

$$\frac{\partial T}{\partial x} = k\frac{1}{r}\frac{\partial}{\partial r}\left(r\frac{\partial T}{\partial r}\right). \tag{2.5}$$

This equation is formally equal to the transient heat conduction in an infinite circular cylinder [8].

The general analytical solution of (2.1)–(2.4) can be determined by applying Duhamel's principle [9] to the particular solution obtained assuming a constant temperature profile along the x direction.

Indeed, if the soil temperature profile is constant along x ($\varphi(x) = T^*$), the analytical solution is provided by the infinite series [8]

$$\frac{(T - T_0)}{(T^* - T_0)} = 1 - 2A\sum_{n=1}^{\infty} e^{-(\beta_n^2/R^2)kx}\frac{J_0\left((r/R)\beta_n\right)}{\left(\beta_n^2 + A^2\right)J_0(\beta_n)}, \tag{2.6}$$

where $A = RH$, J_0 is the Bessel function of order zero, and β_n are the roots of

$$\beta J_1(\beta) = AJ_0(\beta). \tag{2.7}$$

Combining this equation with Duhamel's principle, we obtain the general solution

$$T(r,x) - T_0 = \frac{2Ak}{R^2}\sum_{n=1}^{\infty}\beta_n e^{-(\beta_n^2/R^2)kx}\frac{J_0\left((r/R)\beta_n\right)}{\left(\beta_n^2 + A^2\right)J_0(\beta_n)}\int_0^x e^{(\beta_n^2/R^2)k\lambda}\varphi(\lambda)d\lambda. \tag{2.8}$$

Thus, if the temperature of the fluid $T(r,x)$ is measured at the exit of the landfill ($x = L$), the unknown soil temperature profile $\varphi(x)$ can be estimated.

Following the method developed in [6], let us approximate the profile by a continuous piecewise function $\psi(x)$ in the range $[0, L]$ divided into M equal intervals of width $h = L/M$,

$$\psi(x) = T_0 + h\sum_{i=1}^{k-1} c_i + c_k(x - x_{k-1}), \quad x_{k-1} \le x \le x_k, \tag{2.9}$$

where c_k is the angular coefficient of the linear approximation in the interval $x_{k-1} \le x \le x_k$.

The integrals in the infinite series can now be approximated by

$$\int_0^x e^{(\beta_n^2/R^2)k\lambda}\phi(\lambda)d\lambda = \int_0^{x_1} e^{(\beta_n^2/R^2)k\lambda}(T_0 + c_1\lambda)d\lambda + \int_{x_1}^{x_2} e^{(\beta_n^2/R^2)k\lambda}[T_0 + hc_1 + c_2(\lambda - x_1)]d\lambda + \cdots + \int_{x_{k-1}}^{x} e^{(\beta_n^2/R^2)k\lambda}\left[T_0 + h\sum_{i=1}^{k-1} c_i + c_k(\lambda - x_{k-1})\right]d\lambda, \quad x_{k-1} \le x \le x_k, \tag{2.10}$$

which can be rewritten as

$$\begin{aligned}
\int_0^x e^{(\beta_n^2/R^2)k\lambda}\phi(\lambda)d\lambda &= T_0\left\{\int_0^{x_1} e^{(\beta_n^2/R^2)k\lambda}d\lambda + \int_{x_1}^{x_2} e^{(\beta_n^2/R^2)k\lambda}d\lambda + \cdots + \int_{x_{k-1}}^{x} e^{(\beta_n^2/R^2)k\lambda}d\lambda\right\} \\
&\quad + c_1\left\{\int_0^{x_1} \lambda e^{(\beta_n^2/R^2)k\lambda}d\lambda + h\int_{x_1}^{x_2} e^{(\beta_n^2/R^2)k\lambda}d\lambda \right. \\
&\qquad \left. + \cdots + h\int_{x_{k-1}}^{x} e^{(\beta_n^2/R^2)k\lambda}d\lambda\right\} \\
&\quad + c_2\left\{\int_{x_1}^{x_2} (\lambda - x_1) e^{(\beta_n^2/R^2)k\lambda}d\lambda + h\int_{x_2}^{x_3} e^{(\beta_n^2/R^2)k\lambda}d\lambda \right. \\
&\qquad \left. + \cdots + h\int_{x_{k-1}}^{x} e^{(\beta_n^2/R^2)k\lambda}d\lambda\right\} \\
&\quad + c_3\left\{\int_{x_2}^{x_3} (\lambda - x_2) e^{(\beta_n^2/R^2)k\lambda}d\lambda + h\int_{x_3}^{x_4} e^{(\beta_n^2/R^2)k\lambda}d\lambda \right. \\
&\qquad \left. + \cdots + h\int_{x_{k-1}}^{x} e^{(\beta_n^2/R^2)k\lambda}d\lambda\right\} \\
&\quad + \cdots \\
&= \frac{T_0R^2}{k\beta_n^2}\left\{e^{(\beta_n^2/R^2)kx} - 1\right\} \\
&\quad + c_1\left\{\frac{R^2}{\beta_n^2k}x_1e^{(\beta_n^2/R^2)kx_1} - \left(\frac{R^2}{\beta_n^2k}\right)^2\left(e^{(\beta_n^2/R^2)kx_1} - 1\right)\right. \\
&\qquad \left. + \frac{hR^2}{\beta_n^2k}\left(e^{(\beta_n^2/R^2)kx} - e^{(\beta_n^2/R^2)kx_1}\right)\right\} \\
&\quad + c_2\left\{\frac{R^2}{\beta_n^2k}\left(x_2e^{(\beta_n^2/R^2)kx_2} - x_1e^{(\beta_n^2/R^2)kx_1}\right)\right.
\end{aligned}$$

$$
\begin{aligned}
&- \left(\frac{R^2}{\beta_n^2 k}\right)^2 \left(e^{(\beta_n^2/R^2)kx_2} - e^{(\beta_n^2/R^2)kx_1}\right) \\
&+ \frac{hR^2}{\beta_n^2 k}\left(e^{(\beta_n^2/R^2)kx} - e^{(\beta_n^2/R^2)kx_2}\right) \\
&- \frac{x_1 R^2}{\beta_n^2 k}\left(e^{(\beta_n^2/R^2)kx_2} - e^{(\beta_n^2/R^2)kx_1}\right)\Bigg\} \\
&+ \cdots \\
&+ c_k \Bigg\{ \frac{R^2}{\beta_n^2 k}\left(x e^{(\beta_n^2/R^2)kx} - x_{k-1} e^{(\beta_n^2/R^2)kx_{k-1}}\right) \\
&- \left(\frac{R^2}{\beta_n^2 k}\right)^2 \left(e^{(\beta_n^2/R^2)kx} - e^{(\beta_n^2/R^2)kx_{k-1}}\right) \\
&- \frac{x_{k-1} R^2}{\beta_n^2 k}\left(e^{(\beta_n^2/R^2)kx} - e^{(\beta_n^2/R^2)kx_{k-1}}\right)\Bigg\}, \quad x_{k-1} \le x \le x_k.
\end{aligned}
\tag{2.11}
$$

Thus,

$$
\int_0^x e^{(\beta_n^2/R^2)k\lambda}\phi(\lambda)d\lambda = P_n + \sum_{i=1}^{k} c_i R_{\text{in}}, \quad x_{k-1} \le x \le x_k, \tag{2.12}
$$

where P_n and R_{in} can be evaluated by comparison.

We can now rewrite (2.8) as

$$
T(r,x) - T_0 = \frac{2Ak}{R^2}\sum_{n=1}^{\infty} \beta_n e^{-(\beta_n^2/R^2)kx} \frac{J_0\left((r/R)\beta_n\right)}{\left(\beta_n^2 + A^2\right)J_0(\beta_n)}\left(P_n + \sum_{i=1}^{k} c_i R_{\text{in}}\right), \quad x_{k-1} \le x \le x_k. \tag{2.13}
$$

In order to estimate the value of N such that

$$
\begin{aligned}
&\frac{2Ak}{R^2}\sum_{n=1}^{N} \beta_n e^{-(\beta_n^2/R^2)kx} \frac{J_0\left((r/R)\beta_n\right)}{\left(\beta_n^2 + A^2\right)J_0(\beta_n)}\left(P_n + \sum_{i=1}^{k} c_i R_{\text{in}}\right) \\
&\quad \approx \frac{2Ak}{R^2}\sum_{n=1}^{\infty} \beta_n e^{-(\beta_n^2/R^2)kx} \frac{J_0\left((r/R)\beta_n\right)}{\left(\beta_n^2 + A^2\right)J_0(\beta_n)}\left(P_n + \sum_{i=1}^{k} c_i R_{\text{in}}\right)
\end{aligned}
\tag{2.14}
$$

to any predefined accuracy, let us analyse first the infinite series

$$
\frac{2Ak}{R^2}\sum_{n=1}^{\infty} \beta_n e^{-(\beta_n^2/R^2)kx} \frac{J_0\left((r/R)\beta_n\right)}{\left(\beta_n^2 + A^2\right)J_0(\beta_n)} P_n, \tag{2.15}
$$

where

$$P_n = \frac{T_0 R^2}{k\beta_n^2}\left\{e^{(\beta_n^2/R^2)kx} - 1\right\},$$

$$\begin{aligned}&\frac{2Ak}{R^2}\sum_{n=1}^{\infty}\beta_n e^{-(\beta_n^2/R^2)kx}\frac{J_0\left((r/R)\beta_n\right)}{\left(\beta_n^2 + A^2\right)J_0(\beta_n)}\left[\frac{T_0R^2}{k\beta_n^2}\left\{e^{(\beta_n^2/R^2)kx} - 1\right\}\right] \\ &= 2AT_0\left\{\sum_{n=1}^{\infty}\frac{1}{\beta_n}\frac{J_0\left((r/R)\beta_n\right)}{\left(\beta_n^2 + A^2\right)J_0(\beta_n)} + \sum_{n=1}^{\infty}\frac{e^{-(\beta_n^2/R^2)kx}}{\beta_n}\frac{J_0\left((r/R)\beta_n\right)}{\left(\beta_n^2 + A^2\right)J_0(\beta_n)}\right\}.\end{aligned} \tag{2.16}$$

Let us consider the first series in (2.16).

Since $\beta_n > \beta_1 + 3(n-1)$,

$$\begin{aligned}\sum_{n=N+1}^{\infty}\frac{1}{\beta_n}\frac{J_0\left((r/R)\beta_n\right)}{\left(\beta_n^2 + A^2\right)J_0(\beta_n)} &< \sum_{n=N+1}^{\infty}\frac{1}{\beta_1 + 3(n-1)}\frac{J_0\left((r/R)\beta_n\right)}{\left(\beta_n^2 + A^2\right)J_0(\beta_n)} \\ &< \frac{1}{\beta_1 + 3N}\sum_{n=N+1}^{\infty}\frac{J_0\left((r/R)\beta_n\right)}{\left(\beta_n^2 + A^2\right)J_0(\beta_n)}.\end{aligned} \tag{2.17}$$

Setting $x = 0$ in (2.8), we can verify that for all r/R,

$$\sum_{n=1}^{\infty}\frac{J_0\left((r/R)\beta_n\right)}{\left(\beta_n^2 + A^2\right)J_0(\beta_n)} = \frac{1}{2A}. \tag{2.18}$$

Consequently,

$$\sum_{n=N+1}^{\infty}\frac{J_0\left((r/R)\beta_n\right)}{\left(\beta_n^2 + A^2\right)J_0(\beta_n)} = \frac{1}{2A} - \sum_{n=1}^{N}\frac{J_0\left((r/R)\beta_n\right)}{\left(\beta_n^2 + A^2\right)J_0(\beta_n)}. \tag{2.19}$$

Thus, for any N, we can verify whether

$$\sum_{n=N+1}^{\infty}\frac{1}{\beta_n}\frac{J_0\left((r/R)\beta_n\right)}{\left(\beta_n^2 + A^2\right)J_0(\beta_n)} < \frac{1}{\beta_1 + 3N}\left[\frac{1}{2A} - \sum_{n=1}^{N}\frac{J_0\left((r/R)\beta_n\right)}{\left(\beta_n^2 + A^2\right)J_0(\beta_n)}\right] < \varepsilon, \tag{2.20}$$

where ε is any predetermined accuracy.

The same truncation index N can be used to estimate a sufficient number of terms in the second series.

Indeed, let us rewrite

$$\begin{aligned}&\frac{2Ak}{R^2}\sum_{n=1}^{\infty}\beta_n e^{-(\beta_n^2/R^2)kx}\frac{J_0\left((r/R)\beta_n\right)}{\left(\beta_n^2 + A^2\right)J_0(\beta_n)}\left[\frac{T_0R^2}{k\beta_n^2}\left\{e^{(\beta_n^2/R^2)kx} - 1\right\}\right] \\ &\quad = 2AT_0\left\{\sum_{n=1}^{\infty}a_n + \sum_{n=1}^{\infty}a_n e^{-(\beta_n^2/R^2)kx}\right\},\end{aligned} \tag{2.21}$$

and let N be the index such that

$$\frac{\sum_{n=N+1}^{\infty} a_n}{\sum_{n=1}^{N} a_n} \leq \varepsilon. \tag{2.22}$$

Since

$$\begin{aligned}
\sum_{n=1}^{N} a_n e^{-(\beta_n^2/R^2)kx} &> e^{-(\beta_N^2/R^2)kx} \sum_{n=1}^{N} a_n, \\
\sum_{n=N+1}^{\infty} a_n e^{-(\beta_n^2/R^2)kx} &< e^{-(\beta_N^2/R^2)kx} \sum_{n=N+1}^{\infty} a_n, \\
\frac{\sum_{n=N+1}^{\infty} a_n e^{-(\beta_n^2/R^2)kx}}{\sum_{n=1}^{N} a_n e^{-(\beta_n^2/R^2)kx}} &< \frac{e^{-(\beta_N^2/R^2)kx} \sum_{n=N+1}^{\infty} a_n}{e^{-(\beta_N^2/R^2)kx} \sum_{n=1}^{N} a_n} < \varepsilon,
\end{aligned} \tag{2.23}$$

consequently N is a conservative estimate also for the second series.

It can be shown that using a similar procedure, the same truncation index can be used also for the series

$$\sum_{n=1}^{\infty} c_i R_{\text{in}} \beta_n e^{-(\beta_n^2/R^2)kx} \frac{J_0\left((r/R)\beta_n\right)}{\left(\beta_n^2 + A^2\right) J_0(\beta_n)}. \tag{2.24}$$

All the previous algebraic expressions can be combined to provide the final relationship between the radial distribution of temperatures in a section of the pipe at a distance L from the point where heat transfer with the soil starts

$$\begin{aligned}
T(r, L) &= T_0 + \omega(r) + \sum_{i=1}^{M} c_i \xi_i(r), \\
\omega(r) &= \frac{2Ak}{R^2} \sum_{n=1}^{N} \beta_n P_n(L) e^{-(\beta_n^2/R^2)kL} \frac{J_0\left((r/R)\beta_n\right)}{\left(\beta_n^2 + A^2\right) J_0(\beta_n)}, \\
\xi_i(r) &= \frac{2Ak}{R^2} \sum_{n=1}^{N} \beta_n R_{\text{in}}(L) e^{-(\beta_n^2/R^2)kL} \frac{J_0\left((r/R)\beta_n\right)}{\left(\beta_n^2 + A^2\right) J_0(\beta_n)}.
\end{aligned} \tag{2.25}$$

For each r, the value of N is determined by the condition

$$\frac{1}{\beta_1 + 3N} \left[\frac{1}{2A} - \sum_{n=1}^{N} \frac{J_0\left((r/R)\beta_n\right)}{\left(\beta_n^2 + A^2\right) J_0(\beta_n)} \right] \approx \varepsilon \sum_{n=1}^{N} \frac{1}{\beta_n} \frac{J_0\left((r/R)\beta_n\right)}{\left(\beta_n^2 + A^2\right) J_0(\beta_n)}, \tag{2.26}$$

where ε is typically 10^{-6}.

For any data set,

$$y_j = T(r_j, L) - T_0 - \omega(r_j), \tag{2.27}$$

we can estimate the slopes of the piecewise linear temperature distribution of the soil from the system of linear equations

$$y_j = \sum_{i=1}^{M} \xi_{ij} c_i. \tag{2.28}$$

The usual least-squares estimation procedure provides the well-known relationship

$$\hat{\mathbf{c}} = (\Gamma^*\Gamma)^{-1}\Gamma^*\mathbf{y}, \tag{2.29}$$

where $\hat{\mathbf{c}}$ is the vector of the estimated slopes and $\Gamma = \|\xi_{ij}\|$.

Since this estimation problem is an ill-posed problem, the accuracy of the estimates $\hat{c}$ does not depend continuously on the experimental errors on the data.

The results obtained applying Tikhonov's regularisation method to this problem will be discussed in the next sections using simulated data generated by a smooth temperature profile with a spike representing a hot spot in the landfill.

3. Regularisation Technique

Reducing the unknown soil temperature function to a finite-dimensional vector $\hat{c}$ changes the theoretically ill-posed problem into a numerically ill-conditioned one, reflected by near singularity of the matrix $\Gamma^*\Gamma$.

Thus, the most frequently used regularisation method consists in the modification and/or elimination of the eigenvalues of $\Gamma^*\Gamma$ that are too small.

A possible way to do this is reducing the dimension of the matrix (which in our case implies reducing the number of intervals over which the temperature of the soil is approximately linear). For this approach to be effective, the dimension of the vector $\hat{\mathbf{c}}$ has frequently to be reduced so severely as to result in an unacceptably poor reconstruction.

A more efficient technique is the one proposed by Tikhonov and Arsenine [5] and based on the statistical properties of the experimental errors on the set of measured variables $\mathbf{y}$.

To illustrate it, let us suppose that measured $\mathbf{y}'$ and exact (unknown) values $\mathbf{y}$ of the experimental data are related by the relationship

$$\left\|\mathbf{y} - \mathbf{y}'\right\|^2 \leq \delta, \tag{3.1}$$

where δ is determined by the variance of the statistical distribution of the experimental error.

Tikhonov's regularisation method consists in replacing the original minimisation problem

$$\left\|\Gamma\hat{\mathbf{c}} - \mathbf{y}'\right\|^2 = \min, \tag{3.2}$$

Table 1

Parameter	Value	Symbol
Fluid speed	1 m/s	u
Pipe diameter	0.4 m	$2R$
Fluid density	1000 Kg/m^3	ρ
Fluid conductivity	0.6397 W/(s m °K)	K
Heat transfer coefficient*	90.36 J/(s m^2 °K)	H

* Data taken from [11] ("Ground Source Heat Pumps: Design of Geothermal Systems for Commercial and Institutional Buildings"), ASHRAE (2008).

with the minimisation problem

$$\left\| \Gamma \hat{\mathbf{c}} - \mathbf{y}' \right\|^2 + \alpha \|\hat{\mathbf{c}}\|^2 = \min, \tag{3.3}$$

where the positive constant α is chosen so that

$$\left\| \Gamma \hat{\mathbf{c}} - \mathbf{y}' \right\|^2 = \delta. \tag{3.4}$$

Combining (3.3) and (3.4) provides the reconstructed vector $\hat{\mathbf{c}}$,

$$\hat{\mathbf{c}} = (\Gamma^* \Gamma + \alpha \mathbf{I})^{-1} \Gamma^* \mathbf{y}', \tag{3.5}$$

with α being determined by Morozov's discrepancy method [10], that is, iteratively increasing the value of α until (3.4) is satisfied.

Clearly the eigenvalues of $\Gamma^*\Gamma$ are now increased by an amount α, which being positive regularises the solution vector $\hat{\mathbf{c}}$ at the price of smoothing it. The compromise between regularisation and accuracy is given by (3.4), which being rooted in statistics provides a theoretical framework for an optimal offset.

However, caution is warranted when considering automatic acceptance of the solution obtained. Indeed, the value of δ (related to the statistical distribution of the experimental error) might be only approximately known. Additionally, the variance of the sample can differ substantially from the theoretical one, thus leading to a biased value of δ.

Therefore, solution vectors $\hat{\mathbf{c}}$ obtained by letting α vary around the optimal Tikhonov's value (typically an order of magnitude above and below) should be examined for the detection of possible over- or undersmoothing effects.

4. A Numerical Example

Exact simulated data have been generated using a smooth parabolic temperature profile with a spike to indicate the presence of a hot spot which might turn into a landfill fire. The profile of the physical model is plotted in Figure 1. The geometrical and physical-chemical parameters used are reported in Table 1.

Since the fluid used is water, both fluid density and fluid conductivity can be estimated with a very high degree of accuracy. Consequently the first four parameters can be assumed to

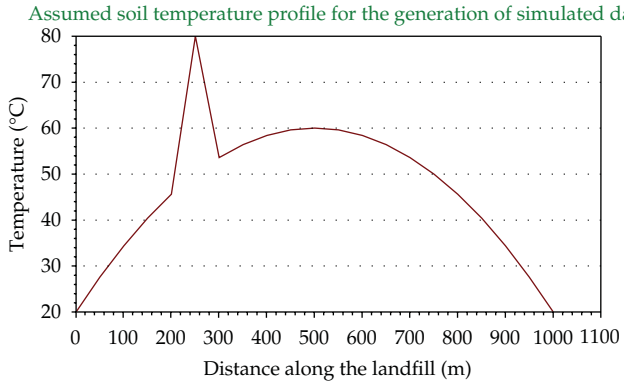

Figure 1

be accurately known. On the other hand, the heat transfer coefficient depends on the nature of soil. Since the goal of this paper is to show the reliability of the general procedure, the literature value (recommended by the American Society of Heating and Air-Conditioning for ordinary soil) has been used.

More accurate values (based on an experimental campaign) should be employed when real life cases are considered. Additionally, the uncertainties resulting from the standard deviation of the estimate of the heat transfer coefficient should be taken into account. To this purpose, a preliminary parameter sensitivity analysis is carried out in this paper by letting the parameter H vary by 10% about the value recommended by the ASHRAE.

The computation of data was carried out using (2.8). The truncation index was evaluated using the procedure described previously, whereas the integrals were computed analytically.

A Gaussian distributed error with zero mean and a standard deviation equal to the measurement precision (10^{-3}°C) was added to the exact simulated data.

The soil temperature profile was reconstructed using 10, 12, 15, and 20 equally spaced intervals in each of which the temperature profile was assumed linear. The regularisation parameter was estimated using Tikhonov's stabilisation method based on the statistical assumptions.

The corresponding graphs are plotted in Figures 2, 3, 4, and 5, respectively.

In all reconstructions, there is no clear identification of a peak, rather a smooth "bump" appears in all reconstructions at approximately the right place. Thus, the number of intervals does not seem to significantly affect the reconstruction of the temperature profile.

On the other hand, if Tikhonov's parameter is reduced by a factor 2, the presence of a temperature peak at the right position is more clearly visible. The value of the peak is also estimated with good accuracy as shown in the 15-interval reconstruction plotted in Figure 6.

The increased accuracy in position and intensity of the peak value is offset by more marked oscillations, as could be expected owing to the reduction of the smoothing factor.

As expected, increasing Tikhonov's parameter by a factor 2 smooths the temperature profile further and blurs the shape of the peak, as shown in Figure 7.

In all reconstructions, there is a hint that a hot spot with a larger-than-expected temperature is present in the landfill. The position is also predicted with reasonable accuracy. Reducing the value of Tikhonov's parameter below its theoretically optimal value provides an excellent estimation of position and intensity of the temperature peak. Thus, combining

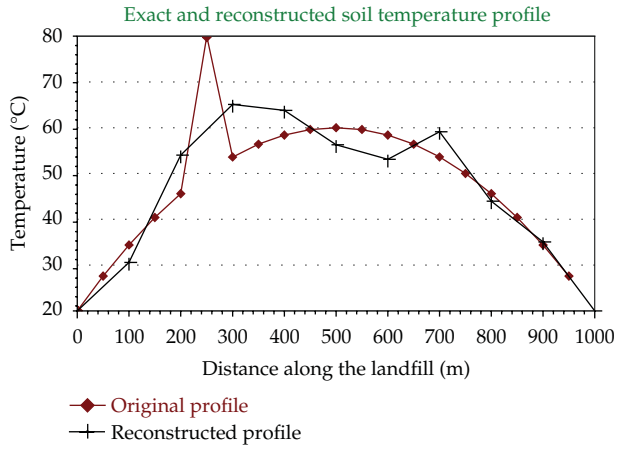

Figure 2: Ten intervals—Tikhonov's regularisation factor.

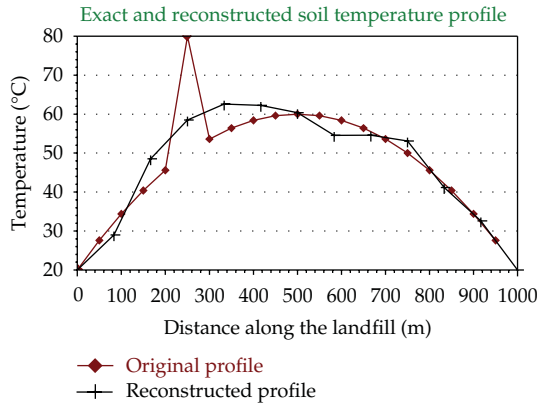

Figure 3: Twelve intervals—Tikhonov's regularisation factor.

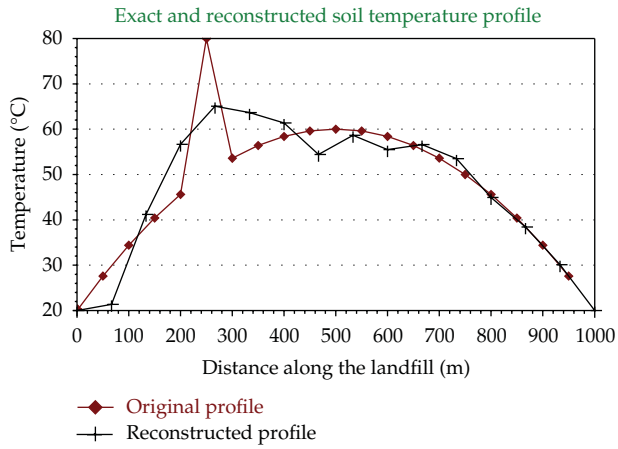

Figure 4: Fifteen intervals—Tikhonov's regularisation factor.

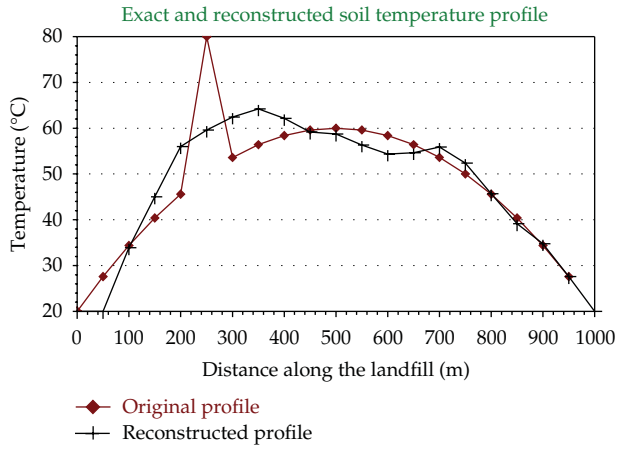

Figure 5: Twenty intervals—Tikhonov's regularisation factor.

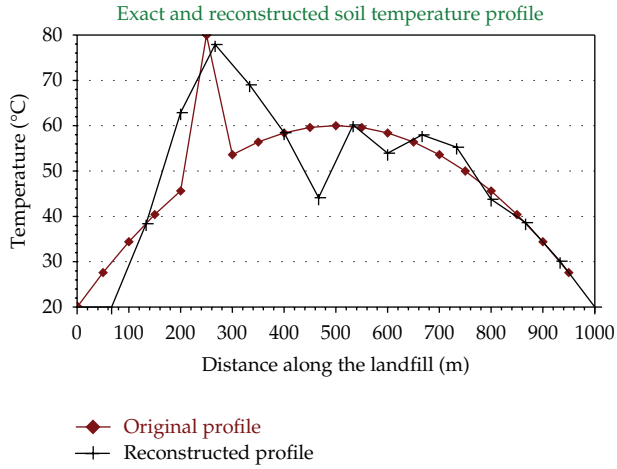

Figure 6: Fifteen intervals—Half Tikhonov's regularisation factor.

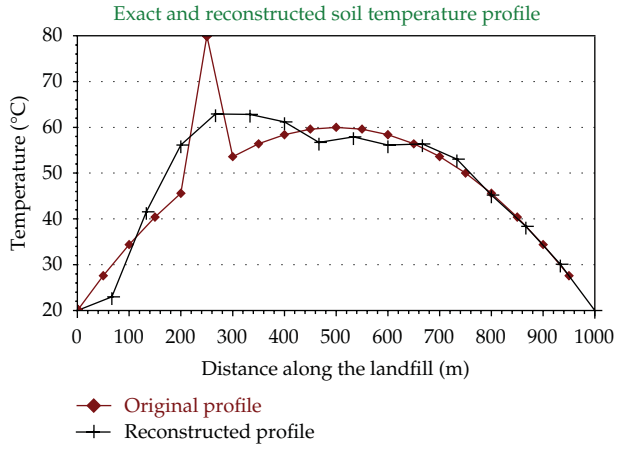

Figure 7: Fifteen intervals—double Tikhonov's regularisation factor.

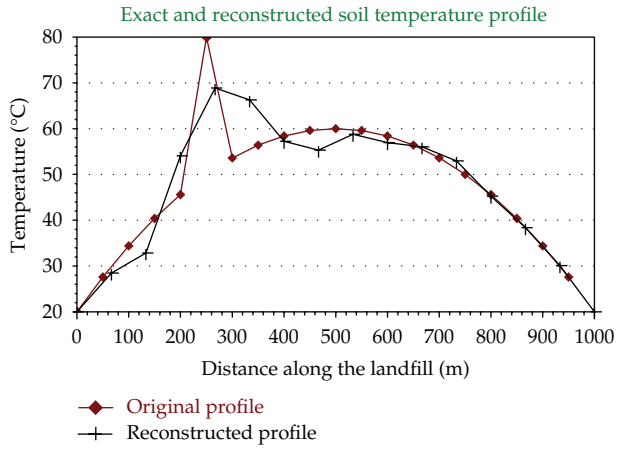

Figure 8: Fifteen intervals—Tikhonov's regularisation factor-assumed heat transfer coefficient equal to 90% of the value used to generate the simulated data.

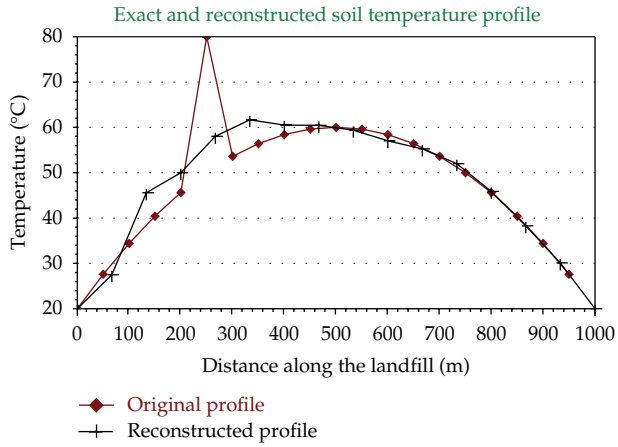

Figure 9: Fifteen intervals—Tikhonov's regularisation factor-assumed heat transfer coefficient equal to 110% of the value used to generate the simulated data.

Tikhonov's regularisation method with a strategy of exploring additional reconstructions by letting the regularisation parameter vary around its theoretical value provides valuable information for the overall monitoring process.

As mentioned before, the only parameter subject to a certain degree of uncertainty is the heat transfer coefficient. Even if good estimates can be obtained through a limited number of measurements in a well-designed experimental campaign, it is important to verify the consequences of the use of an incorrect heat transfer coefficient on the reconstruction of the temperature profile.

To this purpose, a simple sensitivity analysis has been performed by examining reconstructed profiles when the heat transfer coefficient employed in the regression analysis differs by 10% from the corresponding value used in the generation of the simulated data.

The heat transfer coefficient H is directly proportional to the variable A. Furthermore, it follows from the relation $\beta J_1(\beta) = AJ_0(\beta)$ that the variables β_n are increasing functions of A.

Thus, both ω and ξ (and consequently the vector y' and the matrix Γ) are decreasing functions of the heat transfer coefficient used in the reconstruction. Therefore a higher value of H is equivalent to an increased weight of the regularisation term in the minimisation problem (3.3) and consequently to a more marked smoothing effect.

This is confirmed by the two further reconstructions obtained using 15 equally spaced intervals, the theoretical Tikhonov's regularisation factor, and values of the heat transfer coefficient equal to 90% and 110% of the original value, respectively. As shown in Figures 8 and 9, even a 10% deviation from the true value (which can be regarded as an upper estimate error) does not affect to any significant degree the analysis made.

Furthermore, it can prove difficult to distinguish between over- (under)smoothing due to larger- (smaller-) than-optimal value of Tikhonov's factor and a wrong estimate of the heat transfer coefficient. This can be regarded as an added reason for considering a reasonably wide range of values of this factor.

5. Conclusions

If and when the heat generated in a landfill is extracted by the circulation of a heat recovery fluid, some additional information on temperature distribution inside the landfill will be available as an added benefit.

The reconstruction technique described in this paper is not intended to replace the traditional monitoring, but rather to complement it, making it possible to reduce the number of sensors and/or to detect potential combustion phenomena at places where no sensor is installed. Furthermore, mobile temperature monitoring equipment can be more efficiently allocated following the indications provided by the implementation of the algorithm developed in this paper.

Notation

Symbols

c_i: Slope of temperature in the interval i (°C/m)
c_p: Specific heat of heat recovery fluid
h: Interval of linear dependance of temperature on distance (m)
H: Soil heat transfer coefficient (J/(s·m^2 · °K))
J_0: Bessel function of order zero
J_1: Bessel function of order one
K: Heat conduction coefficient of heat recovery fluid (W/(s ·m ·°C))
L: Distance travelled by the fluid in the landfill (m)
M: Number of equally spaced intervals in L
N: Number of terms in the infinite series necessary to achieve a relative accuracy ε
u: Speed of heat recovery fluid (m/s)
r: Radial variable in the pipe cross section (m)
R: Pipe radius (m)
T: Temperature (°C)
T_0: Ambient temperature (°C)
x: Variable in the direction of fluid motion (m)
y: Experimental data set

α: Tikhonov's regularisation parameter
ε: Relative accuracy in the evaluation of series
λ: Dummy integration variable
ρ: Density of heat recovery fluid (Kg/m^3)
φ: Unknown exact soil temperature profile (°C).

Symbols Defined by Equations

A: $R \cdot H$
k: $K/(\rho \cdot c_p \cdot u)$
P_n, R_{in}: Defined by the equation $\int_0^L e^{(\beta_n^2/R^2)k\lambda}\varphi(\lambda)d\lambda = P_n + \sum_{i=1}^{M} c_i R_{\text{in}}$
β_n: nth root of the equation $\beta J_1(\beta) = AJ_0(\beta)$
Γ: Matrix whose elements are ξ_{ij}
δ: Parameter determined by the variance of the statistical distribution of the experimental error
$\xi,\ \omega$: Defined by the equation $T(r, L) = T_0 + \omega(r) + \sum_{i=1}^{M} c_i\xi_i(r)$.

Superscripts

$'$: Experimental value
$\hat{}$: Estimated value.

References

[1] D. R. Reinhart, P. T. McCreanor, and T. G. Townsend, "The bioreactor landfill: its status and future," *Waste Management and Research*, vol. 20, no. 2, pp. 172–86, 2002.
[2] S. Renou, J. G. Givaudan, S. Poulain, F. Dirassouyan, and P. Moulin, "Landfill leachate treatment: review and opportunity," *Journal of Hazardous Materials*, vol. 150, no. 3, pp. 468–493, 2008.
[3] M. Zamorano, J. I. Pérez Pérez, I. Aguilar Pavés, and A. Ramos Ridao, "Study of the energy potential of the biogas produced by an urban waste landfill in Southern Spain," *Renewable and Sustainable Energy Reviews*, vol. 11, no. 5, pp. 909–922, 2007.
[4] N. J. Themelis and P. A. Ulloa, "Methane generation in landfill," *Renewable Energy*, vol. 32, pp. 1243–1257, 2007.
[5] A. Tikhonov and V. Arsenine, *Méthodes de Résolution de Problémes mal Posés*, Editions MIR, Moscow, Russia, 1976, Traduit du russe par Vladimir Kotliar.
[6] V. G. Dovi', A. P. Reverberi, and V. P. Meshalkin, "A general procedure for the estimation of diffusivities in solids," *The Canadian Journal of Chemical Engineering*, vol. 72, no. 6, pp. 1042–1046, 1994.
[7] R. B. Bird, W. E. Stewart, and E. N. Lightfoot, *Transport Phenomena*, John Wiley & Sons, New York, NY, USA, 2002.
[8] H. S. Carslaw and J. C. Jaeger, *Conduction of Heat in Solids*, Clarendon Press, Oxford, UK, 2nd edition, 1959.
[9] R. Courant and D. Hilbert, *Methods of Mathematical physics*, Wiley-VCH, Berlin, Germany, 1989.
[10] V. A. Morozov, *Methods for Solving Incorrectly Posed Problems*, Springer, New York, NY, USA, 1984.
[11] ASHRAE, *Ground Source Heat Pumps: Design of Geothermal Systems for Commercial and Institutional Buildings*, American Society of Heating, Refrigeration and Air Conditioning Engineers, Atlanta, Ga, USA, 2008.

Hindawi Publishing Corporation
Journal of Applied Mathematics
Volume 2012, Article ID 847864, 16 pages
doi:10.1155/2012/847864

Research Article

Study on the Dependence of Reverse Simulation for Identifying a Pollutant Source on Grid Resolution and Filter Width in Cavity Flow

Satoshi Abe,[1] Shinsuke Kato,[2] Fujihiro Hamba,[2] and Daisuke Kitazawa[2]

[1] *Graduate School of Engineering, The University of Tokyo, Tokyo 113-8656, Japan*
[2] *Institute of Industrial Science, The University of Tokyo, Tokyo 153-8505, Japan*

Correspondence should be addressed to Satoshi Abe, abe.satoshi@jaea.go.jp

Received 16 December 2011; Revised 2 March 2012; Accepted 3 March 2012

Academic Editor: Fu-Yun Zhao

When a hazardous substance is diffused, it is necessary to identify the pollutant source and respond immediately. However, there are many cases in which damage is caused without a clear understanding of where the pollutant source is located. There are three groups of identifying pollutant source information (Liu and Zhai, 2007): the probability method, forward method, and backward method. In our previous study, we proposed reverse simulation, which is categorized as a backward method (Abe and Kato, 2011). Numerical instability by negative diffusion is a principal problem in the backward method. In order to improve the problem, we applied a low-pass filter operation to the concentration flux in the RANS analysis. The simulation secured the numerical stability. However, reverse simulation accuracy is expected to depend on the grid resolution and filter width. In this paper, we introduce reverse simulation results in cavity flow. In particular, we survey the dependence of reverse simulation accuracy on the grid resolution and filter width. Moreover, we discuss the dependence of reverse simulation on the grid resolution and filter width with a one-dimensional diffusion equation. As a result, we found that the simulated negative diffusion varies greatly among the grid resolution and filter width.

1. Introduction

When a hazardous substance is diffused, it is necessary to identify the source of the pollutant and respond immediately, for example, by cleaning up and evacuating people from the area. However, there are many cases in which damage is caused without a clear understanding of where the pollutant source is located. Many lives have been lost as a result of accidental pollution from power stations and factories (e.g., Chernobyl in 1986, Bopal in 1984).

In recent years, some researchers have studied techniques of identifying pollutant sources either in the groundwater or air. The techniques are separated into three groups: probability method, forward method, and backward method [1].

Probability methods determine the pollutant source information with probability objective functions. Wagner developed nonlinear maximum likelihood estimation for simultaneous model parameter estimation and source characterization [2]. The method combines groundwater flow and contaminant transport simulation. Woodbury et al. applied minimum relative entropy theory in order to recover the release history in groundwater flow [3]. Neupauer et al. developed an adjoint method as a formal framework for predicting groundwater contaminant source location and travel-time probabilities [4]. Sohn et al. worked on rapidly locating and characterizing air pollutant releases and presented an approach for estimating the source locations, the amounts released, and the dispersion characteristics of indoor airborne pollutants [5]. They proposed a two-stage Bayesian data interpretation approach.

The forward method identifies the pollutant source by trial-and-error algorithm. The processes describe the match degree of measured and simulated results and can be used to estimate the pollutant sources. Gorelick et al. applied minimizing normalized residual for identifying the source and magnitude of groundwater pollutants in some two-dimensional cases [6]. Alapati and Kabala applied the least squares function to predict the source release history in a one-dimensional underground water problem [7]. In the forward method, there are ways of applying the Tikhonov regularization method [8], which is the most commonly employed method for an ill-posed problem. Skaggs and Kabala applied the regularization method to recover the release history in one-dimensional simulation [9]. In atmospheric gaseous dispersion, Seibert et al. used the Tikhonov regularization method [10], which is the most useful method for an ill-posed problem to derive the source history from ambient concentration measurement. These forward methods are good tools for identifying source information. However, every forward method requires many calculations.

The backward method is the solution to the transport equation in negative time with the end status as the input condition. The most important problem in the backward method is the numerical instability from negative diffusion. Generically, CFD needs to define the location with a finite grid resolution, and there are high wave numbers that cannot be resolved in CFD. Here, wave number is expressed as "$k = 2\pi/\lambda$," where λ is the wave length. The high wave number region has rounding error. Meanwhile, the numerical solution converges on a large space gradient when analyzing negative diffusion on CFD. This means that the high wave number component amplifies more quickly than that of the resolved low wave number region. Therefore, the numerical simulation breaks down due to the rounding errors in the high wave number region [11].

The most useful method for improving numerical instability in backward method is the quasi-reversible (QR) solution, which is developed by Skaggs and Kabala [12]. The QR method adds a term to the diffusion term to improve the numerical stability. Equation (1.1) shows the one-dimensional government equation in the QR method

$$\frac{\partial C}{\partial t} = \Gamma \frac{\partial^2 C}{\partial x^2} + \varepsilon \frac{\partial^4 C}{\partial x^4}, \tag{1.1}$$

Γ represents the diffusion coefficient, and ε represents the stabilization coefficient. This equation can solve with a negative time step. In Skaggs and Kabala's research, the method

was used to recover the time history and spatial distribution of a groundwater contaminant plume.

In our previous study, we introduced reverse simulation [13, 14], which was categorized as a backward method. The method applies a lowpass filter operation to improve the numerical stability (1.2)

$$\overline{F}(x) = \int_{-\infty}^{\infty} G(r)F(x-r)dr,$$
$$G(r) = \sqrt{\frac{6}{\pi\Delta^2}} \exp \frac{-6r^2}{\Delta^2}, \tag{1.2}$$

F is a physical quantity that is applied in the filter operation. The filtered physical quantity is shown with an overbar, and Δ is the filter width.

The most important problem when carrying out a transport equation with negative time advancing in CFD is the numerical instability by analyzing negative diffusion. We made a pass at applying the filter operation to a concentration field (1.3) in Reynolds averaged numerical simulation (RANS) analysis [13]

$$F(x) = C(x), \tag{1.3}$$

C means the concentration. This method improved the numerical stability, but there was a big problem with the analysis results. The concentration distribution spread diffusely in an analytical domain. This means that it is difficult to identify a pollutant source with reverse simulation applying a filter operation to a concentration field. Therefore, we developed a reverse simulation. We made a pass at applying the filter operation to a concentration flux (1.5) to improve the numerical stability and solve the above problem [14]

$$F_i(x) = -\langle u_i' c' \rangle = \frac{\nu_t}{\sigma_3} \frac{\partial C(x)}{\partial x_i}, \tag{1.4}$$

$$F_i(x) = \frac{\partial C(x)}{\partial x_i}. \tag{1.5}$$

In (1.3), $-\langle u_i' c' \rangle$ is turbulent concentration flux. Equation (1.4) means gradient diffusion approximation, ν_t is the coefficient of turbulent diffusion, and σ_3 is the turbulent Schmidt number. In RANS analysis, it was necessary to apply the filter operation to (1.4) strictly. However, ν_t is dependent on the position. This makes the filter operation cumbersome and complicated. Therefore, we applied the filter operation to the differential part of only (1.5) approximately. The simulation secured the numerical stability and solved the problem of concentration spreading diffusely. However, the reverse simulation accuracy is expected to depend on the grid resolution and filter width.

In this paper, we survey the dependence of reverse simulation accuracy on the grid resolution and filter width in cavity flow, which forms a greatly bent and circulating flow. The analysis can be carried out with three different grid resolutions. Each grid resolution has three different filter widths. A total of 9 cases were analyzed in this study. In addition, we discuss the dependence of reverse simulation on gird resolution and filter width with a one-dimensional diffusion equation.

2. Analysis Method

2.1. RANS Government Equation

In the present study, the equations formed to govern incompressible flow in RANS analysis were mass conservation flow equation (2.1), the Navier-Stokes equation (2.2), turbulent kinetic energy (K) equation (2.3), turbulent dissipation (ε) equation (2.4), and concentration (C) transport equation (2.5). The concentration is passive scalar, assuming that the flow field has no influence. The turbulence model in this paper is a two-equation Kato-Launder-type model [15]

$$\frac{\partial U_i}{\partial x_i} = 0, \tag{2.1}$$

$$\frac{\partial U_i}{\partial t} + U_j \frac{\partial U_i}{\partial x_j} = -\frac{1}{\rho}\frac{\partial}{\partial x_i}\left(P + \frac{2}{3}K\right) + \frac{\partial}{\partial x_j}\left\{\nu_t\left(\frac{\partial U_i}{\partial x_j} + \frac{\partial U_j}{\partial x_i}\right)\right\}, \tag{2.2}$$

$$\frac{\partial K}{\partial t} + U_i \frac{\partial K}{\partial x_i} = \frac{\partial}{\partial x_i}\left(\frac{\nu_t}{\sigma_1}\frac{\partial K}{\partial x_i}\right) + P_K - \varepsilon, \tag{2.3}$$

$$\frac{\partial \varepsilon}{\partial t} + U_i \frac{\partial \varepsilon}{\partial x_i} = \frac{\partial}{\partial x_i}\left(\frac{\nu_t}{\sigma_2}\frac{\partial \varepsilon}{\partial x_i}\right) + \frac{\varepsilon}{K}C_1 P_k - C_2\frac{\varepsilon^2}{K}, \tag{2.4}$$

$$\frac{\partial C}{\partial t} + U_i \frac{\partial C}{\partial x_i} = \frac{\partial}{\partial x_i}\left(\frac{\nu_t}{\sigma_3}\frac{\partial C}{\partial x_i}\right), \tag{2.5}$$

$$\nu_t = C_\mu \frac{K^2}{\varepsilon},$$

$$P_k = \nu_t S\Omega,$$

$$S = \sqrt{\frac{1}{2}\left(\frac{\partial U_i}{\partial x_j} + \frac{\partial U_j}{\partial x_i}\right)^2}, \tag{2.6}$$

$$\Omega = \sqrt{\frac{1}{2}\left(\frac{\partial U_i}{\partial x_j} + \frac{\partial U_j}{\partial x_i}\right)^2},$$

$$\sigma_1 = 1.0, \quad \sigma_2 = 1.3, \quad \sigma_3 = 1.0, \quad C_\mu = 0.09, \quad C_1 = 1.44, \quad C_2 = 1.92.$$

The process of negative time advancing in the transport equation is equivalent to that of positive time advancing with negative time convection and diffusion (2.7)

$$\frac{\partial C}{\partial t} - U_i \frac{\partial C}{\partial x_i} = -\frac{\partial}{\partial x_i}\left(\frac{\nu_t}{\sigma_3}\frac{\partial C}{\partial x_i}\right). \tag{2.7}$$

But the equation is unstable with time advancing. Overall, in forward analysis, the diffusion term has the effect of improving the numerical stability because the diffusion coefficients (ν_t) are a positive value. However, in the backward method, the coefficients are a negative value. A diffusion term that has a negative coefficient increases the intensity of the high wave

number region and destabilizes the numerical simulation. For this, we apply lowpass filter operation to (1.2) the concentration flux (1.5). Equation (2.7) is converted to (2.8) by the filter operation

$$\frac{\partial C}{\partial t} - U_i \frac{\partial C}{\partial x_i} = -\frac{\partial}{\partial x_i}\left(\frac{\nu_t}{\sigma_3}\overline{\frac{\partial C}{\partial x_i}}\right). \tag{2.8}$$

The idea is to simulate the negative diffusion played by the low wave number region and cut that by the high wave number region. The lowpass filter operation to the concentration flux is clearly beneficial in [14].

In the present stage, flow fluctuations are not considered. Essentially, it is good to consider the flow fluctuation because the air flow characteristics are unsteady due to fluctuation in both speed and direction. However, it is necessary for treating the unsteady flow to solve the Navier-Stokes equation (2.2) in negative time (inverse analysis) or keep full-time and space-series data. The former is impossible, because it is necessary to couple the Navier-Stokes equation to the mass conservation equation (2.1). The latter requires huge memory to store the time-series data. In addition, our purpose in this paper is to survey and discuss the dependence of reverse simulation on the grid resolution and filter width. In consideration of these circumstances, we treat the steady flow in the forward and reverse analyses.

2.2. The Numerical Discretization, Simulation Method, and Analysis Model

Regarding a lowpass filter operation for reverse numerical calculations, the Gaussian filter is given the Taylor expansion and discretization

$$\overline{F}(x) = F(x) + \frac{F''(x)}{2}\int_{-\infty}^{\infty} r^2 G(r)dr + \frac{F^{(4)}(x)}{24}\int_{-\infty}^{\infty} r^4 G(r)dr + \cdots, \tag{2.9}$$

$$\overline{F}_m = F_m + \frac{\Delta^2}{24}\frac{F_{m-1} - 2F_m + F_{m+1}}{\Delta x^2}. \tag{2.10}$$

Equation (2.8) is expressed as (2.11) when using (2.10)

$$\frac{\partial C}{\partial t} - U_i \frac{\partial C}{\partial x_i} = -\frac{\partial}{\partial x_i}\frac{\nu_t}{\sigma_3}\left\{\frac{\partial C}{\partial x_i} + \frac{\Delta^2}{24}\frac{\partial^2}{\partial x_i^2}\left(\frac{\partial C}{\partial x_i}\right)\right\}. \tag{2.11}$$

The second term of the right-hand side of (2.11) is able to improve the numerical stability in backward analysis. Table 1 shows a summary of the parameters used in the numerical simulation. For spatial discretization in all governing equations, a second-order accurate central difference scheme is used for the convection terms and diffusion terms. In addition, when the concentration is below 0, it is replaced as 0 (clipping method). For time integration, the convection and diffusion terms in the flow field are discretized using the Adams-Bashforth schemes. Also, the convection and diffusion in the scalar fields (concentration,

Table 1: Numerical simulation parameters.

Turbulent model	Kato-Launder k-åmodel
Navier-Stokes equation	Convection term: 2nd-order central difference scheme Diffusion term: 2nd-order central difference scheme
Scalar transport equation (K, ε, C)	Convection term: 2nd-order central difference scheme Diffusion term: 2nd-order central difference scheme
Time advancing	Convection term: Adams-Bashforth method Diffusion term: Adams-Bashforth method
Algorithm	ABMAC type

Table 2: Numerical grids and filter width in each case.

Analysis case		Analysis condition (numerical grid resolution and filter width)
Case 1	Case 1-1	$\Delta x/H_b = 0.2$, $\Delta y/H_b = 0.2$, $\Delta z/H_b = 0.1$, $\Delta = 10.0\text{Ä}x_i$
	Case 1-2	$\Delta x/H_b = 0.2$, $\Delta y/H_b = 0.2$, $\Delta z/H_b = 0.1$, $\Delta = 15.0\text{Ä}x_i$
	Case 1-3	$\Delta x/H_b = 0.2$, $\Delta y/H_b = 0.2$, $\Delta z/H_b = 0.1$, $\Delta = 20.0\text{Ä}x_i$
Case 2	Case 2-1	$\Delta x/H_b = 0.1$, $\Delta y/H_b = 0.1$, $\Delta z/H_b = 0.05$, $\Delta = 10.0\text{Ä}x_i$
	Case 2-2	$\Delta x/H_b = 0.1$, $\Delta y/H_b = 0.1$, $\Delta z/H_b = 0.05$, $\Delta = 15.0\text{Ä}x_i$
	Case 2-3	$\Delta x/H_b = 0.1$, $\Delta y/H_b = 0.1$, $\Delta z/H_b = 0.05$, $\Delta = 20.0\text{Ä}x_i$
Case 3	Case 3-1	$\Delta x/H_b = 0.05$, $\Delta y/H_b = 0.05$, $\Delta z/H_b = 0.05$, $\Delta = 10.0\text{Ä}x_i$
	Case 3-2	$\Delta x/H_b = 0.05$, $\Delta y/H_b = 0.05$, $\Delta z/H_b = 0.05$, $\Delta = 15.0\text{Ä}x_i$
	Case 3-3	$\Delta x/H_b = 0.05$, $\Delta y/H_b = 0.05$, $\Delta z/H_b = 0.05$, $\Delta = 20.0\text{Ä}x_i$

turbulent kinetic energy and turbulent dissipation fields) are discretized using the Adams-Bashforth schemes. In terms of the Navier-Stokes equation and mass conservation equation, the coupling algorithm of the velocity and pressure is based on the ABMAC type [16].

Regarding the grid number and filter width, Table 2 shows the analysis grid resolutions and filter width in each case. Case 1 is the coarsest grid resolution, and case 3 is the finest grid resolution in all cases. Furthermore, we set three different filter widths in each grid resolution.

The domain size is 2.0 H_b, 2.0 H_b, and 5.0 H_b (streamwise, spanwise, and vertical, resp.). Here, H_b is the cavity height. The cavity size is 1.0 H_b, 2.0 H_b, and 1.0 H_b (Figure 1). The streamwise, spanwise, and vertical directions are $x(x_1), y(x_2)$, and $z(x_3)$, respectively. Regarding the boundary conditions, in these analyses, the periodic boundary condition is imposed on the streamwise direction for velocity field, turbulent kinetic energy, and turbulent dissipation. The Neumann condition is imposed on the top boundary for all physical quantities. The boundary conditions for bottom and walls are given by the generalized log-law for the velocity field and the Neumann conditions for turbulent kinetic energy, turbulent dissipation, and concentration field. In addition, the Neumann conditions are applied to all boundary conditions for the filter operation.

Figure 2 shows the normalized analysis time and the normalized emission time of concentration (tU_b/H_b). The forward and reverse analysis times are, respectively, from 0 to 100 and from 100 to 200, which are normalized by H_b and U_b. U_b is the velocity at H_b. As we developed a method of identifying the pollutant source, it is necessary to identify the elapsed time since emission in addition to the source location. But this time, we assume that the elapsed time is known. The emission time is from 0 to 20. The source point is 0.2 H_b, below the head of the cavity and 0.2 H_b downstream of the upper part of the cavity.

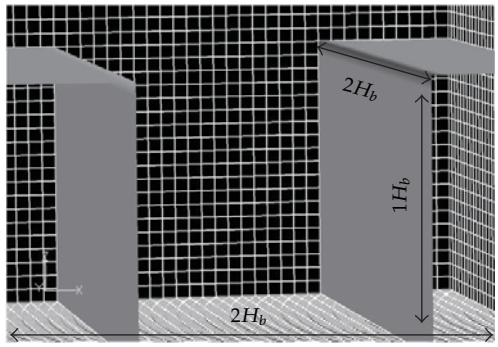

Figure 1: Analysis domain: the domain size of streamwise, span, and vertical directions is 2.0 H_b, 2.0 H_b, and 5.5 H_b, respectively. H_b refers to the cavity height.

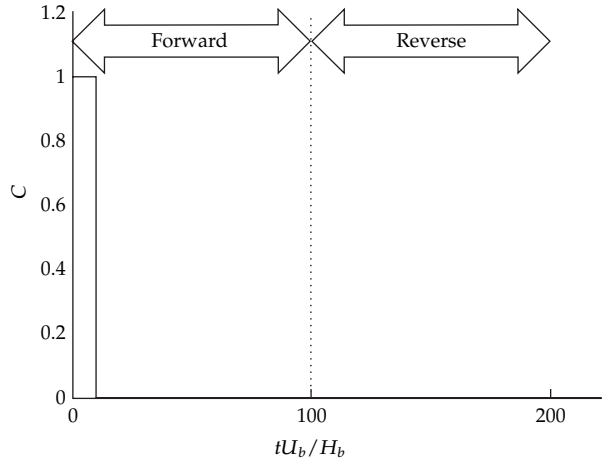

Figure 2: Emission time and analysis time, forward analysis time: 0~100, reverse analysis time: 100~200. U_b refers to the velocity at H_b.

3. Analysis Results

3.1. Forward Analysis Results

Figure 3 shows the vector of the velocity fields in the cavity. In each analysis case, the velocity fields form circulatory flows, and all cases are similar for the stagnation point. All analysis cases have almost the same velocity field.

Figure 4 shows the results of forward analysis ($tU_b/H_b = 100$). The results are to show the input conditions for reverse simulation. These contours are normalized by the peak concentration in each case. In Case 1, the location of peak concentration slightly shifts to the center of the bottom due to a difference of grid resolution. However, the concentration distributions of all cases are similar overall. With the forward analysis results, reverse simulations are carried out.

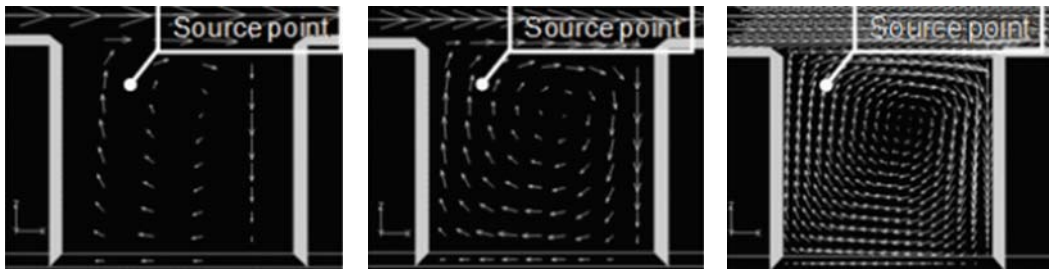

(a) (b) (c)

Figure 3: Side view of velocity vector: (a) Case 1, (b) Case 2, and (c) Case 3.

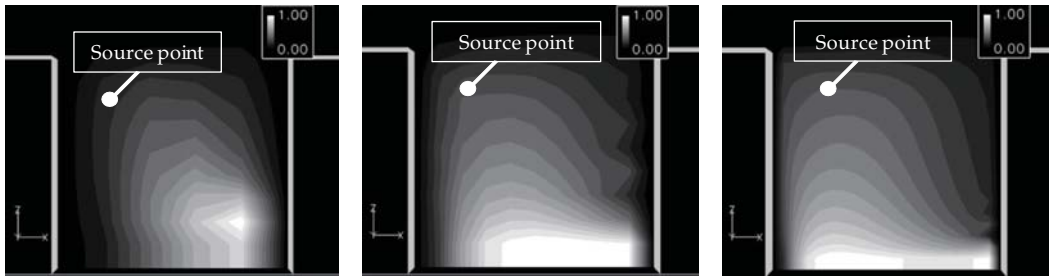

(a) (b) (c)

Figure 4: Input conditions for reverse simulation ($tU_b/H_b = 100$): (a) Case 1, (b) Case 2, and (c) Case 3.

3.2. Reverse Analysis Results

3.2.1. The Influence of Grid Resolution

Figure 5 shows the results of reverse simulations for three different grid resolutions ($tU_b/H_b = 200$). These distributions are normalized by the peak concentrations of each case at $tU_b/H_b = 100$. In each case, numerical instabilities are improved by the filter operation.

However, regarding Case 1-1, which has the coarsest grid resolution (Case 1-1), the concentration distribution spreads widely over the whole cavity. In addition, the high concentration location is very far from the source point as the initial condition of forward analysis because the lowpass filter effect is too strong. In other words, the numerical grid resolution of Case 1 is too rough to carry out reverse simulation and it is difficult to identify a pollutant source when using the grid resolution. Meanwhile, high concentration parts of Case 2-1 and Case 3-1 are clearer than that of Case 1-1. In particular, that of Case 3-1 is the clearest in these analyses.

To identify the pollutant source, we consider the high concentration distributions. Figure 6 shows distributions of over 80 percent of peak concentration in Case 1-1, Case 2-1, and Case 3-1, respectively. These figures are normalized by the peak concentrations in each case at $tU_b/H_b = 100$. The location of Case 1-1 is not appropriate, because the filter effect is too strong. The peak locations of Case 2-1 and Case 3-1 are very near to the source point as the initial condition of the forward analysis, especially the result of Case 3-1. Moreover, the grid resolution is concerned with the peak values. The values of Case 1-1 and Case 2-1 are lower than those at $tU_b/H_b = 100$, and the peak value of Case 3-1 is higher than that at $tU_b/H_b = 100$. These results suggest that reverse simulation can create negative diffusion played by a certain level of wave number region.

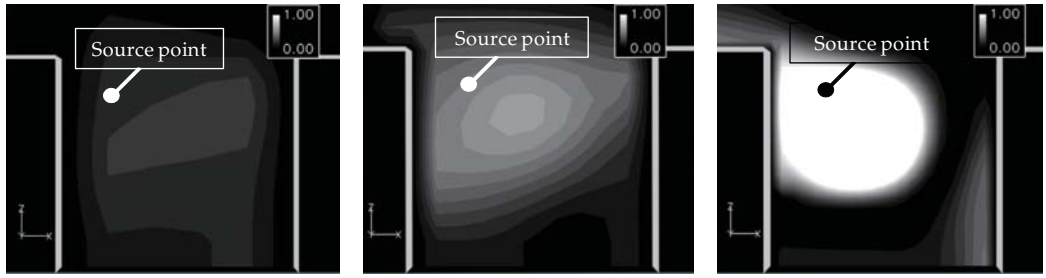

(a) (b) (c)

Figure 5: Reverse analysis results ($tU_b/H_b = 200$): (a) Case 1-1, (b) Case 2-1, and (c) Case 3-1.

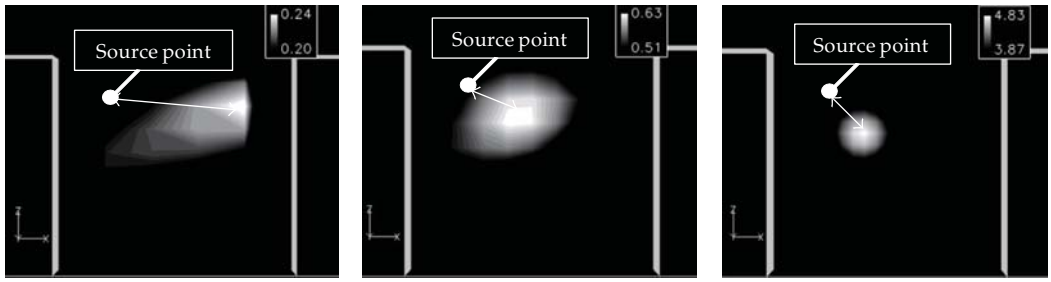

(a) (b) (c)

Figure 6: Peak concentration ($tU_b/H_b = 200$): (a) Case 1-1, (b) Case 2-1, and (c) Case 3-1.

3.2.2. The Influence of Filter Width

Figure 7 shows the results of Case 3-2 and Case 3-3, respectively. Comparing Case 3-1 with Case 3-2 and Case 3-3 reveals that the high concentration parts wash out as the filter widths are larger. This is because the high wave number region cut by a lowpass filter operation expands and negative diffusion played by the wave number region cannot be simulated. The results suggest that it is important for reverse simulation to decide on the filter width.

3.2.3. The Time Series of Concentration Center and Dispersion Width

The next figures concern the concentration center (X_{ic}) and dispersion width (σ_i). The concentration center and dispersion width are defined by (3.1) and (3.2), respectively. Equation (3.1) explains the average location of the concentration distribution. Equation (3.2) explains the average distance from the concentration center

$$X_{ic} = \frac{\iiint x_i C(x_1, x_2, x_3) dx_1 dx_2 dx_3}{\iiint C(x_1, x_2, x_3) dx_1 dx_2 dx_3}, \tag{3.1}$$

$$\sigma_i^2 = \frac{\iiint (x_i - X_{ic})^2 C(x_1, x_2, x_3) dx_1 dx_2 dx_3}{\iiint C(x_1, x_2, x_3) dx_1 dx_2 dx_3}. \tag{3.2}$$

Figure 8 shows the time-lines of the concentration centers of the streamwise direction. It shows the forward analysis from 0 to 100 and the reverse analysis from 100 to 200.

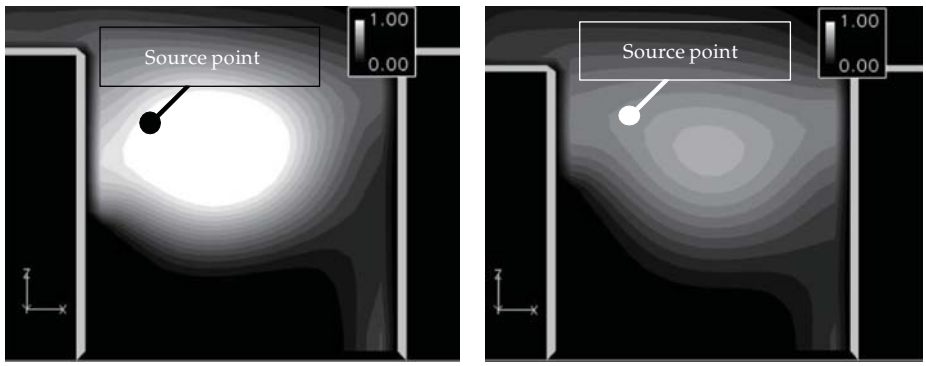

(a) (b)

Figure 7: Reverse analysis results ($tU_b/H_b = 200$): (a) Case 3-2 and (b) Case 3-3.

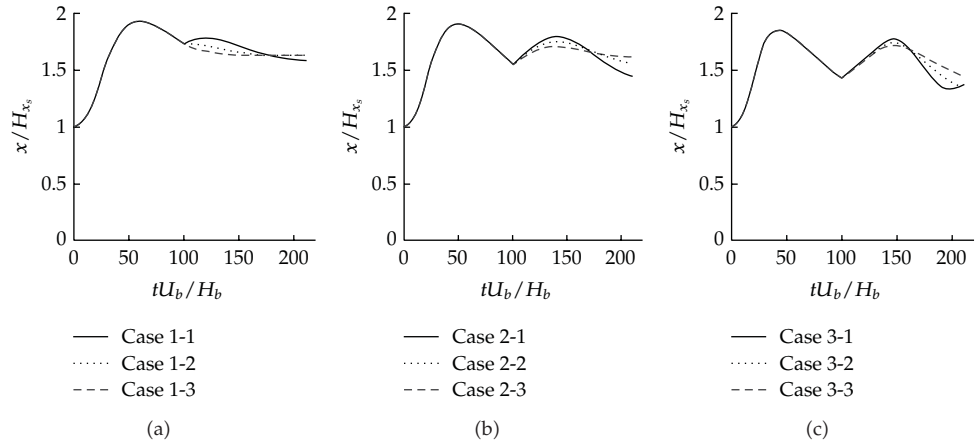

(a) (b) (c)

Figure 8: Time lines of concentration center of streamwise direction. (a) Case 1, (b) Case 2, and (c) Case 3.

The horizontal axes explain time that is normalized by U_b and H_b. The vertical axes explain the concentration center that is normalized by H_{x_s}, which is the emission point of the streamwise direction. At $tU_b/H_b \fallingdotseq 50$, the concentration centers change greatly in all cases. This is because the streamlines change greatly. When using the coarsest grid resolution (Case 1) in reverse simulation, the distribution cannot be caught. However, as the grid resolution is finer, the distribution can be perceived. In addition, we can confirm that the time-line curves become hardened with increase in filter width. In particular, the dependence on the grid resolution and filter width has a greater impact at $tU_b/H_b \fallingdotseq 150$ (corresponding to $tU_b/H_b \fallingdotseq 50$ in forward analysis), at which the concentration centers change greatly. The great time-variation at $tU_b/H_b \fallingdotseq 150$ cannot be simulated with Case 1-3, which has the coarsest grid resolution and the broadest filter width. However, the variation can be simulated perceptively with Case 3-1, which has the finest grid resolution and the narrowest filter width.

Figure 9 shows the time lines of the concentration centers of the vertical direction. The vertical axes explain the concentration center that is normalized by H_{z_s}, which is the emission point of the vertical direction. At $tU_b/H_b \fallingdotseq 30$, the concentration centers change greatly in all cases. This is because the streamlines change greatly as with those of the

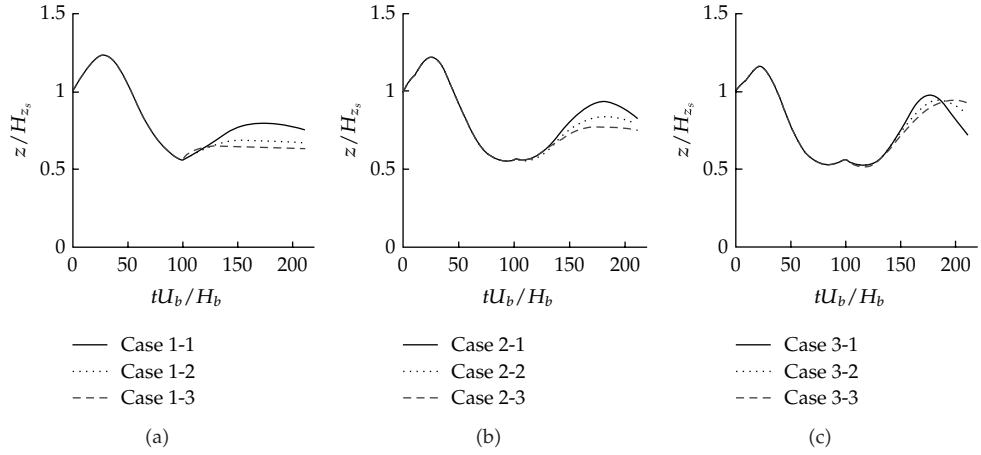

Figure 9: Time lines of concentration center of vertical direction. (a) Case 1, (b) Case 2, and (c) Case 3.

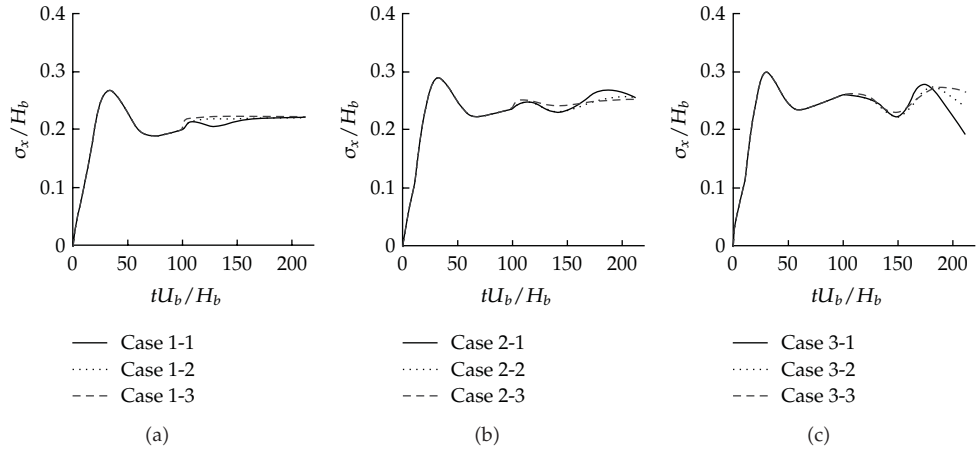

Figure 10: Time lines of concentration dispersion width of streamwise direction (a) Case 1, (b) Case 2, and (c) Case 3.

streamwise direction. The distributions can be caught in reverse simulation, as the grid resolution is higher and the filter width is narrower. This suggests that the dependence of the reverse simulation accuracy on the grid resolution and filter width have a greater impact at $tU_b/H_b \fallingdotseq 170$ (corresponding to $tU_b/H_b \fallingdotseq 30$ in forward analysis).

Figure 10 shows the time lines of the concentration dispersion widths of the streamwise direction. We can see that the dispersion widths have maximum value at $tU_b/H_b \fallingdotseq 30$ in all cases. The distributions cannot be caught adequately by reverse analysis with Case 1 and Case 2. The analysis with Case 2-1, which has middle grid resolution, and the narrowest filter width in Case 2, can only slightly catch the distribution. Meanwhile, reverse analysis with Case 3, which has the highest grid resolution can catch the distribution exactly, especially Case 3-1. In addition, no analysis case makes the dispersion width zero at $tU_b/H_b = 200$ because negative diffusion played by the high wave number is cut by the lowpass filter operation. Figure 11 shows the time lines of the concentration dispersion widths of the vertical direction. In forward analysis, the dispersion widths in all cases monotonically increase until $tU_b/H_b \fallingdotseq 50$ and remain virtually constant until $tU_b/H_b = 100$.

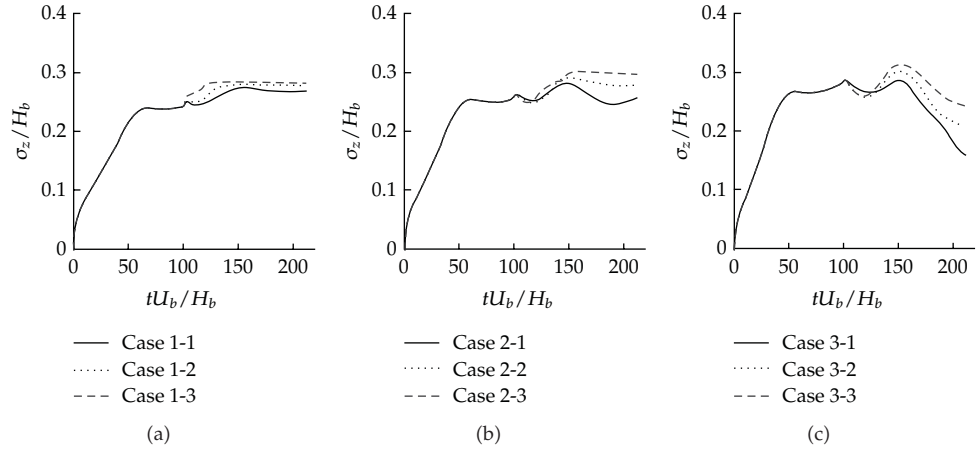

Figure 11: Time lines of concentration dispersion width of vertical direction (a) Case 1, (b) Case 2, and (c) Case 3.

Reverse simulation with Case 1 cannot catch the time series variation. Reverse simulation with Case 2 also cannot catch the negative diffusion adequately. Regarding Case 3, reverse simulation with Case 3-2 and Case 3-3 overestimate the time series variation at $tU_b/H_b \fallingdotseq 150$ (corresponding to $tU_b/H_b \fallingdotseq 50$ in forward analysis). On the other hand, the simulation with Case 3-3, which has the highest grid resolution, can precisely catch the time series variation. In addition, no analysis cases make the dispersion width zero at $tU_b/H_b = 200$ as with that of the streamwise direction because negative diffusion played by the high wave number is cut by the lowpass filter operation.

Figure 12 shows the relationship between coefficients of filter operation and the distance (L) between the concentration center and the real source point as the initial condition normalized by H_b. The horizontal axis explains the coefficient of filter operation normalized by H_b. The vertical axis explains the normalized distance. As the filter effect gets smaller, the distance shrinks. This means that the reverse simulation accuracy is more sensitive with the smaller filter effect. We can expect that reverse simulation accuracy can do better if the simulation is carried out with finer grid resolution.

As shown above, the dependence of reverse simulation on the grid resolution is stronger than that of forward analysis. In addition, the reverse simulation which uses high grid resolution is a useful method for identifying a pollutant source.

4. Discussion

The dependence of reverse simulation on the grid resolution and filter width is higher than that of forward analysis, as described above. The reason for this dependence is as follows.

Equation (4.1) shows a one-dimensional diffusion equation. For the sake of shorthand, the diffusion coefficient (Γ) is a constant and positive value

$$\frac{\partial C}{\partial t} = \Gamma \frac{\partial^2 C}{\partial x^2}. \tag{4.1}$$

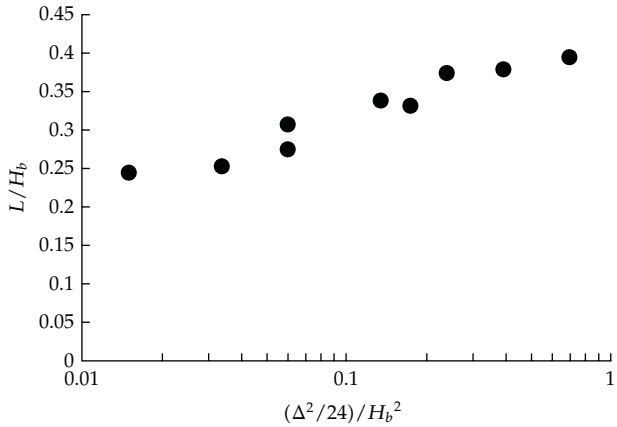

Figure 12: Relationship between coefficients of filter operation and the distance between the concentration center and the real source point in each case.

Equation (4.1) is converted into (4.3) by (4.2) (Fourier transform). k shows the wave number, and i shows the imaginary unit. $\widetilde{C}$ shows the concentration intensity in each wave number

$$C(x,t) = \int_{-\infty}^{\infty} \widetilde{C}(k,t)\exp(ikx)dk_i, \tag{4.2}$$

$$\frac{\partial \widetilde{C}}{\partial t} = -\Gamma k^2 \widetilde{C}. \tag{4.3}$$

Equation (4.3) explains that $\widetilde{C}$ decays over time. Moreover, the decay effect grows strong with progressing high wave number, because the coefficient of the right-hand side of (4.3) has $-k^2$.

In reverse simulation, (4.3) is converted to (4.4). The sign of the right hand side of (3.2) is opposite to that of (3.2) ($-k^2 \rightarrow k^2$)

$$\frac{\partial \widetilde{C}}{\partial t} = \Gamma k^2 \widetilde{C}. \tag{4.4}$$

This equation explains that $\widetilde{C}$ increases over time and the increase effect in the high wave number region is stronger than that in the low wave number region. However, when analyzing the diffusion equation with CFD, there are rounding errors in the unresolved high wave number region. For this reason, $\widetilde{C}$ in the high wave number region grows excessively and the numerical simulation breaks down.

Next, (4.5) shows the lowpass-filtered diffusion equation by (2.8)

$$\frac{\partial C}{\partial t} = -\Gamma\left(\frac{\partial^2 C}{\partial x^2} + \frac{\Delta^2}{24}\frac{\partial^4 C}{\partial x^4}\right). \tag{4.5}$$

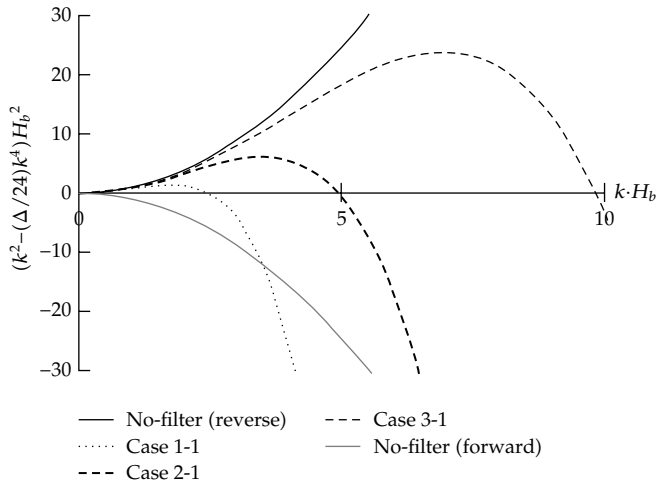

Figure 13: Coefficients of right-hand side of (4.1), (4.2), and (4.4) in each wave number (Case 1-1, Case 2-1, Case 3-1).

Equation (4.5) is converted into (4.6) by (4.2)

$$\frac{\partial \widetilde{C}}{\partial t} = \Gamma\left(k^2 - \frac{\Delta^2}{24}k^4\right)\widetilde{C}. \tag{4.6}$$

The second term of the right-hand side added by filter operation can be seen.

Figure 13 shows coefficients of the right-hand side of (4.3), (4.4), and (4.6). The horizontal axis explains the wave number normalized by H_b, and the vertical axis explains the coefficient of the right side of the equations normalized by H_b in each analysis case (Case 1-1, Case 2-1, Case 3-1). This figure shows the dependence of reverse simulation on the grid resolution. The figure suggests that the negative diffusion played by the low wave number can be simulated even in case of filtered equations. However, coefficients of filtered equations in the high wave number region decline. In particular, above a certain weave number, the coefficients become of negative value. This suggests that $\widetilde{C}$ in the wave number region decays over time. For this, the lowpass filter operation can suppress the increase of rounding errors and the numerical stability improves in reverse simulation. In addition, the wave number regions that negative diffusion can simulate are different in each grid resolution (see Table 2). The wave number becomes very low when using the lowest grid resolution (Case 1). Meanwhile, when using the highest grid resolution (Case 3), the simulated wave number is extended to the high wave number region.

Figure 14 shows coefficients of the right-hand side of (4.3), (4.4), and (4.6). The vertical axis explains the coefficients normalized by H_b in each case (Case 3-1, Case 3-2, Case 3-3). This figure shows the dependence on filter width. This suggests that the wave number regions that can be simulated by negative diffusion are different in each filter width (see Table 2). When using the largest filter width (Case 3-3), the simulated wave number region becomes very low. Meanwhile, when using the narrowest filter width (Case 3-1), the simulated wave number is extended to the high wave number region.

That is the reason for the dependence of reverse simulation on the grid resolution and filter width.

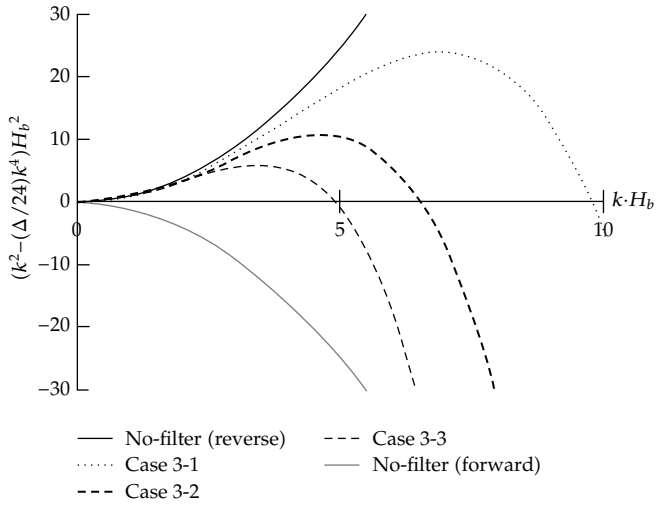

Figure 14: Coefficients of right-hand side of (4.1), (4.2), and (4.4) in each wave number (Case 3-1, Case 3-2, Case 3-3).

5. Conclusion

Reverse simulation is a method of identifying the source of a pollutant and is categorized as a backward method. This paper introduces the result of reverse simulation using RANS analysis in a cavity flow. With a low grid resolution or an excessively large filter width, the concentration distribution of the simulation result spreads widely. This means that the reverse simulation is less accurate and cannot be applied for identifying the pollutant source. Nevertheless, with a fine grid resolution and appropriate filter width, reverse simulation is applicable for identifying the source location.

Furthermore, this paper discusses the dependence of reverse simulation on the grid resolution and filter width with a one-dimensional diffusion equation. The simulated negative diffusion varies greatly according to the grid resolution and filter width. This is important knowledge for applying reverse simulation to practical problems.

In future, reverse simulation should be tried in various comprehensive flows and the applicability surveyed.

Acknowledgment

The present study was supported by the Kondo Jiro Grant of the Asahi Glass Foundation.

References

[1] X. Liu and Z. Zhai, "Inverse modeling methods for indoor airborne pollutant tracking: literature review and fundamentals," *Indoor Air*, vol. 17, no. 6, pp. 419–438, 2007.

[2] B. J. Wagner, "Simultaneous parameter estimation and contaminant source characterization for coupled groundwater flow and contaminant transport modelling," *Journal of Hydrology*, vol. 135, no. 1–4, pp. 275–303, 1992.

[3] A. D. Woodbury and T. J. Ulrych, "Minimum relative entropy inversion: theory and application to recovering the release history of a groundwater contaminant," *Water Resources Research*, vol. 32, no. 9, pp. 2671–2681, 1996.

[4] R. M. Neupauer and J. L. Wilson, "Adjoint-derived location and travel time probabilities for a multidimensional groundwater system," *Water Resources Research*, vol. 37, no. 6, pp. 1657–1668, 2001.
[5] M. D. Sohn, R. G. Sextro, A. J. Gadgil, and J. M. Daisey, "Responding to sudden pollutant releases in office buildings: 1. Framework and analysis tools," *Indoor Air*, vol. 13, no. 3, pp. 267–276, 2003.
[6] S. M. Gorelick, B. E. Evans, and I. Remson, "Identifying sources of groundwater pollution: an optimization approach," *Water Resources Research*, vol. 19, no. 3, pp. 779–790, 1983.
[7] S. Alapati and Z. J. Kabala, "Recovering the release history of a groundwater contaminant via the non-linear least squares estimation," *Hydrological Processes*, vol. 14, pp. 1003–1016, 2000.
[8] A. N. Tikhonov and V. Y. Arsenin, *Solutions of Ill-Posed Problems*, Winston and Sons, New York, NY, USA, 1977.
[9] T. H. Skaggs and Z. J. Kabala, "Recovering the release history of a groundwater contaminant," *Water Resources Research*, vol. 30, no. 1, pp. 71–79, 1994.
[10] P. Seibert, A. Frank, and H. Kromp-Kolb, "Inverse modelling of atmospheric trace substances on the regional scale with Lagrangian models," in *Proceedings of the EUROTRAC-2 Symposium*, P. Midgley and M. Reuther, Eds., Garmisch-Partenkirchen, Germany, March 2002.
[11] F. Hamba, S. Abe, D. Kitazawa, and S. Kato, "Inverse problem of one-dimensional diffusion equation from the point source," *Seisan Kenkyu*, vol. 63, no. 1, pp. 69–73, 2011 (Japanese).
[12] T. H. Skaggs and Z. J. Kabala, "Recovering the history of a groundwater contaminant plume: method of quasi-reversibility," *Water Resources Research*, vol. 31, no. 11, pp. 2669–2673, 1995.
[13] S. Abe and S. Kato, "A study on improving the numerical stability in reverse simulation," *Journal of Environmental Engineering*, vol. 75, no. 656, pp. 891–897, 2010 (Japanese).
[14] S. Abe and S. Kato, "Study on improving numerical stability by applying filter operation to concentration flux for reverse simulation to identify pollutant source," *Journal of Environmental Engineering*, vol. 76, no. 662, pp. 431–438, 2011 (Japanese).
[15] M. Kato and B. E. Launder, "The modeling of turbulent flow around stationary, and vibrating square cylinder," in *Proceedings of the 9th Symposium Turbulent Shear Flow*, pp. 1041–1046, 1993.
[16] J. A. Viecelli, "A computing method for incompressible flows bounded by moving walls," *Journal of Computational Physics*, vol. 8, no. 1, pp. 119–143, 1971.

Hindawi Publishing Corporation
Journal of Applied Mathematics
Volume 2012, Article ID 917650, 17 pages
doi:10.1155/2012/917650

Research Article

Computational Fluid Dynamics Simulation of Multiphase Flow in Structured Packings

Saeed Shojaee,[1] Seyyed Hossein Hosseini,[2] and Behzad Saeedi Razavi[3]

[1] *Department of Chemical Engineering, University of Sistan and Baluchestan, Zahedan 98164-161, Iran*
[2] *Department of Chemical Engineering, Faculty of Engineering, Ilam University, Ilam 69315-516, Iran*
[3] *Institute of Standard and Industrial Research of Iran, Khorasan Razavi 9185837733, Iran*

Correspondence should be addressed to Seyyed Hossein Hosseini, s.h.hosseini@mail.ilam.ac.ir

Received 29 November 2011; Revised 6 March 2012; Accepted 7 March 2012

Academic Editor: Fu-Yun Zhao

A volume of fluid multiphase flow model was used to investigate the effective area and the created liquid film in the structured packings. The computational results revealed that the gas and liquid flow rates play significant roles in the effective interfacial area of the packing. In particular, the effective area increases as the flow rates of both phases increase. Numerical results were compared with the Brunazzi and SRP models, and a good agreement between them was found. Attention was given to the process of liquid film formation in both two-dimensional (2D) and three-dimensional (3D) models. The current study revealed that computational fluid dynamics (CFD) can be used as an effective tool to provide information on the details of gas and liquid flows in complex packing geometries.

1. Introduction

Corrugated sheet structured packing has been widely used in gas-liquid contacting devices of industrial application for improving performance [1]. Several parameters cause the structured packings to be popular: attaining the minimal pressure drop per theoretical stage while achieving high separation efficiency, allowing reduction in energy dissipation, increasing loading capacity, and increasing the flooding capacity to its higher values [2].

Structured packings are made of corrugating metal or plastic sheets that are arranged side by side with opposing channel orientations. Channels are oriented with the angle of $\pm\beta$ from the horizontal direction. This angle usually varies from 45° to 60°. To create the elements, corrugated sheets are alternately arranged parallel to one another. Structured packing

performance depends on the characteristic of the corrugation geometry. The 45°-corrugation-angle structured packings are prevalent in the gas-liquid separation industry. The 60°-corrugation angle is designed for high capacity processes.

The rate of mass transfer for a structured packed column strongly depends on the effective interfacial area of the bed. In most cases, the effective surface for mass transfer is different from the geometrical surface area of the sheets due to the effects of hydraulic conditions and physical interactions that influence the spreading of liquid on the sheets.

A number of theoretical, semiempirical, and empirical correlations for predicting the effective interfacial area in structured packings have been reported in the literature. These models are developed for different packings and various process conditions using physical measurement methods such as electroresistivity and light transmission. Only a few researchers have reported actual interfacial areas for limited kinds of structured packings [3]. Most of the distillation data used in the correlations reported in the literature have been extracted under total reflux conditions. Thus, the liquid and gas velocities effects could not be studied separately from the available data. In some reported models, there is no explicit effect of the gas velocity, and only the liquid phase effects are considered to include the effect of surface wetting. Only a very few works consider the consequence of gas loading [4, 5]. Some researchers have suggested that the interfacial area can be larger than the packing geometry area; however, there are some disagreements on this issue. A brief review of the parameters that influence the interfacial area has been presented in the previous work [6].

The wetting process of the packing surface is quite complex and is not fully understood. In the recent years, computational fluid dynamics (CFD) has become a useful tool for analyzing multiphase flows in various industrial applications. In particular, CFD provides the capability to reduce a number of required experiments for describing the flow pattern inside complex geometries such as structured packings; as a result, it reduces the cost of design for the required equipment.

There have been a number of computer modeling flows in structured packings. For simulating the hydrodynamics of liquid phase flow in structured packing filled with catalyst pellets, Van Gulijk [7] used the Toblerone model, simplified the multiphase flow for a single phase in the channels, and evaluated the transversal dispersion in the structured packed bed. Van Baten et al. [8, 9] investigated the liquid dispersion and gas and liquid phase mass transfer between two sheets of KATAPAK-S structured packing using CFD tool. They considered mass transfer of the gas phase in an empty channel, as well as liquid phase mass transfer within the catalyst-packed channels. Petre et al. [10] and Larachi et al. [11] proposed the structured packing as a combination of four representative elementary 3D units (REU) and evaluated the dry pressure drop of the bed. Szulczewska et al. [12] employed a 2D model, and assumed countercurrent gas-liquid flows, to investigate the mechanisms of droplet formation and liquid film breakup over both flat and corrugated vertical plates. They evaluated the gas-liquid interfacial area using film thickness in a 2D model. Based on Petre and Larachi's work [10, 11], Raynal et al. [13] predicted the dry pressure drop of structured packing. They estimated the thickness of the liquid film and consequently the liquid hold-up in a structured packing under cocurrent flow using the VOF approach. Ataki and Bart [14] applied the flat packing element of Rombopak 4 M in their CFD models and described the degree of wetting and the effective area. They also investigated the effect of liquid properties on the degree of wetting. Haghshenas Fard et al. [15] presented a CFD model to predict both dry and wet pressure drops for the entire packing module. They also determined the mass transfer efficiency of the packing in two packing sheets. Mahr and Mewes [16] proposed a model for two-phase flows in columns with structured packing. They calculated the pressure

drop in the packing at different angles and directions. Using this model, the macroscopic flow field of countercurrent two-phase flow could be evaluated in strong anisotropic porous structures. Khosravi Nikou and Ehsani [17] implemented different turbulence models to study the flow through structured packings and investigated heat and mass transfers in the packing. Fernandes et al. [18, 19] assumed uniform wetting of the packing surface and presented a pseudo single-phase CFD model for determination of wet pressure drops of a Sulze BX packing element in supercritical fluid extraction process.

In summary, a few studies have been reported in the existing literature that use CFD techniques for evaluating the effective areas in structured packings while most of the studies are restricted to prediction of the pressure drop and the use of 2D models for the two-phase flow simulations. In addition, liquid film thickness in 2D and 3D frameworks was investigated rarely in the past. In this study, a 3D computational framework was used by considering multiphase flow for the domain within two layers of the largest element of the structured packings. The evaluation of the effective area was based on the liquid film thickness using the VOF method in the 3D simulation. Countercurrent motions of air and water as gas and liquid phases, respectively, were analyzed, and the effective areas, liquid hold-up, liquid and gas velocities as well as liquid film thickness were evaluated. 2D model was evaluated to study liquid film thickness besides the 3D computational domain.

2. Numerical Simulations

2.1. Governing Equations

The simulations are carried out using the volume of fluid (VOF) model. The VOF approach is well suited for tracking the interface between the two immiscible phases, namely, the gas-liquid interface. VOF solves a single set of momentum equations throughout the domain, while keeping track of the volume of phases in each computational cell. The resulting velocity in each cell is the mass averaged values of the phases present in the cell. The corresponding momentum balance equation for the two-phase flow is given as

$$\frac{\partial}{\partial t}\left(\rho\vec{v}\right) + \nabla\cdot\left(\rho\vec{v}\vec{v}\right) = -\nabla\cdot P + \nabla\cdot\left[\mu\left(\nabla\vec{v} + \vec{v}^{T}\right)\right] + \rho\vec{g} + \vec{F}, \tag{2.1}$$

where ρ is the fluid density and $\vec{v}$ the velocity vector. In addition, P, $\rho\vec{g}$, and $\vec{F}$ are the static pressure, the gravitational body force, and the external body forces, respectively. Equation (2.1) involves the volume fractions of both phases that enter through the physical properties of the phases such as density and viscosity. Accordingly, the phase-averaged properties are given as

$$\begin{aligned}\rho &= \alpha_1\rho_1 + \alpha_2\rho_2,\\ \mu &= \alpha_1\mu_1 + \alpha_2\mu_2,\end{aligned} \tag{2.2}$$

where ρ and α are density and volume fractions and the subscripts correspond to the phases. In each control volume, summation of all the phase volume fractions is equal to unity. That is,

$$\sum_{i=1}^{n}\alpha_i = 1. \tag{2.3}$$

The tracking of the interface is done in the cells where the volume fraction is different from 0 or 1. If a cell is completely filled with one phase, the volume fractional of that phase in the cell is equal to unity ($\alpha = 1$), and the cell is considered to be in the main flow region of that phase. A cell is considered to be on the (interface) free surface when the value of volume fraction is between 0 and 1 ($0 < \alpha < 1$). The tracking of the interface(s) between the phases is accomplished by the solution of a continuity equation for the volume fraction of one (or more) of the phases. For the ith phase this equation is written as

$$\frac{\partial}{\partial t}\left(\alpha_i \rho_i\right) + \nabla \cdot \left(\alpha_i \rho_i \vec{v}_i\right) = 0. \tag{2.4}$$

In the present study, mass transfer terms between the immiscible water and air phases are neglected [18, 19]. The VOF model, however, accounts for the effect of surface tension along the interface between the phases. The surface tension model used in these simulations is the continuum surface force (CSF) model that was proposed by Brackbill [20]. The CSF model can be augmented by the additional prescription of the contact angles between the phases and the walls. The wall may absorb the liquid (wetting wall) or repel the liquid (nonwetting wall), and the contact angle varies depending on the hydrophobicity of the wall. The equilibrium contact angle depends also on the smoothness of the wall [20].

One important part of a CFD simulation is the use of an appropriate turbulence model. In the present study, based on previous work [21] and the CFD model of Khosravi Nikou and Ehsani [17] for simulation of a structured packing, the BSL model (the baseline k-ω model) is used for the present simulations. The main problem with the k-ω model is its well-known strong sensitivity to free stream conditions. This is undesirable, and, in order to solve the problem, the BSL model that is a blending between the k-ω model near the surface and the k-ε model in the outer region is developed.

Typically, the relative error between two successive iterations is specified using a convergence criterion of 10^{-4} for each scaled residual component. It might be worth mentioning the computational time required for each 3D simulation run, which is about 6-7 days while this time duration is about 20–25 hours for each 2D simulation run on a Pentium 4 CPU running on a quad-core 3.2 GHz with 4 GB of RAM.

For the current simulations, the phases are air and water. The fluids are assumed to be Newtonian, isothermal, and incompressible; therefore, their properties are kept constant. The computations are conducted under the unsteady state condition, with a time step of 0.002 sec until a pseudosteady state is reached. Pseudosteady conditions are established when the mass flow rates at the outlets do not change. The physical properties of the phases and the geometrical characteristics used in the simulations are listed in Tables 1 and 2.

2.2. Domain and Grid Arrangements

To investigate the effective area, the experimental setup of Rocha et al. [22] is utilized for validation and verification of the 3D CFD model. The computational space for the CFD model consists of 34 triangular channels, with a total number of 137 crossovers, which is shown in Figure 1. Since the thickness of the liquid film on the packing surface is very small, a refined structural grid is used for achieving better convergence and for decreasing the number of grid elements in the domain. The grids are dense near the wall for more accurate determination of the liquid film thickness, and they become coarser away from the wall.

Table 1: Physical properties of the system for simulations.

Physical properties	Air	Water
Density ρ (kg m^{-3})	1.185	997
Kinematic viscosity υ (m^2 s^{-1})	1.545 10^{-5}	8.926 10^{-7}
Surface tension σ (N m^{-1})	—	0.0728
Static contact angle with air steel	—	70–80°

Table 2: Geometrical characteristics for the simulated structured packing.

Packing type	Sulzer BX	Gempak 2A
Specific surface area (m^2/m^3)	500	223
Height of element (m)	0.185	0.2477
Void fraction (%)	90	95
θ (deg)	55	45
a_p (m^{-1})	—	223
Channel dimensions (m)		
Height of triangle (h)	0.006	0.0122
Base of triangle (b)	0.012	0.0267
Corrugation spacing (s)	0.009	0.018

Grid independence of the solution was tested through using several different grid sizes. Table 3 shows the predicted liquid film thickness using various mesh sizes. This table shows that when finer grids are used the predicted liquid film thickness is reduced. Against the coarse grids, the predicted liquid film thicknesses for both fine and medium grids are roughly close. The simulation running time on the fine grid takes considerable CPU time. Consequently, simulations are conducted on the medium grid with a total number of computational hexahedral cells of 1315200, 22100, and 17280 for 3D and 2D frameworks of Gempak 2A as well as 2D modeling of Sulzer BX, respectively.

To investigate liquid film formation on the packing in a 2D computational framework, the experimental setups of Rocha et al. [22] and Cho et al. [23] at Gempak 2A and Sulzer BX packings, respectively, are used. In a 2D domain, a cross-section of the packing channel is obtained when the duct between two corrugated plates is cut vertically.

2.3. *Initial and Boundary Conditions*

For the 3D model (Rocha et al. [22] setup) on the lower side of the packing sheets, the uniform inlet velocity boundary conditions are prescribed for both air and water phases. In this section of the packing, the velocity inlets are identified where gas and liquid velocities in that region have, respectively, positive and negative values to hold countercurrent flows in the simulation process. The outlet is defined on the upper side of the packing sheets using the pressure outlet boundary condition. At this boundary, the outlet static pressure is prescribed. A no-slip boundary condition is used for the gas and liquid phases on the lateral walls of the packing. The computational domain is assumed to be initially filled with air, and the initial volume fraction of the water is set to zero. In addition, the initial values of gas and liquid velocities are set to zero through the packing element.

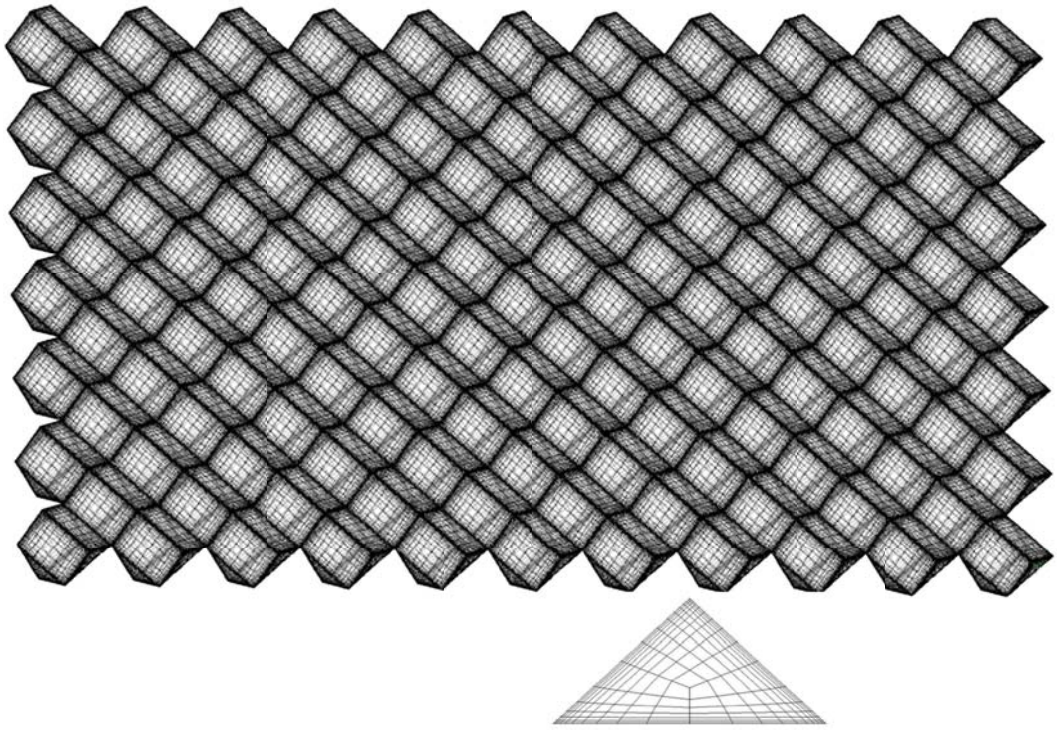

Figure 1: Computational domain for simulation and schematic overview of meshing of a triangular face.

Table 3: Liquid film thickness at different mesh sizes.

	Fine	Medium	Coarse
Rocha et al. [22] (for 3D modeling)			
Number of computational cells	1657700	1315200	771584
Liquid film thickness (mm)	0.26	0.269	0.372
Rocha et al. [22] (for 2D modeling)			
Number of computational cells	25000	22100	15500
Liquid film thickness (mm)	0.275	0.28	0.31
Cho et al. [23] (for 2D modeling)			
Number of computational cells	20000	17280	10500
Liquid film thickness (mm)	0.265	0.27	0.30

For the 2D two-phase flow simulations (Rocha et al. [22] and Cho et al. [23]), the liquid and gas inlet zones are defined with uniform inlet velocity boundary conditions. The outlets for liquid and gas are defined with an outflow boundary condition. The computational domain is assumed to be initially filled with air, and the initial volume fraction of the water is set to zero. At the walls, a no-slip boundary condition for gas and liquid phases is imposed according to the previous works. The static contact angle of $\gamma = 70^\circ$ is also assumed.

3. Results and Discussion

3.1. Pressure Drop

Pressure drop is an important measured parameter that can be used to validate hydrodynamic models of multiphase systems. Here the predicted pressure drops are compared with the experimental data. A commonly used model for determining mass transfer and pressure drop in structured packings was developed several years ago at the separations research program (SRP) of the University of Texas at Austin. Rocha et al. [22] treated structured packing as a network of wetted wall columns and theorized that the effective area, pressure drop, and hold-up should be all related. They proposed following correlation for dry pressure drop of the packings,

$$\frac{\Delta P_{\text{dry}}}{Z} = \frac{0.177\rho_G}{S\varepsilon^2(\sin\theta)^2}U_{gS}^2 + \frac{88.774\mu_G}{S^2\varepsilon\sin\theta}, \tag{3.1}$$

where U_{gS} and ε, respectively, are superficial gas velocity and void fraction of packing and S stands for side dimension of corrugation.

The irrigated pressure drop was also proposed by Rocha et al. [22], based on a generic channel model, as

$$\frac{\Delta P_{\text{dry}}}{Z} - \frac{\Delta P}{Z}\left[1 - (0.614 + 71.35S)h_L\right]^5 = 0. \tag{3.2}$$

The CFD results are compared with the corresponding experimental data and SRP model results. Figure 2 shows the predicted dry pressure drops of CFD tool and SRP model against the F-factor, $u_G(\rho_G)^{0.5}$, in the structured packing. The experimental data of Rocha et al. [22] are reproduced in this figure to compare with the CFD results and SRP model predictions. The mean absolute relative error of the CFD dry pressure drop is about 13.4%. A major reason for the under-prediction of the pressure drop in Figure 2 is that the junction effect between two consecutive packing layers is not considered in the simulations. More details regarding this effect are found in Petre et al.'s [10] work. Therefore, under-prediction of the pressure drop results of the present model is anticipated. However, the SRP model slightly overpredicts the pressure drop in comparison with the experimental data.

Figure 3 depicts the predicted irrigated pressure drops of CFD tool and SRP model against the F-factor in the structured packing. The experimental data of Rocha et al. [22] are again reproduced in this figure to compare with SRP model predictions and CFD results. As can be seen in this figure, the SRP model overestimates the wet pressure drop in the F-factor higher than $3.5\,\text{m/s}(\text{kg/m}^3)^{0.5}$ and predicts the best results in lower range of the F-factor. However, the CFD results show the same trend with the experimental data especially in higher F-factors. By reaching the flooding region, CFD predicts the better results in comparison with the SRP model. Generally, pressure drop in two-phase flow containing gas-liquid interaction is increasing due to the change in flow direction and gas-gas interactions. Therefore, the model predicts acceptable results in terms of dry and irrigated pressure drops. Consequently, the current model can be used to examine the behavior of the other hydrodynamic parameters in the structured packings.

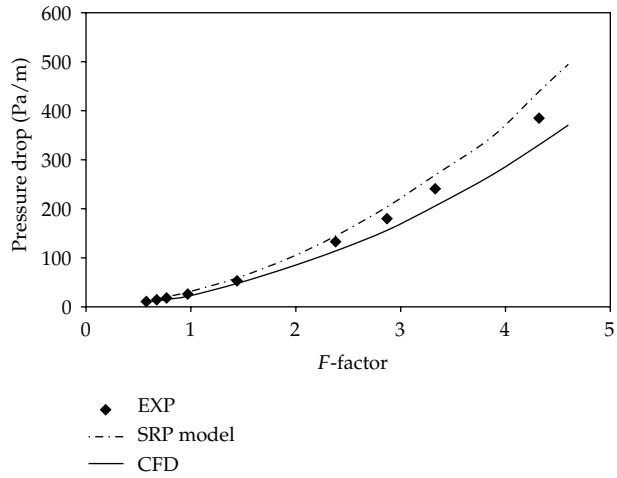

Figure 2: Comparison between predicted dry pressure drops of CFD tool and SRP model and experimental data [22] for different *F*-factors in the structured packing.

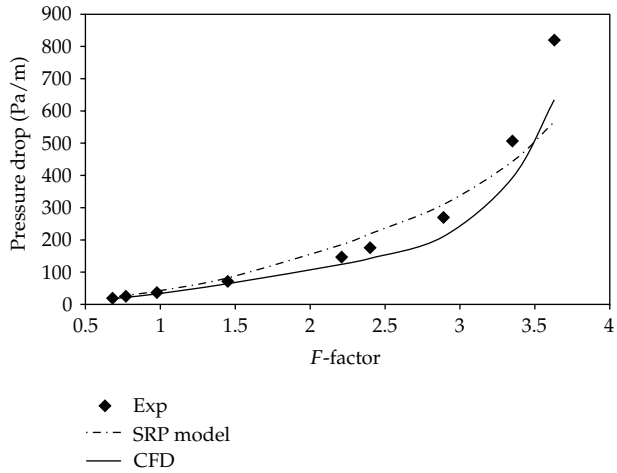

Figure 3: Comparison between predicted wet pressure drops of CFD tool and SRP model and experimental data [22] for different *F*-factors in the structured packing.

3.2. Effective Area

The effective area for mass transfer is defined as the absolute effective area divided by the packing volume (m^2/m^3). Knowledge of the value of this parameter and the effective factors upon it can be useful for the design of packings in separation columns. In this study, the effective area is evaluated from the values of liquid hold-up per estimated liquid film thickness based on the earlier work of Iliuta and Larachi [24]:

$$a_e = \frac{h_L}{\delta_{\mathrm{CFD}}}, \tag{3.3}$$

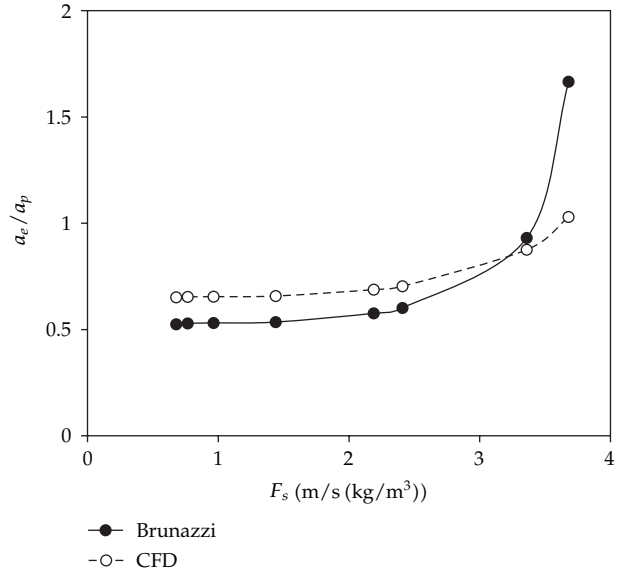

Figure 4: Comparison between the CFD results and the Brunazzi model by increasing gas velocity.

where a_e and δ_{CFD} represent the effective area of packing and average liquid film thickness. Simulations are carried out for a water superficial velocity of 0.007 m/s and different gas capacity factors ($F_s = u_G\sqrt{\rho_G}$). Based on the evaluated average thickness of the rivulets, the surface area of liquid rivulets is determined.

Figure 4 compares the CFD results for the ratio of the predicted effective interfacial area to the packing surface area (a_e/a_p) with the Brunazzi et al. [25] correlation. The use of the correlation suggested by Brunazzi et al. [25] requires only a simple experimental estimate of the liquid hold-up. The correlation is as follows:

$$\frac{a_e}{a_p} = \frac{d_{\mathrm{eq}}}{4}\left(\frac{h_L}{\varepsilon}\right)^{1.5}\left[\frac{\rho_L g\varepsilon(\sin\theta)^2}{3\mu_L u_L}\right]^{0.5}. \tag{3.4}$$

The simulation results show that, in the preloading zone, the effective area is a weak function of the gas flow rate. This is due to the weak interactions between gas and liquid phases. It is observed that with increasing the superficial gas velocity, the effective area of the packing is increasing, resulting in the corresponding mass transfer rate increase. At gas flow factor of 3.68 m/s (kg/m^3), the effective area is equal to the packing surface area. On the other hand, a higher gas rate increases the instability in liquid flow and leads to a higher effective interfacial area. The Brunazzi et al. [25] correlation predicts the rise of effective area and shows a good agreement with the CFD results. As can be seen in Figure 4, at the capacity higher than 3.25, the Brunazzi et al. [25] correlation overpredicts the effective area in comparison with the CFD results. It is also seen that the slope of the calculated curve by the Brunazzi et al. [25] correlation increases suddenly because experimental hold-up in this correlation reflects indirectly the gas velocity effect.

As it is shown in Figure 4, the computed fractional area, a_e/a_p, is approximately constant in the range of gas velocity (F_s) from 2.4 to 680 m/s (kg/m^3) but it increases with

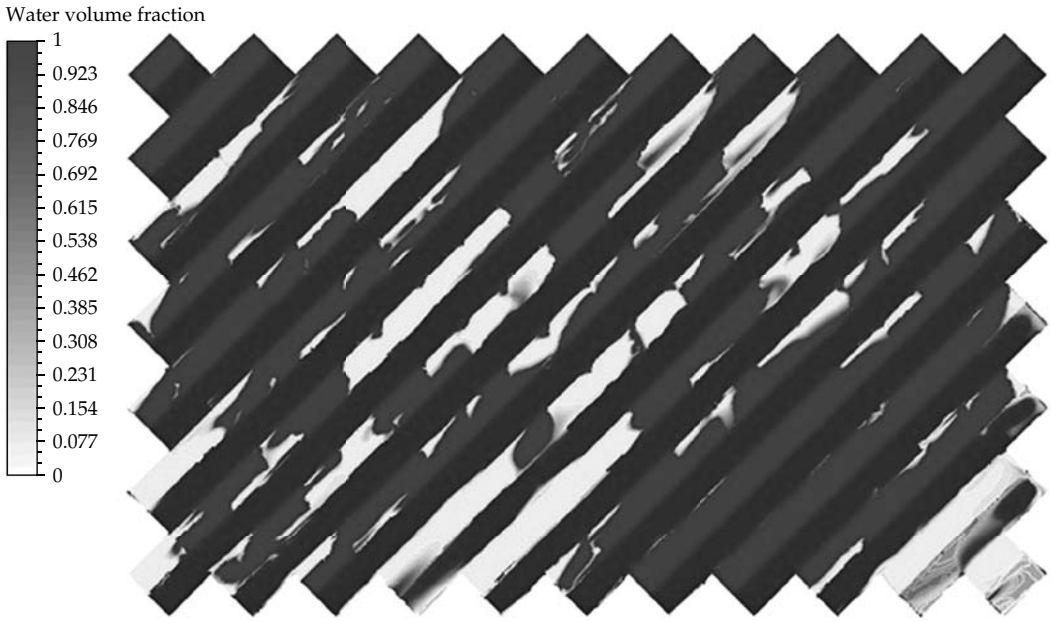

Figure 5: Typical liquid flow on surface of corrugation sheet.

increasing the gas velocity ($F_s > 2.41\,\mathrm{m/s\,(kg/m^3)}$). It is therefore concluded that, in addition to the liquid flow rate, the structured packing interfacial areas are moderately influenced by the gas flow rate.

The distribution of liquid on the surface of packing is a complex phenomenon. Figure 5 illustrates the liquid distribution on the corrugation sheet area. The presence of both dry and wet patches on the packing surface is clearly seen from this figure. This figure shows that liquid not only flows in the channel in which it has been supplied but also flows into the other channels. That is, the liquid is mixed with adjacent streams and the packing surface is covered by a thin liquid layer.

In this step, the laminar flow condition with the assumption that the gas phase does not flow in the packings is made. Thus, the gas phase is considered stagnant with zero velocity and does not affect the liquid flow. This assumption may be a reasonable starting approximation due to the fact that the gas flow has small effect on the liquid flow in the packing.

The efficiency of the packed columns strongly depends on the flow behavior of the liquid inside the packing. Figure 6 indicates a comparison between the CFD results with the Brunazzi et al. [25] correlation against the liquid load. This figure shows that, by increasing the liquid load, the effective area increases for the Brunazzi et al. [25] correlation as well as for the simulation results. When the entire surface area is covered by the liquid film, the effective area (a_e) remains roughly unchanged. For the area ratio, both the CFD results and the Brunazzi et al. [25] correlation lead to values that do not exceed one.

The possibility of a_e/a_p ratios in excess of unity is not explicitly discussed in the literature. It should be noted here that a_e/a_p ratios higher than one are possible in various gas-liquid mixing devices. An example is the spray towers, where this ratio becomes very

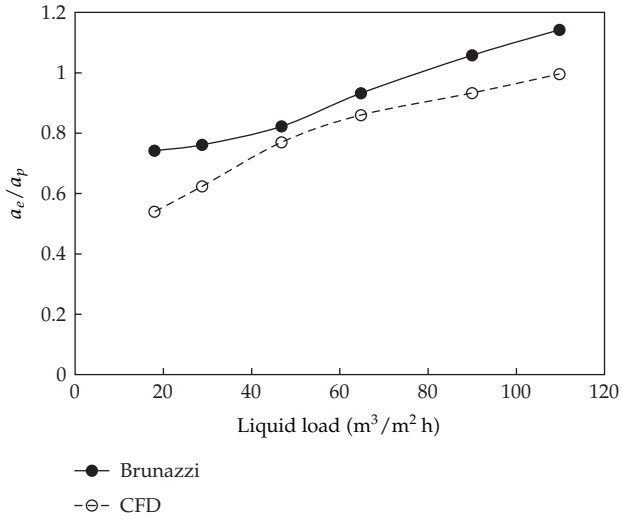

Figure 6: Comparison between the CFD results and the Brunazzi model by increasing the liquid load.

large [26]. Recently, several researchers have estimated the effective interfacial area of structured packings, a_e/a_p, with ratios higher than unity for the flooding regime [26, 27].

The Brunazzi et al. [25] model predicts an increase in the effective area by increasing the liquid loading. It can be seen that the model is in a good agreement with the CFD results especially in the intermediate range of liquid loadings.

Since the gas velocity is assumed zero, the liquid phase forms a film flow downward on the packing surface. Thus, the effective area becomes equal to the packing surface area. The results of the simulations shown in Figure 6 also show that at the flow rate of 109.8 m^3/m^2h, when $a_e = a_p$, the total packing surface is covered by water completely.

As an important result, the Brunazzi et al. [25] model, which has been derived based on several parameters, such as liquid hold-up value, geometric parameters, and physical properties of gas and liquid phases, predicts the interfacial area accurately without introducing any adjustable parameter. As noted before, it can be emphasized that the Brunazzi et al. [25] model is independent from the packing type.

Several researchers have studied the effective interfacial area for the different structured packings by experiments and using some published empirical models [28–30]. They have found a similar trend (qualitative agreement) with the results of this study (Figures 4 and 6) and different values of this term quantitatively. The difference in performance of various packings may be attributed to undesirable liquid pooling and bridging for the packings.

3.3. Liquid Flow Pattern

To verify the liquid flow pattern through the structured packing using CFD analysis, X-ray projection of the experimental work of Mahr and Mewes [16] is used for a simple comparison. In the Mahr and Mewes [16] study, the holes in the packing have been sealed in order to keep the liquid between both sheets. Predicted results by the CFD model for the liquid phase behavior confirm the Mahr and Mewes [16] findings. They did not consider gas flow in their measurements similarly to the current study. They found that the liquid film is created in

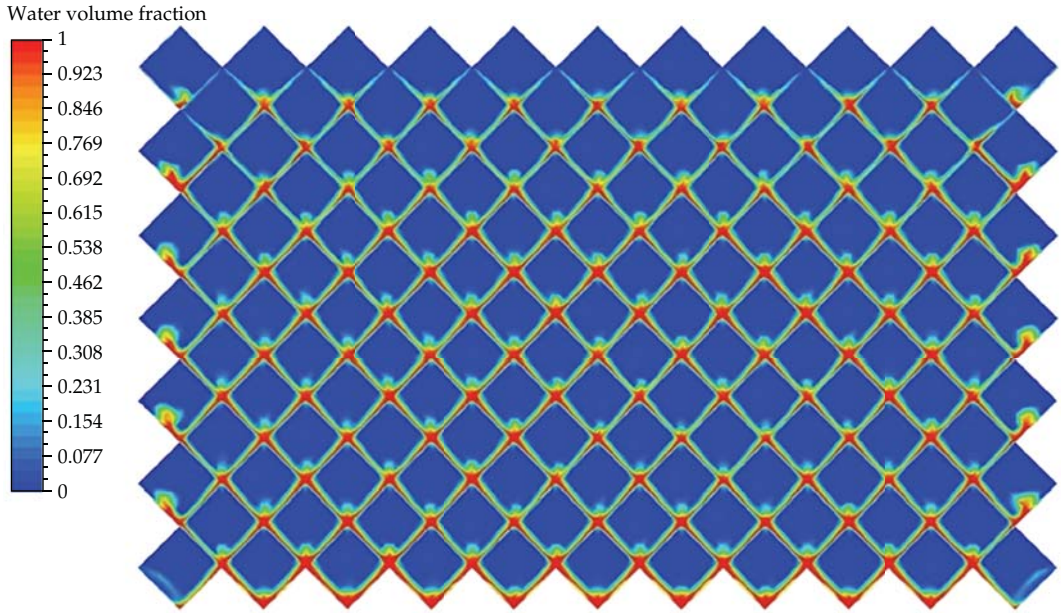

Figure 7: Computed liquid film flow on plane between two sheets of Gempak 2A structured packing using CFD.

both inner sides of the packing surface. Their finding is consistent with the current numerical results (Figure 7). Mahr and Mewes [16] observed that at a low liquid flow rate the majority of the liquid is conducted mainly along the flow path with an angle of ±19° with respect to the axial direction. Only a small amount of liquid is kept in the grooves of the corrugation due to surface tension, and the bulk of the liquid phase flows along the corrugation angle of ±42° toward both sides. A local minimum value of liquid hold-up is found straight below the injection point. The experimental results also show that the liquid phase spreads more toward the sides compared to the straight downward flow from the injection point.

Figure 7 shows the predicted liquid film flow on a plane throughout a packing element of Gempak 2A structured packing. The liquid, which flows down the side length of the corrugated sheet channels, mixes and redistributes at the contact points of two sheets. At the mixing point, the film thickness increases and decreases roughly periodically, due to the abrupt change in liquid flow direction and mixing liquid with adjacent streams. In addition, the distribution of liquid in Figure 7 and that in Mahr and Mewes [16] are symmetric with respect to the axial direction at the injection points.

3.4. Liquid Film Thickness

Two sets of 2D simulations for two-phase flows are performed. For the first case, the experimental condition of Cho et al. [23] for Sulzer BX packing is evaluated by the model. Computed size distribution of liquid film thickness along the Sulzer BX packing surface is shown in Figure 8 for a liquid velocity of 0.0101 m/s and F-factor of 0.8 m/s $(\mathrm{kg/m^3})^{0.5}$. It can be seen from the figure that the liquid film thickness is not uniform. Through a comparison between the Nusselt film thickness, which has been obtained based on the uniform liquid film thickness, and the averaged computed film thickness in the region lower than the loading,

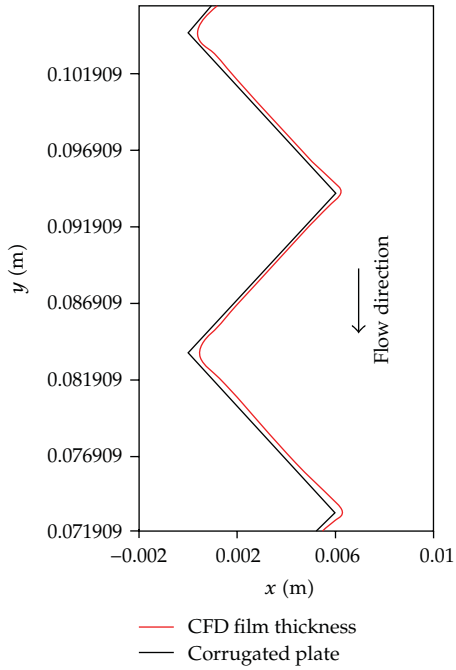

Figure 8: Predicted liquid film thickness along the packing for Sulzer BX at a liquid velocity of 0.0101 m/s and F-factor of 0.8 m/s $(\mathrm{kg/m^3})^{0.5}$.

it is found that the deviation is about 35%. The average computed liquid film thickness is 0.00027 m.

For the second set of study, the experimental condition of Rocha et al. [22] for Gempak 2A packing is simulated. The computed liquid volume fraction counters in the 2D model of Gempak 2A and Sulzer BX are shown in Figure 9. Here the liquid velocity and F-factor are, respectively, 0.007 m/s and 2.2 m/s $(\mathrm{kg/m^3})^{0.5}$. From this figure the presence of liquid films on the packing surfaces can be clearly seen, which vary in thickness. Nonuniformity of the film thickness can also be observed in the 3D model results (Figure 7). Figure 9, however, shows that the liquid film thickness in the Gempak 2A packing is more uniform compared to the Sulzer BX. It is also seen that the liquid film is thicker at the intersection of the plates and decreases with distance. Moreover, the liquid film thickness in Gempak 2A packing is thinner than that in Sulzer BX. That is particularly the case at the cornets. When the dimensions of the packing become larger, Gempak 2A, liquid thickness decreases for a constant liquid load due to covering wide surface of the packing by the liquid phase. This behavior is logical; as a result the dimensions of the packing can influence the liquid film thickness.

4. Conclusions

The CFD model for countercurrent two-phase flows in a structured packing was validated by comparison with the experimental data and well-known empirical models of Brunazzi et al. [25] and SRP [22]. The CFD model described the influences of hydrodynamics parameters such as gas velocity and liquid load on the effective mass transfer area. The simulation results indicated that the gas flow rate is an important factor for the mass transfer performance.

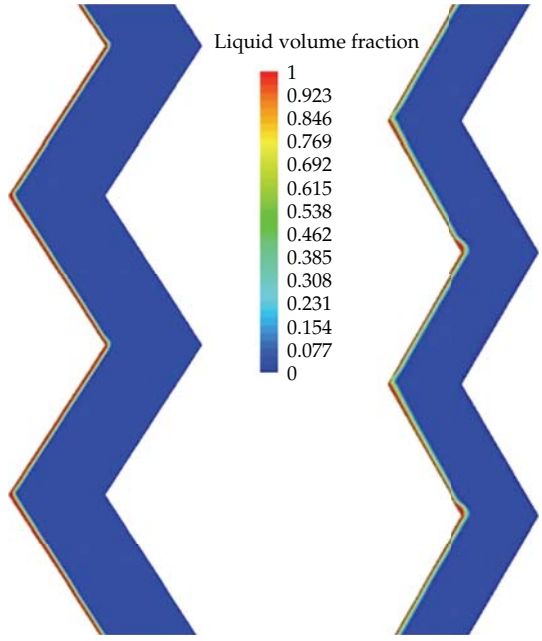

Figure 9: Contours of liquid volume fraction for 2D modeling of Gempak 2A and Sulzer BX (U_L = 0.007 m/s; F-factor = 2.2 m/s $(\text{kg/m}^3)^{0.5}$.

Increasing kinetic energy of gas flow to increase the liquid hold-up generates instabilities in liquid film, formation of surface ripples, and creation of droplets that result in higher interfacial area and thus increases the efficiency. An increase of the liquid wetting caused an increase in the packing surface until the liquid covered the entire surface. Beyond that, the rate of increase is small. In addition, the simulations showed that the CFD model is capable for determining the minimum flow rates for an entire surface of structured packing covered with the liquid. CFD tool emphasized the general applicability of the Brunazzi et al. [25] model for the various types of structured packings at different gas and liquid flow rates.

Studying the liquid film flow over the packing surfaces by CFD simulation can lead to a better understanding of the role of the effective parameters on the gas-liquid mass transfer. The process of liquid film formation on the packing surface was studied in details and the parameters that influence the liquid film thickness were discussed. It was shown that, inside the two sheets of structured packing, the maximum thickness of the liquid film was near the contact points of the sheets where liquid was redistributed over the corrugated surface. Such behaviour was observed in both 2D and 3D modelings. CFD showed that the dimensions of the packing could influence the liquid film thickness. In addition, considering uniform liquid film thickness, Nusselt assumption on the structured packings is unacceptable. This matter was observed in both 2D and 3D modelings.

Nomenclature

A: Packing type and size-dependent constants
a_e: Effective mass transfer area, m^2/m^3

a_L: Effective liquid flow angle
a_p: Specific area of packing, m^2/m^3
b: Corrugation base dimension, m
B: The packing type and size-dependent constants
d_{eq}: Equivalent diameter of flow channel
d_h: Hydraulic diameter of packing defined by $4\varepsilon/a_p$
$\vec{F}$: Additional forces in the Navier-Stokes equations, N
F_s: Gas capacity factor, $u_G(\rho_G)^{0.5}$, $m/s(kg/m^3)^{0.5}$
g: Gravitational acceleration, m/s^2
h: Corrugation crimp height, m
h_L: Liquid hold-up, —
P: Pressure
S: Corrugation side length, m
t: Time, s
u: Velocity, m/s
U_{gS}: Superficial gas velocity, m/s
$\vec{v}$: velocity vector
Z: Packed height, m.

Dimensionless Numbers

Fr $= u^2/gd_h$: Froude number
Re $= ud_h/\upsilon$: Reynolds number
We $= u^2\rho d_h/\sigma$: Weber number

Greek Letters

α: Volume fraction, —
γ: Static contact angle, degree
δ: Liquid film thickness, mm
ε: Void fraction of packing, —
θ: Corrugation angle (with respect to the horizontal), degree
μ: Viscosity, Pa .s
ν_L: Liquid kinematic viscosity, m^2/s
ρ_L: Liquid density, kg/m^3
σ: Surface tension, N/m
Ω: Packing surface void fraction.

Subscripts

G: Gas phase
i: Index
L: Liquid phase
n: Number of phases.

References

[1] Z. Olujic, M. Behrens, L. Colli, and A. Paglianti, "Predicting the efficiency of corrugated sheet structured packings with large specific surface area," *Chemical and Biochemical Engineering Quarterly*, vol. 18, no. 2, pp. 89–96, 2004.

[2] E. Brunazzi, A. Paglianti, and L. Petarca, "Design of absorption columns equipped with structured packings," *Chimica & Industria*, vol. 78, pp. 459–467, 1996.

[3] S. Shetty and R. L. Cerro, "Fundamental liquid flow correlations for the computation of design parameters for ordered packings," *Industrial and Engineering Chemistry Research*, vol. 36, no. 3, pp. 771–783, 1997.

[4] R. H. Weiland, K. R. Ahlgren, and M. Evans, "Mass-transfer characteristics of some structured packings," *Industrial and Engineering Chemistry Research*, vol. 32, no. 7, pp. 1411–1418, 1993.

[5] Z. P. Xu, A. Afacan, and K. T. Chuang, "Predicting mass transfer in packed columns containing structured packings," *Chemical Engineering Research and Design*, vol. 78, no. 1, pp. 91–98, 2000.

[6] S. Shojaee, S. H. Hosseini, A. Rafati Saleh, and G. Ahmadi, "Prediction of effective area in structured packings by CFD," *Industrial & Engineering Chemistry Research*, vol. 50, pp. 10833–10842, 2011.

[7] C. Van Gulijk, "Using computational fluid dynamics to calculate transversal dispersion in a structured packed bed," *Computers and Chemical Engineering*, vol. 22, no. 1, pp. S767–S770, 1998.

[8] J. M. Van Baten, J. Ellenberger, and R. Krishna, "Radial and axial dispersion of the liquid phase within a KATAPAK-S(R) structure: experiments vs. CFD simulations," *Chemical Engineering Science*, vol. 56, no. 3, pp. 813–821, 2001.

[9] J. M. van Baten and R. Krishna, "Gas and liquid phase mass transfer within KATAPAK-S structures studied using CFD simulations," *Chemical Engineering Science*, vol. 57, no. 9, pp. 1531–1536, 2002.

[10] C. F. Petre, F. Larachi, I. Iliuta, and B. P. A. Grandjean, "Pressure drop through structured packings: breakdown into the contributing mechanisms by CFD modeling," *Chemical Engineering Science*, vol. 58, no. 1, pp. 163–177, 2003.

[11] F. Larachi, C. F. Petre, I. Iliuta, and B. Grandjean, "Tailoring the pressure drop of structured packings through CFD simulations," *Chemical Engineering and Processing*, vol. 42, no. 7, pp. 535–541, 2003.

[12] B. Szulczewska, I. Zbicinski, and A. Górak, "Liquid flow on structured packing: CFD simulation and experimental study," *Chemical Engineering and Technology*, vol. 26, no. 5, pp. 580–584, 2003.

[13] L. Raynal, C. Boyer, and J. P. Ballaguet, "Liquid holdup and pressure drop determination in structured packing with CFD simulations," *Canadian Journal of Chemical Engineering*, vol. 82, no. 5, pp. 871–879, 2004.

[14] A. Ataki and H. J. Bart, "Experimental and CFD simulation study for the wetting of a structured packing element with liquids," *Chemical Engineering and Technology*, vol. 29, no. 3, pp. 336–347, 2006.

[15] M. Haghshenas Fard, M. Zivdar, R. Rahimi et al., "CFD simulation of mass transfer efficiency and pressure drop in a structured packed distillation column," *Chemical Engineering and Technology*, vol. 30, no. 7, pp. 854–861, 2007.

[16] B. Mahr and D. Mewes, "Two-phase flow in structured packings: modeling and calculation on a macroscopic scale," *AIChE Journal*, vol. 54, no. 3, pp. 614–626, 2008.

[17] M. R. Khosravi Nikou and M. R. Ehsani, "Turbulence models application on CFD simulation of hydrodynamics, heat and mass transfer in a structured packing," *International Communications in Heat and Mass Transfer*, vol. 35, no. 9, pp. 1211–1219, 2008.

[18] J. Fernandes, P. C. Simões, J. P. B. Mota, and E. Saatdjian, "Application of CFD in the study of supercritical fluid extraction with structured packing: dry pressure drop calculations," *Journal of Supercritical Fluids*, vol. 47, no. 1, pp. 17–24, 2008.

[19] J. Fernandes, P. F. Lisboa, P. C. Simões, J. P. B. Mota, and E. Saatdjian, "Application of CFD in the study of supercritical fluid extraction with structured packing: wet pressure drop calculations," *Journal of Supercritical Fluids*, vol. 50, no. 1, pp. 61–68, 2009.

[20] J. U. Brackbill, "A continuum method for modeling surface tension," *Journal of Computational Physics*, vol. 100, no. 2, pp. 335–354, 1992.

[21] A. Rafati Saleh, S. H. Hosseini, S. Shojaee, and G. Ahmadi, "CFD studies of pressure drop and increasing capacity in mellapakplus 752.Y structured packing," *Chemical Engineering & Technology*, vol. 34, pp. 1402–1412, 2011.

[22] J. A. Rocha, J. L. Bravo, and J. R. Fair, "Distillation columns containing structured packings: a comprehensive model for their performance. 1. Hydraulic models," *Industrial and Engineering Chemistry Research*, vol. 32, no. 4, pp. 641–651, 1993.

[23] S. Y. Cho, Y. Y. Lee, and S. J. Kim, "A study on characteristics of a modern structured packing," *Korean Journal of Chemical Engineering*, vol. 12, no. 3, pp. 313–319, 1995.

[24] I. Iliuta and F. Larachi, "Mechanistic model for structured-packing-containing columns: irrigated pressure drop, liquid holdup, and packing fractional wetted area," *Industrial and Engineering Chemistry Research*, vol. 40, no. 23, pp. 5140–5146, 2001.

[25] E. Brunazzi, G. Nardini, A. Paglianti, and L. Petarca, "Interfacial area of Mellapak packing: absorption of 1,1,1-trichloroethane by Genosorb 300," *Chemical Engineering & Technology*, vol. 18, no. 4, pp. 248–255, 1995.

[26] M. Henriques De Brito, U. Von Stockar, A. Menendez Bangerter, P. Bomio, and M. Laso, "Effective mass-transfer area in a pilot plant column equipped with structured packings and with ceramic rings," *Industrial & Engineering Chemistry Research*, vol. 33, no. 3, pp. 647–656, 1994.

[27] R. E. Tsai, A. F. Seibert, R. B. Eldridge, and G. T. Rochelle, "Influence of viscosity and surface tension on the effective mass transfer area of structured packing," *Energy Procedia*, vol. 1, pp. 1197–1204, 2009.

[28] S. Aferka, A. Viva, E. Brunazzi, P. Marchot, M. Crine, and D. Toye, "Tomographic measurement of liquid hold up and effective interfacial area distributions in a column packed with high performance structured packings," *Chemical Engineering Science*, vol. 66, no. 14, pp. 3413–3422, 2011.

[29] G. Q. Wang, X. G. Yuan, and K. T. Yu, "A method for calculating effective interfacial area of structured packed distillation columns under elevated pressures," *Chemical Engineering and Processing*, vol. 45, no. 8, pp. 691–697, 2006.

[30] J. R. Fair, A. F. Seibert, M. Behrens, P. P. Saraber, and Z. Olujic, "Structured packing performance—experimental evaluation of two predictive models," *Industrial and Engineering Chemistry Research*, vol. 39, no. 6, pp. 1788–1796, 2000.

Hindawi Publishing Corporation
Journal of Applied Mathematics
Volume 2012, Article ID 545120, 9 pages
doi:10.1155/2012/545120

Review Article

Numerical Simulation of Unsteady Compressible Flow in Convergent Channel: Pressure Spectral Analysis

Petra Pořízková,[1] Karel Kozel,[2] and Jaromír Horáček[2]

[1] *Department of Technical Mathematics, Faculty of Mechanical Engineering, Czech Technical University in Prague, Karlovo Nám. 13, 121 35 Praha 2, Czech Republic*
[2] *Institute of Thermomechanics AS CR, Dolejškova 5, 18200 Prague 8, Czech Republic*

Correspondence should be addressed to Petra Pořízková, puncocha@marian.fsik.cvut.cz

Received 16 January 2012; Accepted 8 March 2012

Academic Editor: Fu-Yun Zhao

This study deals with the numerical solution of a 2D unsteady flow of a compressible viscous fluid in a channel for low inlet airflow velocity. The unsteadiness of the flow is caused by a prescribed periodic motion of a part of the channel wall with large amplitudes, nearly closing the channel during oscillations. The flow is described by the system of Navier-Stokes equations for laminar flows. The numerical solution is implemented using the finite volume method (FVM) and the predictor-corrector Mac-Cormack scheme with Jameson artificial viscosity using a grid of quadrilateral cells. Due to the motion of the grid, the basic system of conservation laws is considered in the arbitrary Lagrangian-Eulerian (ALE) form. The numerical results of unsteady flows in the channel are presented for inlet Mach number $M_\infty = 0.012$, Reynolds number $\mathrm{Re}_\infty = 4481$, and the wall motion frequency 100 Hz.

1. Introduction

A current challenging question is a mathematical and physical description of the mechanism for transforming the airflow energy in human vocal tract (convergent channel) into the acoustic energy representing the voice source in humans. The voice source signal travels from the glottis to the mouth, exciting the acoustic supraglottal spaces, and becomes modified by acoustic resonance properties of the vocal tract [1]. The airflow coming from the lungs causes self-oscillations of the vocal folds, and the glottis completely closes in normal phonation regimes, generating acoustic pressure fluctuations. In this study, the movement of the boundary channel is known, harmonically opening and nearly closing in the narrowest cross-section of the channel, making the investigation of the airflow field in the glottal region possible.

Acoustic wave propagation in the vocal tract is usually modeled from incompressible flow models separately using linear acoustic perturbation theory, the wave equation for the potential flow [2], or the Lighthill approach on sound generated aerodynamically [3].

Goal of this work is numerical simulation of compressible viscous flow in 2D convergent channel which involves attributes of real flow causing acoustic perturbations as is "Coandă phenomenon" (the tendency of a fluid jet to be attracted to a nearby surface), vortex convection and diffusion, jet flapping, and so forth along with lower call on computer time, due to later extension in 3D channel flow. Particular attention is paid to the analysis of acoustic pressure signal from the channel.

2. Mathematical Model

To describe the unsteady laminar flow of a compressible viscous fluid in a channel, the 2D system of Navier-Stokes equations was considered as a mathematical model. The system of Navier-Stokes equations is expressed in nondimensional conservative form [4]

$$\frac{\partial \mathbf{W}}{\partial t} + \frac{\partial \mathbf{F}}{\partial x} + \frac{\partial \mathbf{G}}{\partial y} = \frac{1}{\mathrm{Re}}\left(\frac{\partial \mathbf{R}}{\partial x} + \frac{\partial \mathbf{S}}{\partial y}\right), \tag{2.1}$$

where $\mathbf{W} = [\rho, \rho u, \rho v, e]^T$ is the vector of conservative variables, $\mathbf{F}$ and $\mathbf{G}$ are the vectors of inviscid fluxes, and $\mathbf{R}$ and $\mathbf{S}$ are the vectors of viscous fluxes. The static pressure p is expressed by the state equation in the form

$$p = (\kappa - 1)\left[e - \frac{1}{2}\rho\left(u^2 + v^2\right)\right]. \tag{2.2}$$

The transformation to the nondimensional form uses inflow parameters (marked with the infinity subscript) as reference variables (dimensional variables are marked with the hat): the speed of sound $\hat{c}_\infty = 343\,\mathrm{ms}^{-1}$, density $\hat{\rho}_\infty = 1.225\,\mathrm{kg\,m}^{-3}$, reference length $\hat{L}_r = 0.02\,\mathrm{m}$, and dynamic viscosity $\hat{\eta}_\infty = 18 \cdot 10^{-6}\,\mathrm{Pa \cdot s}$. Inflow temperature $\hat{T}_\infty$ $[K]$ depends on relation for speed of sound $\hat{c}_\infty^2 = \kappa \hat{R} \hat{T}_\infty$ where $\kappa = 1.4$ is the ratio of the specific heats. Inflow pressure satisfies equation of state for ideal gas $\hat{p}_\infty = \hat{\rho}_\infty \hat{R} \hat{T}_\infty$.

General Reynolds number in (2.1) is computed from reference variables $\mathrm{Re} = \hat{\rho}_\infty \hat{c}_\infty \hat{L}_r / \hat{\eta}_\infty$. The nondimensional dynamic viscosity in the dissipative terms is a function of temperature in the form $\eta = (T/T_\infty)^{3/4}$. The heat transfer coefficient is expressed as $k = \eta\kappa/[\mathrm{Pr}(\kappa - 1)]$, where $\mathrm{Pr} = 0.7$ is the Prandtl number.

3. Computational Domain and Boundary Conditions

For phonation of vowels, the frequencies of the vocal folds oscillations are in the region from cc 82 Hz for bass up to cc 1170 Hz for soprano in singing voice, and the airflow velocity in the trachea is approximately in the range of 0.3–5.2 ms^{-1} taking into account the tracheal diameter in humans in the range 14.5–17.6 mm [2].

The bounded computational domain D_1, used for the numerical solution of flow field in the channel, is shown in Figure 1. The domain is a symmetric channel, the shape of which is

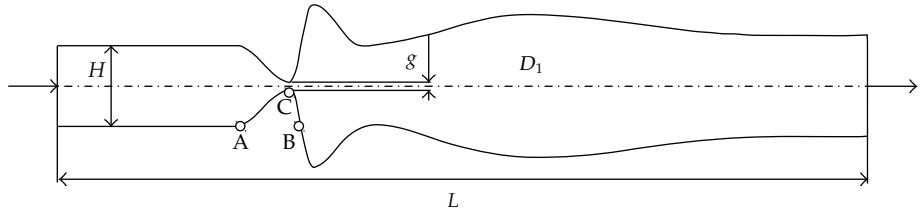

Figure 1: Computational domain D_1. $L = 8$ (160 mm), $H = 0.8$ (16 mm), and $g = 0.08$ (1.6 mm)—middle position.

inspired by the shape [5] of the trachea (inlet part of the channel), vocal folds, false vocal folds and supraglottal spaces (outlet part). The upper and the lower boundaries are the channel walls. A part of the wall changes its shape between the points A and B according to a given harmonic function of time and axial coordinate (see, e.g., [6]). The gap $g(t)$ is the narrowest part of the channel (in point C). The gap width was oscillating with frequency 100 Hz (typical for normal male voice) between the minimum $g_{\min} = 0.4$ mm and maximum $g_{\max} = 2.8$ mm, not closing the channel completely.

The boundary conditions are considered in the following formulation:

(1) upstream conditions: $u_\infty = \widehat{u}_\infty/\widehat{c}_\infty = M_\infty$, $v_\infty = 0$, $\rho_\infty = 1$, and p_∞ is extrapolated from domain D_1;

(2) downstream conditions: $p_2 = 1/\kappa$ and $(\rho, \rho u, \rho v)$ are extrapolated from D_1;

(3) flow on the wall: $(u, v) = (u_{\text{wall}}, v_{\text{wall}})$ where $(u_{\text{wall}}, v_{\text{wall}})$ is velocity vector of the wall and $\partial T/\partial \vec{n} = 0$ where $T = \kappa p/\rho$ is the temperature.

The general Reynolds number in (2.1) multiplied with nondimensional value $M_\infty H$ represents kinematic viscosity scale, and for computation of the real problem, inlet Reynolds number $\text{Re}_\infty = \widehat{\rho}_\infty \widehat{c}_\infty M_\infty H \widehat{L}_r/\widehat{\eta}_\infty$ is used.

4. Numerical Solution

The numerical solution uses FVM in conservative cell-centered form on the grid of quadrilateral cells, see, for example, [4].

The bounded domain is divided into mutually disjoint subdomains $D_{i,j}$ (i.e., quadrilateral cells). The system of (2.1) is integrated over the subdomains $D_{i,j}$ using the Green formula and the mean value theorem. In the time-changing domain, the integral form of FVM is derived using the ALE formulation. The ALE method defines homeomorphic mapping of the reference domain $D_{t=0}$ at initial time $t = 0$ to a domain D_t at $t > 0$ [7].

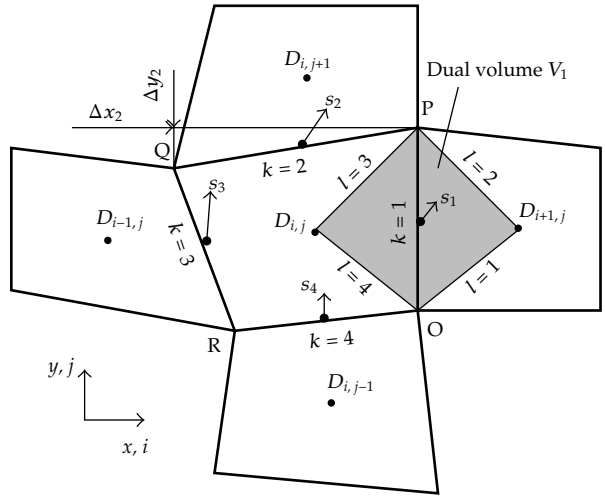

Figure 2: Finite volume $D_{i,j}$ and dual volume V'_k.

The explicit predictor-corrector MacCormack (MC) scheme in the domain with a moving grid of quadrilateral cells is used. The scheme is 2nd order accurate in time and space using orthogonal regular grid [4]

$$\mathbf{W}_{i,j}^{n+1/2} = \frac{\mu_{i,j}^{n}}{\mu_{i,j}^{n+1}}\mathbf{W}_{i,j}^{n} - \frac{\Delta t}{\mu_{i,j}^{n+1}}\sum_{k=1}^{4}\left[\left(\tilde{\mathbf{F}}_k^n - s_{1k}\mathbf{W}_k^n - \frac{1}{\mathrm{Re}}\tilde{\mathbf{R}}_k^n\right)\Delta y_k - \left(\tilde{\mathbf{G}}_k^n - s_{2k}\mathbf{W}_k^n - \frac{1}{\mathrm{Re}}\tilde{\mathbf{S}}_k^n\right)\Delta x_k\right],$$

$$\overline{\mathbf{W}}_{i,j}^{n+1} = \frac{\mu_{i,j}^{n}}{\mu_{i,j}^{n+1}}\frac{1}{2}\left(\mathbf{W}_{i,j}^{n} + \mathbf{W}_{i,j}^{n+1/2}\right) - \frac{\Delta t}{2\mu_{i,j}^{n+1}}\sum_{k=1}^{4}\left[\left(\tilde{\mathbf{F}}_k^{n+1/2} - s_{1k}\mathbf{W}_k^{n+1/2} - \frac{1}{\mathrm{Re}}\tilde{\mathbf{R}}_k^{n+1/2}\right)\Delta y_k - \left(\tilde{\mathbf{G}}_k^{n+1/2} - s_{2k}\mathbf{W}_k^{n+1/2} - \frac{1}{\mathrm{Re}}\tilde{\mathbf{S}}_k^{n+1/2}\right)\Delta x_k\right], \tag{4.1}$$

where $\Delta t = t^{n+1} - t^n$ is the time step, $\mu_{i,j} = \int\int_{D_{i,j}} dx\,dy$ is the volume of cell $D_{i,j}$, Δx and Δy are the steps of the grid in directions x and y, and vector $\mathbf{s}_k = (s_1, s_2)_k$ represents the speed of edge k (see Figure 2). The physical fluxes $\mathbf{F}$, $\mathbf{G}$, $\mathbf{R}$, $\mathbf{S}$ on the edge k of the cell $D_{i,j}$ are replaced by numerical fluxes (marked with tilde) $\tilde{\mathbf{F}}$, $\tilde{\mathbf{G}}$, $\tilde{\mathbf{R}}$, $\tilde{\mathbf{S}}$ as approximations of the physical fluxes.

The approximations of the convective terms $\mathbf{sW}_k$ and the numerical viscous fluxes $\tilde{\mathbf{R}}_k, \tilde{\mathbf{S}}_k$ on the edge k are central. The higher partial derivatives of velocity and temperature in $\tilde{\mathbf{R}}_k, \tilde{\mathbf{S}}_k$ are approximated using dual volumes V'_k (see [4]) shown in Figure 2. The inviscid numerical fluxes are approximated by the physical fluxes from the cell on the left side of the current edge in the predictor step and from the cell on the right side of the current edge in the corrector step.

The last term used in the MC scheme is the Jameson artificial dissipation $\mathrm{AD}(W_{i,j})^n$ [8]. Artificial dissipation is used to stabilize computation and also due to velocity gradients in the narrowest width of the channel, where $M_\infty \approx 0.5$. The vector of conservative variables is computed at a new time level t^{n+1}: $\mathbf{W}_{i,j}^{n+1} = \overline{\mathbf{W}}_{i,j}^{n+1} + \mathrm{AD}(W_{i,j})^n$.

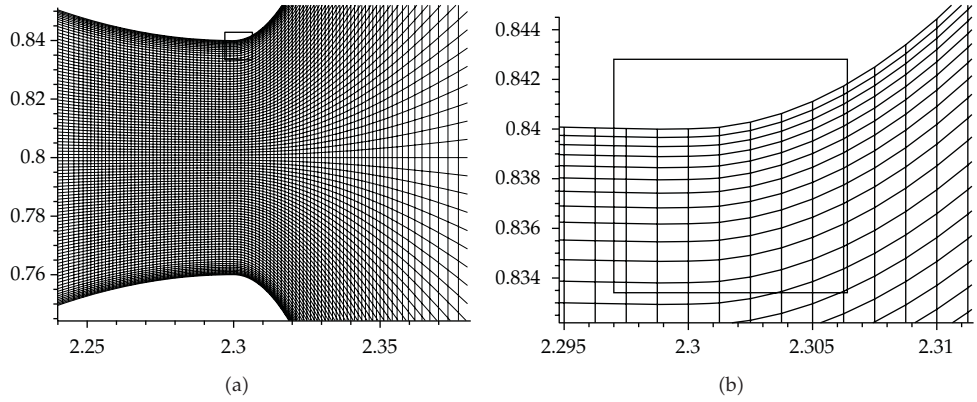

Figure 3: Grid of quadrilateral cells in the narrowest part of domain D_1 at the middle position of the gap width $g = 0.08$ (1.6 mm). Detail: $\Delta y_{\min} \doteq 5 \cdot 10^{-4}$ (0.01 mm).

The stability condition of the scheme (on the regular orthogonal grid) limits the time step

$$\Delta t \leq \mathrm{CFL}\left(\frac{|u_{\max}| + c}{\Delta x_{\min}} + \frac{|v_{\max}| + c}{\Delta y_{\min}} + \frac{2}{\mathrm{Re}}\left(\frac{1}{\Delta x_{\min}^2} + \frac{1}{\Delta y_{\min}^2}\right)\right)^{-1}, \tag{4.2}$$

where c denotes the local speed of sound, $u_{\max}$ and $v_{\max}$ are the maximum velocities in the domain, and CFL < 1 for nonlinear equations [9]. Time discretization of the scheme satisfies discrete geometric conservation law (DGCL), see [10].

The grid used in the channel has successive refinement cells near the wall. The minimum cell size in y-direction is $\Delta y_{\min} \approx 1/\sqrt{\mathrm{Re}_\infty}$ to capture the boundary layer effects. Figure 3 shows the detail of the grid in domain D_1 in the narrowest channel cross-section at the middle position of the gap.

5. Numerical Results

The numerical results were obtained (using a specifically developed program) for the following input data: Mach number $M_\infty = 0.012$ ($\widehat{u}_\infty = 4.116\,\mathrm{ms}^{-1}$), Reynolds number $\mathrm{Re}_\infty = 4481$, atmospheric pressure $p_2 = 1/\kappa$ ($\widehat{p}_2 = 102942\,Pa$) at the outlet, and wall oscillation frequency $\widehat{f} = 100\,\mathrm{Hz}$. The computational domain contained 450×100 cells in D_1.

The computation has been carried out in two stages. First, a steady numerical solution is obtained, when the channel between points A and B has a rigid wall fixed in the middle position of the gap width. Then this solution is used as the initial condition for the unsteady simulation.

Figure 4 shows the initial condition for unsteady computation of the flow field in domain D_1 and the convergence to the steady-state solution computed using the L_2 norm of momentum residuals (ρu). The maximum Mach number computed in the flow field Figure 4(a) was $M_{\max} = 0.177$ (corresponding to the dimension velocity $\widehat{u}_{\max} = 60.7\,\mathrm{ms}^{-1}$). The picture displays nonsymmetric flow developed behind the narrowest channel cross-section. The graph in Figure 4(b) indicates the nonstationary solution of initial condition

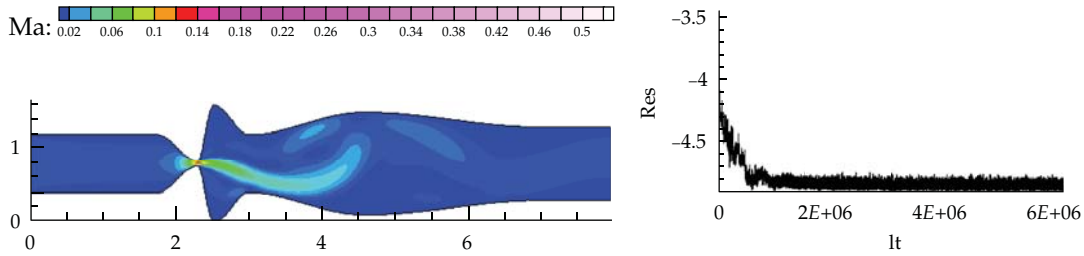

(a) The velocity flow field mapped by isolines of Mach number

(b) Convergence to the steady-state solution using L_2 norm of momentum residuals (ρu)

Figure 4: The initial condition computed in D_1—$M_\infty = 0.012$, $\mathrm{Re}_\infty = 4481$, $p_2 = 1/\kappa$, 450×100 cells, and $M_{\max} = 0.177$ ($\widehat{u}_{\max} = 60.7\,\mathrm{ms}^{-1}$).

which is caused probably by eddies separated in the unmovable glottal orifice and floating away.

The numerical simulation of the airflow computed in domain D_1 over the fourth cycle of the wall oscillation is presented in Figure 5 showing the unsteady flow field in five time instants during one vibration period. Large eddies are developing in supraglottal spaces and a "Coandă" effect is apparent in the flow field pattern. The absolute maximum of Mach number $M_{\max} = 0.535$ ($\widehat{u}_{\max} = 183.5\,\mathrm{ms}^{-1}$) in the flow field during fourth cycle was achieved at time $t = 34.2\,\mathrm{ms}$ ($g = 1.002\,\mathrm{mm}$, opening phase) behind the narrowest channel cross-section. The flow becomes practically periodic after the first period of oscillations.

Figure 6 shows three vibration periods of the gap width oscillation (a) and the acoustic pressures signals computed in the gap (b) and at the outlet (c) on the axis of the channel. The acoustic pressure was calculated by subtracting the average values of the pressure signals $p_{\mathrm{ac}} = p - p_2$. The acoustic pressure time dependent data are transformed to frequency-dependent data (acoustic pressure spectrum) using discrete fourier transformation (DFT) of the signals. The spectrum of the pressure in the glottis, Figure 6(b)-right, shows the dominant fundamental frequency of vocal folds model oscillations $\widehat{f}_0 = 100\,\mathrm{Hz}$ and the generated higher harmonics as a consequence of the throttling and nearly closing the glottal gap $g(t)$. Two different regimes are apparent in the acoustic pressure signal at the channel outlet during one vibration period of the glottis in Figure 6(c)-left. Relatively smooth signal containing low frequencies is dominant in the time interval corresponding to the phase of maximum glottal opening, and a very noisy signal containing high frequencies is associated with the phase of minimum glottal opening. Four acoustic resonances of the channel cavity at about $\widehat{f}_0 = 100$, $\widehat{f}_1 = 550$, $\widehat{f}_2 = 1150$, and $\widehat{f}_3 = 1950\,\mathrm{Hz}$ can be identified in the spectrum envelope of the pressure at the channel outlet in Figure 6(c)-right. The first acoustic resonance $\widehat{f}_1 = 550\,\mathrm{Hz}$ (see spectrum peak at cc 500 Hz) corresponds to the first eigenfrequency $\widehat{F}_1$ of a simple tube of the length of the complete channel closed at the inlet and open at the outlet ($\widehat{F}_1 = \widehat{c}_\infty/(4L \cdot \widehat{L}_r) = 343\,\mathrm{ms}^{-1}/(4 \cdot 0.16\,\mathrm{m}) = 536\,\mathrm{Hz}$). The acoustic resonances are more damped with increasing frequency, which can be caused by the fluid viscosity as well as by a numerical viscosity implemented in the numerical method (constants magnitude in $\mathrm{AD}(W_{i,j})^n$).

Remark 5.1. We used several tests on fine and coarse grids in the computational domain. Also the domain has been prolonged in upstream and also in downstream part. Achieved results were approximately the same on fine grid.

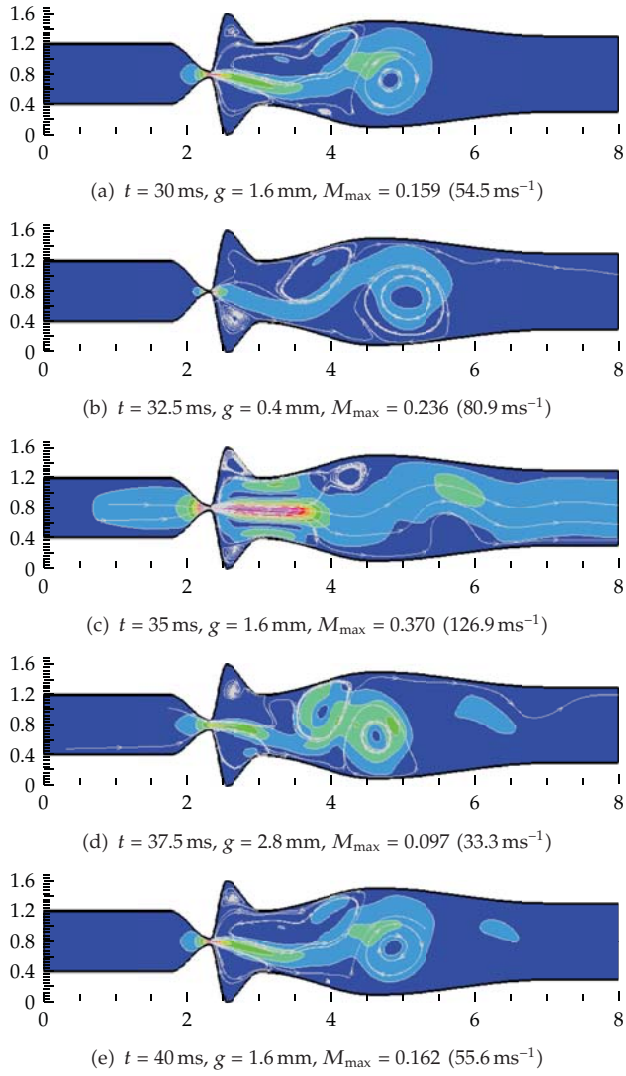

(a) $t = 30\,\text{ms}$, $g = 1.6\,\text{mm}$, $M_{\max} = 0.159$ $(54.5\,\text{ms}^{-1})$

(b) $t = 32.5\,\text{ms}$, $g = 0.4\,\text{mm}$, $M_{\max} = 0.236$ $(80.9\,\text{ms}^{-1})$

(c) $t = 35\,\text{ms}$, $g = 1.6\,\text{mm}$, $M_{\max} = 0.370$ $(126.9\,\text{ms}^{-1})$

(d) $t = 37.5\,\text{ms}$, $g = 2.8\,\text{mm}$, $M_{\max} = 0.097$ $(33.3\,\text{ms}^{-1})$

(e) $t = 40\,\text{ms}$, $g = 1.6\,\text{mm}$, $M_{\max} = 0.162$ $(55.6\,\text{ms}^{-1})$

Figure 5: The unsteady numerical solution of the airflow in D_1— $\hat{f} = 100\,\text{Hz}$, $M_\infty = 0.012$, $\text{Re}_\infty = 4481$, $p_2 = 1/\kappa$, and 450×100 cells. Data computed during the fourth oscillation cycle. Results are mapped by isolines of velocity ratio and by streamlines.

Remark 5.2. The mathematical model (2.1) of laminar flow used in this case is debatable. For the first approximation, we supposed unformed turbulent flow at the inlet part of the channel.

Remark 5.3. The validation of computations for this case is not complete because of experiments absence. Semivalidation of the computations is comparison with particle image velocimetry method (PIV) experiment, but we can compare only qualitative behavior of the flow. Full validation of the code for subsonic and transonic flow through a turbine cascade computed in periodic domain is showed, for example, in [10].

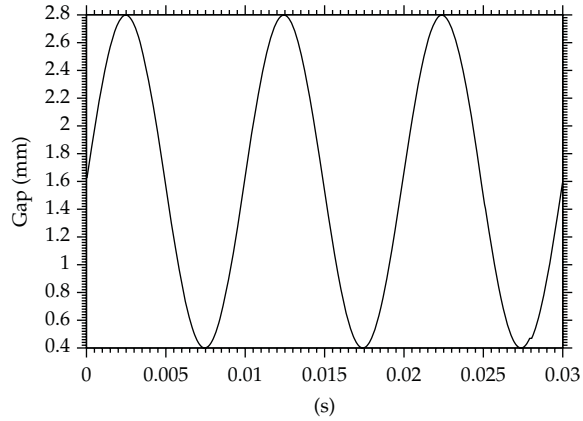

(a) The prescribed oscillation of gap width $\hat{f}$ = 100 Hz.

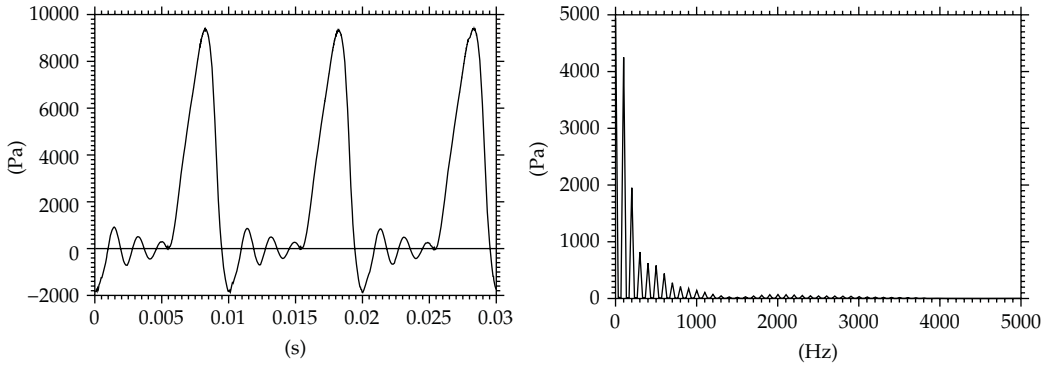

(b) The acoustic pressure in the gap and DFT spectrum—$\hat{f}_0$ = 100 Hz.

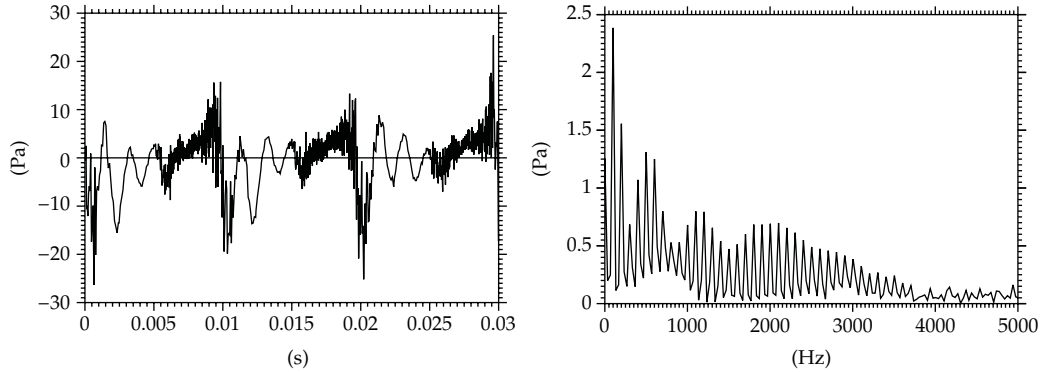

(c) The acoustic pressure at the outlet and DFT spectrum—$\hat{f}_0$ = 100, $\hat{f}_1$ = 550, $\hat{f}_2$ = 1150, $\hat{f}_3$ = 1950 Hz.

Figure 6: Three vibration periods of the gap width oscillations and the acoustic pressure signals p_{ac} computed in the gap and at the outlet on the axis of the channel.

6. Discussion and Conclusions

The numerical solution in the channel showed large vortex structures developed in the supraglottal space moving slowly downstream and decaying gradually. It was possible to detect a "Coandă phenomenon" in the computed flow field patterns. A similar generation of large-scale vortices, vortex convection and diffusion, jet flapping, and general flow patterns

were experimentally obtained in physical models of the vocal folds by using PIV method in [5, 11, 12].

The results show that some numerical results of viscous flow in a symmetric channel using a symmetric grid and scheme can be nonsymmetrical, depending on the geometry and the Reynolds number. This effect was observed also for laminar transonic flow computation [13]. The assumption of the axisymmetry solution for the axisymmetry channels (see [6]) excludes modeling the "Coandă" effect and large vortex structures of the size comparable with the cross-section of the channel.

The analysis of the computed pressure revealed basic acoustic characteristics of the channel. This is promising result for future studies for a direct modeling of human voice generated by the flow in vibrating glottis taken into account a real shape of the human vocal tract for phonation and throttling the glottal gap width up to zero.

Acknowledgment

This paper was partially supported by Research Plans MSM 6840770010, GAČR P101/11/0207 and 201/08/0012.

References

[1] I. R. Titze, *Principles of Voice Production*, National Centre for Voice and Speech, Iowa City, IA, Iowa, USA, 2000.

[2] I. R. Titze, *The Myoelastic Aerodynamic Theory of Phonation*, National Centre for Voice and Speech, Iowa City, IA, Iowa, USA, 2006.

[3] S. Zorner, M. Kalteenbacher, W. Mattheus, and C. Brucker, "Human phonation analysis by 3d aeroacoustic computation," in *Proceedings of the International Conference on Acoustic NAG/DAGA 2009*, pp. 1730–1732, Rotterdam, The Netherlands, 2009.

[4] J. Fürst, M. Janda, and K. Kozel, "Finite volume solution of 2D and 3D Euler and Navier-Stokes equations," in *Mathematical Fluid Mechanics*, pp. 173–194, Birkhäuser, Basel, Switzerland, 2001.

[5] J. Horacek, P. Sidlof, V. Uruba, J. Vesely, V. Radolf, and V. Bula, "PIV measurement of flow-patterns in human vocal tract model," in *Proceedings of the the International Conference on Acoustic NAG/DAGA 2009*, pp. 1737–1740, Rotterdam, The Netherlands, 2009.

[6] P. Punčochářová-Pořízková, J. Fürst, J. Horáček, and K. Kozel, "Numerical solutions of unsteady flows with low inlet Mach numbers," *Mathematics and Computers in Simulation*, vol. 80, no. 8, pp. 1795–1805, 2010.

[7] R. Honzatko, J. Horacek, and K. Kozel, *Solution of Inviscid Incompressible Flow Over a Vibrating Profile*, vol. 3 of *COE Lecture Notes*, Kyushu university, 2006, Edited by M. Benes, M. Kimura and T. Nataki.

[8] A. Jameson, W. Schmidt, and E. Turkel, "Numerical solution of the Euler equations by the finite volume methods using Runge-Kutta time-stepping schemes," *AIAA*, pp. 81–125, 1981.

[9] R. Dvorak and K. Kozel, *Mathematical Modeling in Aerodynamics*, Prague, Czech Republic, 1996, (In Czech).

[10] P. Porizkova, *Numerical solution of compressible flows using finite volume method*, Ph.D. thesis, Czech Technical University in Prague, Faculty of Mechanical Engineering, Prague, Czech Republic, 2009.

[11] P. Sidlof, *Fluid-structure interaction in human vocal folds*, Ph.D. thesis, Charles University in Prague, Faculty of Mathematics and Physics, Prague, Czech Republic, 2007.

[12] J. Neubauer, Z. Zhang, R. Miraghaie, and D. Berry, "Coherent structures of the near field flow in self-oscillating physical model of the vocal folds," *Journal of the Acoustical Society of America*, vol. 121, no. 2, pp. 1102–1118, 2007.

[13] J. Fort, T. Hulek, K. Kozel, and M. Vavrincova, *Remark on Numerical Simulation of 2D Unsteady Transonic Flows*, vol. 414 of *Lecture Notes in Physics*, Springer, Berlin, Germany, 1993, Edited by M. Napolitano and F. Sabetta.

Hindawi Publishing Corporation
Journal of Applied Mathematics
Volume 2012, Article ID 534783, 14 pages
doi:10.1155/2012/534783

Research Article

Comparative Performance of Surrogate-Assisted MOEAs for Geometrical Design of Pin-Fin Heat Sinks

Siwadol Kanyakam[1] and Sujin Bureerat[2]

[1] *Department of Engineering Management, Faculty of Science and Technology, Rajabhat Maha Sarakham University, Maha Sarakham 44000, Thailand*
[2] *Department of Mechanical Engineering, Faculty of Engineering, Khon Kaen University, Khon Kaen 40002, Thailand*

Correspondence should be addressed to Sujin Bureerat, sujbur@kku.ac.th

Received 16 January 2012; Revised 21 February 2012; Accepted 6 March 2012

Academic Editor: Hung Lam (Steve) Yim

This paper presents the comparative performance of several surrogate-assisted multiobjective evolutionary algorithms (MOEAs) for geometrical design of a pin-fin heat sink (PFHS). The surrogate-assisted MOEAs are achieved by integrating multiobjective population-based incremental learning (PBIL) with a quadratic response surface model (QRS), a radial-basis function (RBF) interpolation technique, and a Kriging (KRG) or Gaussian process model. The mixed integer/continuous multiobjective design problem of PFHS with the objective to minimise junction temperature and fan pumping power simultaneously is posed. The optimum results obtained from using the original multiobjective PBIL and the three versions of hybrid PBIL are compared. It is shown that the hybrid PBIL using KRG is the best performer. The hybrid PBILs require less number of function evaluations to surpass the original PBIL.

1. Introduction

An air-cooled heat sink is one of the most effective and popular cooling devices for electronic packages due to its high reliability, simplicity, safety, and low cost. It is operated in such a way that the heat sink is attached to a device that needs to be cooled down such as a central processing unit (CPU) chip. Then, heat dissipation is achieved by using a fan to generate air flow through the heat sink. As a result, design of such a cooling device needs to find an optimum geometry such that cooling performance is optimised. The minimisation of the temperature between the heat sink base and the electronic device, which is called junction temperature, is one of the most used design objectives for maximising thermal performance

[1–5]. Nevertheless, in heat transfer design, increasing thermal performance usually results in an increase of pressure drop across the cooling device. This requires high pumping power and consequently high operating cost. Therefore, a design process of a heat sink usually has two design objectives that are junction temperature and fan pumping power for this study.

The use of multiobjective optimisers for geometrical and sizing design of heat sinks has been investigated in recent years. Our previous work shows that using MOEAs for multiobjective design of pin-fin and plate-fin heat sinks is superior to a classical design approach [1–5]. Other work related to numerical simulation and optimum design of some types of pin-fin heat sinks can be found in [6–12]. Nevertheless, it is also found that the optimisation process is time-consuming due to expensive function evaluations from performing finite volume analysis (FVA); therefore, the performance enhancement of the MOEA design process is always required. The use of a radial-basis function response surface model (RSM) in combination with a strength Pareto evolutionary algorithm for plate-fin heat sink design has been studied [1]. It was found that, with the inclusion of the RBF surrogate model in the evolutionary design process, the performance of SPEA is greatly increased. In cases of pin-fin heat sink design, investigation on the use of integrated Kriging model and PBIL for solving a heat sink design problem has been made [5]. It is found that the hybrid optimiser performance is acceptable.

This work is aimed at performance enhancement of a multiobjective evolutionary optimiser by incorporating evolutionary search with a number of surrogate models. Although it is well known in the past that using a surrogate model can improve search performance of MOEAs, the performance test of several surrogate models for a particular design case still needs to be studied since the nature of design problems can affect surrogate model prediction performance. The design problem is posed to find geometrical parameters of a PFHS to minimise its junction temperature and fan pumping power. The population-based incremental learning is chosen as the optimiser since it gives the best results as shown in [2, 4]. The design process has been refined from the work presented in [5]. Surrogate models employed with PBIL are a Kriging method or Gaussian process model [13], a radial-basis function [1], and a quadratic response surface model. The comparative results show that the performance of a surrogate-assisted PBIL is superior to the nonsurrogate PBIL although the former uses lower number of function evaluations. The best surrogate model for this type of design problem is KRG.

2. Surrogate-Assisted PBIL

A particular multiobjective optimisation problem can be expressed as follows.

$$\begin{aligned} &\text{Minimise} \quad \mathbf{f} = \{f_1(x), \ldots, f_k(\mathbf{x})\} \\ &\text{subject to} \quad g_i(\mathbf{x}) \leq 0, \end{aligned} \tag{2.1}$$

where $\mathbf{x} \in [\mathbf{x}_l, \mathbf{x}_u]$ is a vector of n design variables and $g_i(\mathbf{x})$ are design inequality constraints. $k \geq 2$ objective functions $f_i(x)$ are intended to be minimised simultaneously. Figure 1 shows an arbitrary biobjective minimisation problem. The set of feasible design solutions are plotted in the objective domain (f_1 and f_2 coordinates). The optimum points are located on the front as shown. This is called a nondominated or Pareto front of the design problem where the members of the Pareto front are said to be equally good in optimisation point of view.

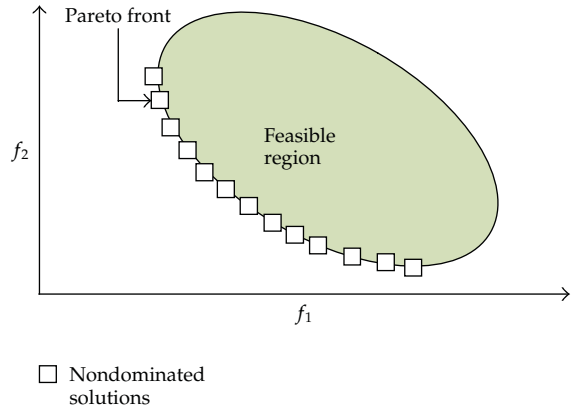

Figure 1: Pareto optimal set.

PBIL is an evolutionary optimiser based upon binary search space proposed by Baluja [14] in 1994, whereas it is extended for multiobjective cases by Bureerat and Sriworamas [15]. For single objective case, the PBIL search procedure starts with an initial probability vector (P_i) in which each element in the vector determines the probability of having "1" on each column of a binary population given that each row in the population is one design solution. The samples of a probability vector are shown in Table 2. It is shown that one probability vector can result in a variety of populations, and this feature of PBIL leads to impressive population diversity reproduction in a multiobjective optimisation design process [15].

Having obtained a probability vector from the binary population, the best binary design solution is then used to modify the probability vector using the following relation:

$$P_i^{\text{new}} = P_i^{\text{old}}(1 - L_R) + b_i L_R, \tag{2.2}$$

where b_i is the element of the best binary solution and L_R is learning rate which, in this work, is defined as

$$L_R = 0.5 + \text{rand} \cdot (+0.1 \text{ or } -0.1), \tag{2.3}$$

where rand $\in [0, 1]$ is a uniform random number.

For the multiobjective version of PBIL, a set of probability vectors, in which they are called a probability matrix, are used instead of only one vector so as to produce a more diverse binary population. The search procedure starts with an initial probability matrix, and a Pareto archive for collecting nondominated solutions. A binary population can then be obtained from the union set of sub-populations created from each row of the probability matrix. The nondominated solutions are obtained by sorting the combination of the nondominated solutions from the previous generation and the members in the current population. In case that the number of nondominated solutions exceeds the predefined archive size, a normal line method [2] is employed to remove some solutions from the Pareto archive. The process is repeated until a stopping criterion is fulfilled. More details of multiobjective PBIL can be seen in [2, 15].

In this work, the hybridisation of PBIL and a surrogate model is carried out in such a way that training design points and their corresponding objective values are generated using a Latin hypercube sampling (LHS) technique. Then, a surrogate model (KRG, QRS, or RBF) is built. The PBIL is used to find the nondominated front of the design problem where function evaluations are based upon a surrogate model predictor. Afterwards, a few design solutions in the nondominated front are selected by means of a clustering technique [16], whereas their actual function evaluations are performed. The selected binary solutions are set as an initial population, and they are used to generate the PBIL probability matrix. Then, the usual PBIL procedure is activated for a few iterations to improve the nondominated front. From the hybrid strategy, it is expected that the number of function evaluations is lower than that used by a nonsurrogate PBIL. The computational procedure can be separated into three phases and detailed as follows.

Phase I: Initialisation

(1) Generate training points using a Latin hypercube technique.

(2) Perform actual function evaluation.

(3) Construct a surrogate model (KRG, QRS, or RBF).

Phase II: Optimisation using a surrogate model

(1) Generate an initial probability matrix $P_{ij} = 0.5$ and a Pareto archive $A = \{\}$.

(2) If a termination condition is satisfied, stop. Otherwise, go to step 3.

(3) Generate a binary population B according to P_{ij}.

(4) Function evaluation based on surrogate prediction.

(5) Find nondominated solutions of $A \cup B$, and replace A with those solutions.

(6) If A is too large, remove some of its members using a normal line technique.

(7) Use members in A to update P_{ij} using (2.2) where L_R is computed using (2.3).

(8) Go to 2.

Phase III: Optimisation by actual function evaluations

(1) Select some members from A in the previous phase using a clustering technique, and find their actual function values.

(2) Generate an initial probability matrix $P_{ij} = 0.5$ and a Pareto archive A from sorting the design solution in step 1 of phase III.

(3) Update P_{ij} using members in A.

(4) If a termination condition is satisfied, stop. Otherwise, go to step 5.

(5) Generate a binary population B according to P_{ij}.

(6) Actual function evaluation based on finite volume analysis.

(7) Find nondominated solutions of $A \cup B$, and replace A with those solutions.

(8) If A is too large, remove some of its members using a normal line technique.

(9) Use members in A to update P_{ij} using (2.2) where L_R is computed using (2.3).

(10) Go to 4.

3. Surrogate Models

Let $y = f(\mathbf{x})$ be a function of a design vector $\mathbf{x}$ sized $n \times 1$. Given a set of design solutions (or sampling points) $\mathbf{X} = [\mathbf{x}^1, \ldots, \mathbf{x}^N]$ generated by using the Latin hypercute technique and their corresponding function values $\mathbf{Y} = [y_1, \ldots, y_N]$, a surrogate or approximation model is constructed by means of curve fitting or interpolation. Approximation models used in this study are as follows.

3.1. Quadratic Response Surface Model

The most commonly used polynomial surrogate model or a response surface model is of the second-order polynomial or quadratic model, which can be expressed as

$$\overline{y} = \beta_0 + \sum \beta_i x_i + \sum \beta_i x_i x_j, \tag{3.1}$$

where β_i for $i = 0, \ldots, (n+1)(n+2)/2$ are the polynomial coefficients to be determined. The coefficients can be found by using a regression or least square technique.

3.2. Kriging Model

A Kriging model (also known as a Gaussian process model) used in this paper is the famous MATLAB toolbox named design and analysis of computer experiments (DACEs) [13]. The estimation of function can be thought of as the combination of global and local approximation models that is

$$y(\mathbf{x}) = \overline{f}(\mathbf{x}) + Z(\mathbf{x}), \tag{3.2}$$

where $\overline{f}(\mathbf{x})$ is a global regression model while $Z(\mathbf{x})$ is a stochastic Gaussian process with zero mean and nonzero covariance representing a localised deviation. In this work, a linear function is used for a global model, which can be expressed as

$$\overline{f} = \beta_0 + \sum_{i=1}^{n} \beta_i x_i = \boldsymbol{\beta}^T \mathbf{f}, \tag{3.3}$$

where $\boldsymbol{\beta} = [\beta_0, \ldots, \beta_n]^T$, $\mathbf{f} = \mathbf{f}(\mathbf{x}) = [1, x_1, x_2, \ldots, x_n]^T$. The covariance of $Z(\mathbf{x})$ is expressed as

$$\mathrm{Cov}(Z(\mathbf{x}^p), Z(\mathbf{x}^q)) = \sigma^2 \mathbf{R}[R(\mathbf{x}^p, \mathbf{x}^q)] \tag{3.4}$$

for $p, q = 1, \ldots, N$, where R is the correlation function between any two of the N design points and $\mathbf{R}$ is the symmetric correlation matrix size $N \times N$ with the unity diagonal [17]. The correlation function used herein is

$$R(\mathbf{x}^p, \mathbf{x}^q) = \exp\left(-(\mathbf{x}^p - \mathbf{x}^q)^T \boldsymbol{\theta} (\mathbf{x}^p - \mathbf{x}^q)\right), \tag{3.5}$$

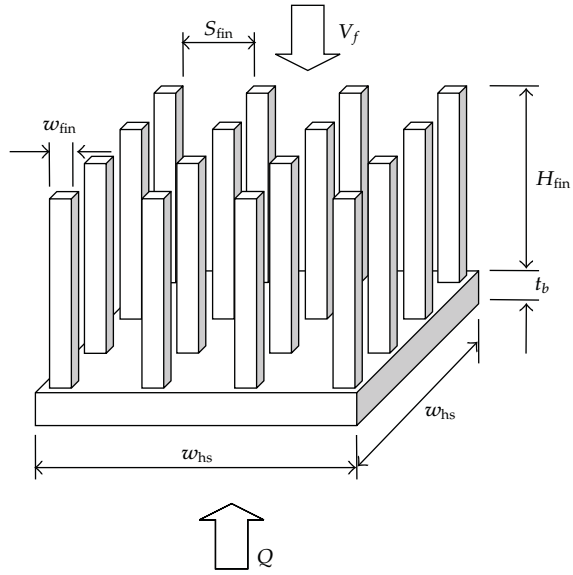

Figure 2: Physical model of pin-fin heat sink.

where θ_i are the unknown correlation parameters to be determined by means of the maximum likelihood method. Having found $\boldsymbol{\beta}$ and $\boldsymbol{\theta}$, the Kriging predictor can be achieved as

$$\overline{y}(\mathbf{x}) = \mathbf{f}(\mathbf{x})^T\boldsymbol{\beta} + \mathbf{r}^T(\mathbf{x})\mathbf{R}^{-1}(\mathbf{y} - \mathbf{F}\boldsymbol{\beta}), \tag{3.6}$$

where $\mathbf{F} = [\mathbf{f}(\mathbf{x}^1), \mathbf{f}(\mathbf{x}^2), \ldots, \mathbf{f}(\mathbf{x}^n)]^T$ and $\mathbf{r}^T(\mathbf{x}) = [R(\mathbf{x}, \mathbf{x}^1), R(\mathbf{x}, \mathbf{x}^2), \ldots, R(\mathbf{x}, \mathbf{x}^N)]$. For more details, see [13].

3.3. Redial-Basis Function Interpolation

The redial-basis function interpolation has been used in a wide range of applications such as integration between aerodynamic and finite element grids in aeroelastic analysis [18]. The use of such a model for surrogate-assisted evolutionary optimisation is said to be commonplace [1, 19, 20]. The approximate function can be written as

$$\overline{y}(\mathbf{x}) = \sum_{i=1}^{N} \alpha_i K\left(\left\|\mathbf{x} - \mathbf{x}^i\right\|\right), \tag{3.7}$$

where α_i are the coefficients to be determined and K is a radial-basis kernel (here it is set to be linear splines). The coefficients can be found from the N sampling points as detailed in [1].

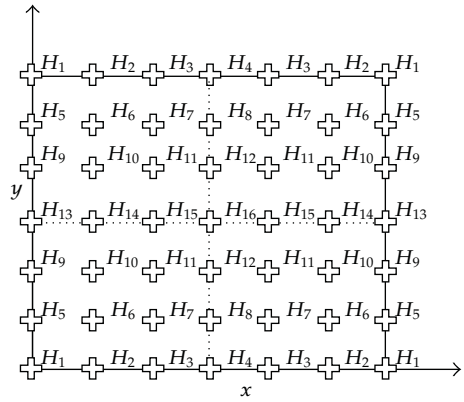

Figure 3: Fin height distribution control points.

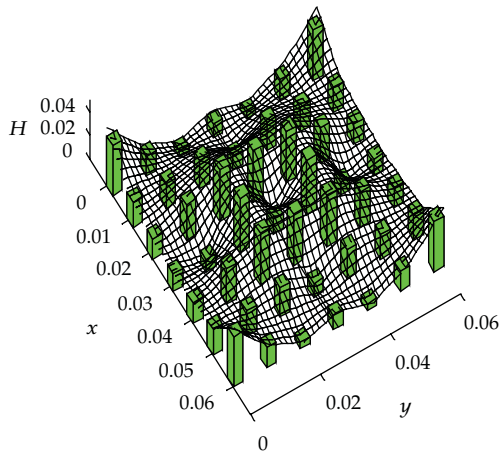

Figure 4: Fin heights distribution.

4. PFHS Design

A pin-fin heat sink herein is an air-cooled heat sink with square heat sink base and square pin fins as shown in Figure 2. Heat dissipation is accomplished by using a fan to generate air flow at the top of the heat sink. A PFHS physical model with square base (w_{hs}) is given in Figure 2. Parameters defining a heat sink geometry include base length (w_{hs}), base thickness t_b, fin width (w_{fin}), and number of fins n_f. The fins heights are varied based on the 16 input parameters (H_1–H_{16}). Figure 3 displays 7×7 control points on the fin base where the 16 fin height parameters are distributed symmetrically. The fin height can be determined by using radial-basis function interpolation. Figure 4 displays a sample of fin height distribution by using a RBF interpolation [3]. A fin-to-fin space or fin stitch (s_{fin}) is equispaced. The heat sink is cooled by a fan of V_f air velocity (m/s) which is installed on the top of a heat sink. A uniform heat load (Q) generated at the junction of heat sink, and an electronic device is set to be 120 watt. Materials and air properties and the assumptions of heat-flow in this simulation are detailed in [1, 2].

In the design process, an automated procedure is achieved by interfacing the CFD software into MATLAB. The design variables include those parameters for creating PFHS geometry and the inlet air velocity. For more details of the encoding/decoding process of the design variables, see [3].

The design problem is proposed to minimise biobjective functions as fan pumping power and junction temperature of a pin-fin heat sink. The fan pumping power is used to measure the consumption of electronic power, while the junction temperature determines heat sink thermal performance. Heat sink aspect ratio and space limit of the device are set to be design constraints. The multiobjective design problem of PFHS can be written as follows.

Objective functions:

$$\begin{aligned} &\min_{\mathbf{x}} \{T_j, P_{\text{fan}}\}, \\ &T_j = T_a + QR_{\text{hs}}, \\ &P_{\text{fan}} = \frac{\dot{m}_a \Delta P}{\rho_a}. \end{aligned} \tag{4.1}$$

Design variable vector:

$$\mathbf{x} = [n_f, w_{\text{fin}}, w_{\text{hs}}, V_f, H_{1-16}, t_b]^T. \tag{4.2}$$

Constraints:

$$\begin{aligned} T_j - 355^\circ\text{K} \ &\leq \ 0, \\ 0.0025 \leq w_{\text{fin}} &\leq 0.005, \\ 4 \leq N_f &\leq 14, \\ 0.0025 \leq t_b &\leq 0.005, \\ 0.0 \leq H_{\text{fin}} &\leq 0.05, \\ 0.5 \leq V_f &\leq 1.0, \\ 0.03 \leq w_{\text{hs}} &\leq 0.06, \\ 0.0025 < s_{\text{fin}} &< 0.004, \end{aligned} \tag{4.3}$$

where T_j is junction temperature, P_{fan} is fan pumping power, Q is heat load, R_{hs} is heat sink thermal resistant, ΔP is pressure drop across the heat sink, ρ_a is air density, and $\dot{m}_a$ is air mass flow rate.

The continuity, momentum, and energy equations for steady-state forced convection in a Newtonian, constant properties fluid without heat generation can be written as

$$\begin{aligned} \nabla \cdot \vec{V} &= 0, \\ \vec{V} \cdot \nabla \vec{V} &= -\frac{1}{\rho_a} \nabla P + \nu \nabla^2 \vec{V}, \\ \vec{V} \cdot \nabla T &= \alpha \nabla^2 T, \end{aligned} \tag{4.4}$$

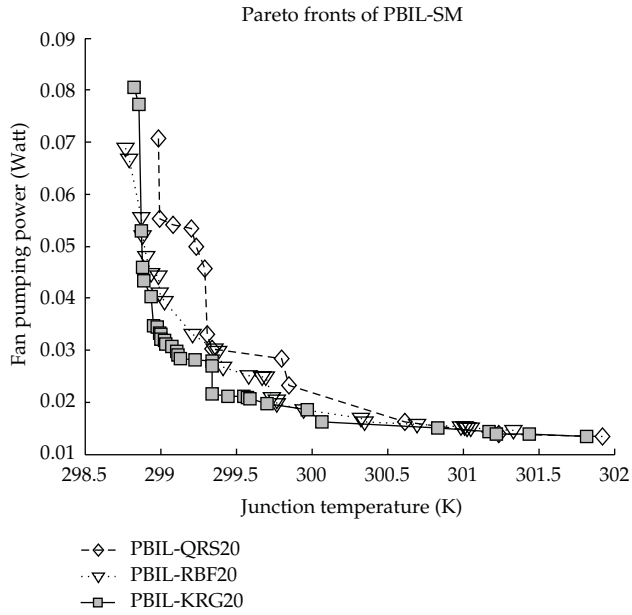

Figure 5: Pareto fronts from surrogate-assisted PBILs.

where $\vec{V}$ is fluid velocity, T is temperature, α is thermal conductivity, and ν is kinematic viscosity.

These are the governing equations for thermofluid analysis of the forced convection in the pin-fin heat sink. During the optimisation process, the three equations are handled by means of finite volume analysis, which is one of the most powerful numerical methods for computational fluid dynamics. The assumptions for the analysis are as follows.

(i) Fluid flow being laminar and steady.

(ii) Constant material thermophysical properties of both air and solid material.

(iii) Uniform inlet air velocity.

(iv) Uniform heat flux throughout the entire base plate bottom surface.

The heat sink body is made of aluminium. The physical properties of the solid and fluid are given in [1, 2]. The ambient temperature is set to be 298 K.

The vector of design variables $\mathbf{x}$ has 21 elements. SI units are used in the design objectives and constraints unless otherwise specified. In this work, 30 sampling points are created using a LHS technique, while PBIL with 100 population size and 200 generations is performed with surrogate-based function evaluations. Then, 25 design solutions from the surrogate optimisation are taken as initial solutions for a common PBIL, which is used for further exploring the nondominated front with 25 population size and 19 generations. This means that the proposed surrogate-assisted PBIL takes $30 + 25 \times 20 = 530$ actual function evaluations. For the original PBIL without using a surrogate model, the population size is set to be 25 while the number of generations is set to be 35. This implies that the nonsurrogate PBIL uses $25 \times 35 = 875$ actual function evaluations.

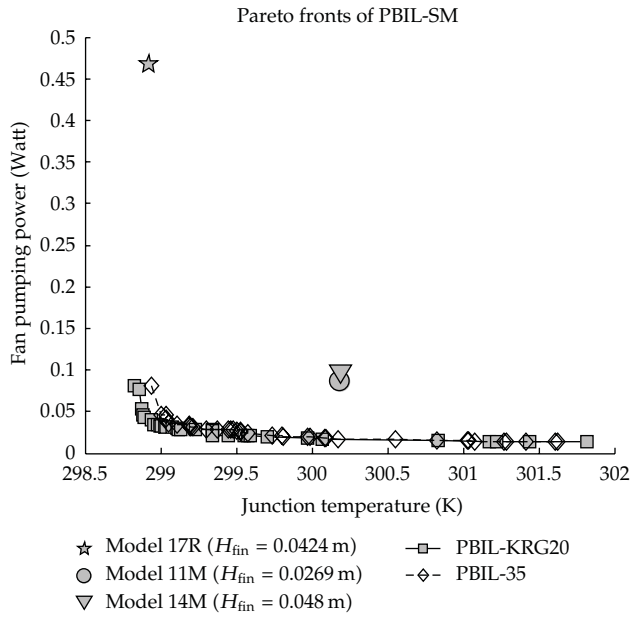

Figure 6: PBIL-KRG20 versus PBIL35.

5. Results and Discussion

Figure 5 displays nondominated fronts obtained from the various surrogate-assisted PBILs, which are defined as PBIL-QRS, PBIL-RBF, and PBIL-KRG for hybrid PBILs using a quadratic response surface model, a radial-basis function interpolation technique, and a Kriging model respectively. It can be clearly seen that the front obtained by using PBIL-KRG is superior to the others while the second best is PBIL-RBF.

The best front from the hybrid approach is then compared with that obtained from using the nonsurrogate PBIL (termed as PBIL-35) as shown in Figure 6. Apart from the two nondominated fronts, real heat sinks currently used in the real world are modelled where there junction temperature and fan pumping power values are calculated. The real heat sinks which have cylindrical pin fins include the following.

(i) Model 17R with 0.0635 m heat sink width, constant 0.0424 m fin height, 0.0033 m fin diameter, 0.0127 m heat sink base thickness, and 14 × 14 fins.

(ii) Model 11M with 0.0508 m heat sink width, constant 0.0269 m fin height, 0.0033 m fin diameter, 0.0048 m heat sink base thickness, and 61 fins.

(iii) Model 14M with 0.0508 m heat sink width, constant 0.0480 m fin height, 0.0033 m fin diameter, 0.0048 m heat sink base thickness, and 61 fins.

The first model is termed a dense pin fin heat sink, while the others are called a sparse pin fin heat sink. The models are simulated with an inlet air velocity 0.5 m/s and constant heat load 120 watts being applied at the bottom of the heat sink base. Based on the dominance theory, the design solutions obtained from PBIL-KRG and nonsurrogate PBIL are far superior to those real heat sinks.

The zoom-in of Figure 6 is given in Figure 7 so as to compare PBIL-KRG and PBIL-35. It can be seen that the results obtained from using the hybrid PBIL is overall superior to its

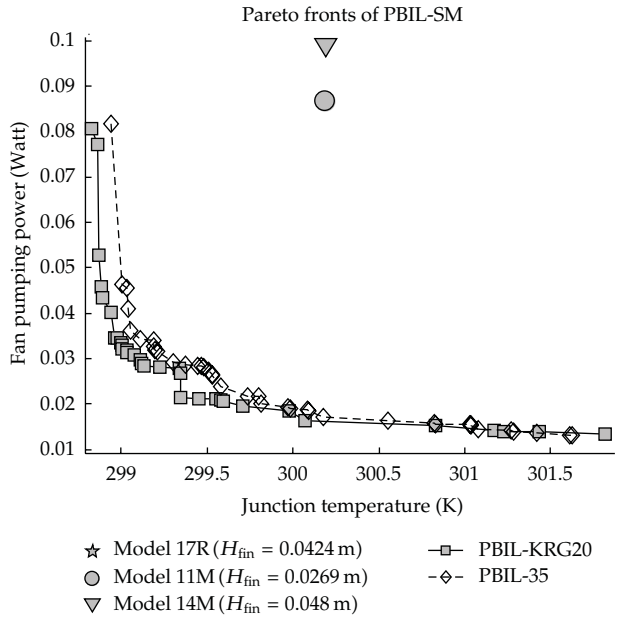

Figure 7: PBIL-KRG20 versus PBIL35 zoom-in of Figure 6.

Table 1: Hypervolume comparison (reference point is [303, 0.1]).

Optimiser	Hypervolume
PBIL-KRG20	0.42131
PBIL-RBF20	0.41935
PBIL-QRS20	0.39659
PBIL35	0.41183

Table 2: Probability vectors and their corresponding populations.

Population 1				Population 2				Population 3			
0	0	1	0,	0	1	0	1,	1	1	0	1
1	0	0	1,	1	1	1	0,	0	0	0	1
1	1	1	0,	0	0	0	1,	1	1	0	1
0	1	0	1,	0	0	0	0,	0	1	1	0

Probability vectors [0.5, 0.5, 0.5, 0.5] [0.25, 0.5, 0.25, 0.5] [0.5, 0.75, 0.25, 0.75].

nonsurrogate counterpart. This is confirmed by the quantitative assessment in Table 1. From the table, the hypervolume values of the Pareto fronts plotted in Figures 5 and 7 are computed where the reference point is set to be [303 K, 0.1 Watt]. Based on its definition, the larger hypervolume means the better Pareto or nondominated front. Two hybrid approaches PBIL-KRG and PBIL-RBF can surpass the original PBIL although the later uses 345 more actual function evaluations. Some selected design solutions from the PBIL-KRG front are plotted in Figure 8. It is shown that the hybrid optimiser results in a variety of PFHS geometries.

Further investigation is made to examine the accuracy of the employed surrogate models. The 30 sampling points in the previous section is used to build three surrogate

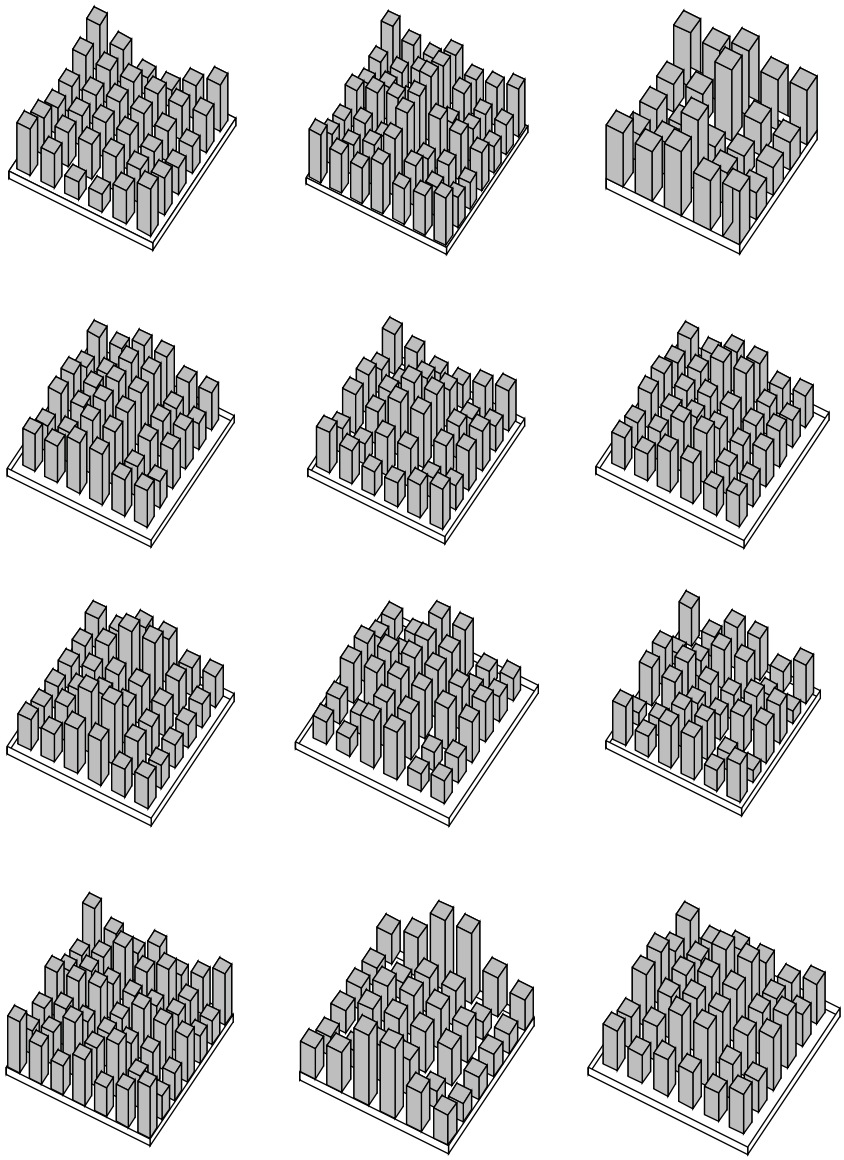

Figure 8: Selected PFHSs from the front of PBIL-KRG20.

models (QRS, RBF, and KRG). The second set of sampling points with 30 design solutions is generated, while its function values evaluated based on the surrogate models and finite volume analysis (actual function values) are determined. The boxplot in Figure 9 shows the error as an absolute value of the difference between actual function value and one from surrogate approximation. It can be seen that the most accurate surrogate model for both junction temperature and fan pumping power is KRG while the second best is RBF. This is coincident with the optimum results obtained from the hybrid PBILs.

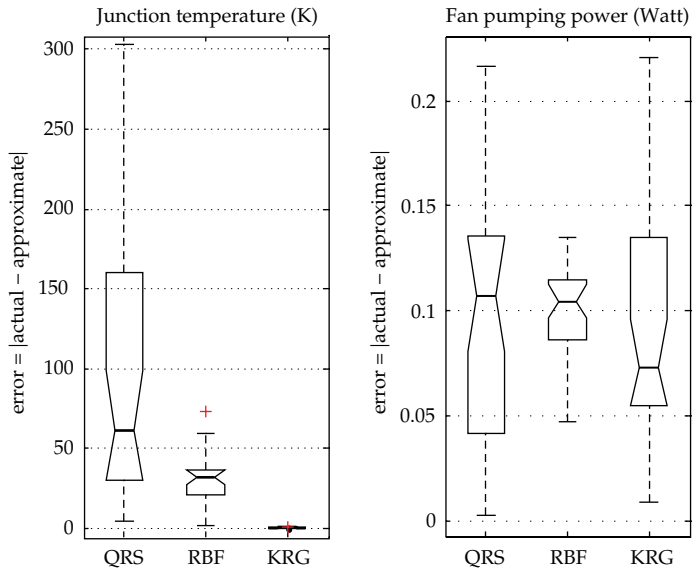

Figure 9: Accuracy assessment of the surrogate models.

6. Conclusions

This paper proposes hybrid PBIL using three well-known surrogate models as a quadratic response surface model, a radial-basis function interpolation technique, and a Kriging model. The hybridisation is carried out in such a way that a Latin hypercube sampling technique is employed to generate training points for constructing a surrogate model. Then, PBIL is used to tackle the design problem based upon the surrogate model prediction. Having obtained Pareto solutions from this phase, the Pareto front is then further improved by running PBIL with actual function evaluations for a few generations.

The hybrid PBILs along with the nonsurrogate PBIL are implemented on the multiobjective geometrical design of pin-fin heat sinks. The design problem is posed to find PFHS geometries while minimising its junction temperature and fan pumping power. The computational results reveal that the best performer is a surrogate-assisted PBIL using KRG. This is coincident with the accuracy investigation on predicting junction temperature and fan pumping power of the surrogate models. Design solutions obtained from performing the proposed design process are superior to those real heat sinks currently used in the real world. The proposed hybrid strategy is said to be efficient. Our future work is to study alternative hybrid strategy so that MOEA search performance for solving PFHS design is improved.

Acknowledgments

This research was supported by the Office of the Higher Education Commission, Thailand, under the program Strategic Scholarships for Frontier Research Network (CHE-PhD-THA), the Sustainable Infrastructure Research and Development Center (Khon Kaen University), and the Thailand Research Fund (TRF).

References

[1] S. Srisomporn and S. Bureerat, "Geometrical design of plate-fin heat sinks using hybridization of MOEA and RSM," *IEEE Transaction on Components and Packaging Technology*, vol. 31, no. 2, pp. 351–360, 2009.

[2] S. Bureerat and S. Srisomporn, "Optimum plate-fin heat sinks by using a multi-objective evolutionary algorithm," *Engineering Optimization*, vol. 42, no. 4, pp. 305–323, 2010.

[3] S. Kanyakam and S. Bureerat, "Multiobjective optimisation of a Pin-Fin heat sink using evolutionary algorithms," in *Proceedings of the Inverse Problems, Design and Optimization Symposium*, Joao Pessoa, Brazil, August 2010.

[4] S. Kanyakam and S. Bureerat, "Multiobjective evolutionary optimization of splayed pin-fin heat sink," *Engineering Applications of Computational Fluid Mechanics*, vol. 5, no. 4, pp. 553–565, 2011.

[5] S. Kanyakam and S. Bureerat, "Optimal design of a pin-fin heat sink using a surrogate-assisted multiobjective evolutionary algorithm," *Advanced Materials Research*, vol. 308–310, pp. 1122–1128, 2011.

[6] S. Manivannan, S. Prasanna, R. Arumugam, and N. Sudharsan, "Multi-objective optimization of flat plate heat sink using Taguchi-based Grey relation analysis," *The International Journal of Advanced Manufacturing Technology*, vol. 52, no. 5–8, pp. 739–749, 2010.

[7] W. A. Khan, J. R. Culham, and M. M. Yovanovich, "Optimization of pin-fin heat sinks in bypass flow using entropy generation minimization method," *Journal of Electronic Packaging, Transactions of the ASME*, vol. 130, no. 3, pp. 0310101–0310107, 2008.

[8] H. T. Chen, P. L. Chen, J. T. Horng, and Y. H. Hung, "Design optimization for pin-fin heat sinks," *Journal of Electronic Packaging, Transactions of the ASME*, vol. 127, no. 4, pp. 397–406, 2005.

[9] S. Y. Kim, J.-M. Koo, and A. V. Kuznetsov, "Effect of anisotropy in permeability and effective thermal conductivity on thermal performnce of an Aluminum foam heat sink," *Numerical Heat Transfer A*, vol. 40, no. 1, pp. 21–36, 2001.

[10] S. Y. Kim, J.-M. Koo, and A. V. Kuznetsov, "Optimization of pin-fin heat sinks using anisotropic local thermal nonequilibrium porous model in a jet impinging channel," *Numerical Heat Transfer A*, vol. 44, no. 8, pp. 771–787, 2003.

[11] J. G. Maveety and H. H. Jung, "Design of an optimal pin-fin heat sink with air impingment cooling," *IEEE Transactions on Components and Packaging Technologies*, vol. 25, no. 3, pp. 459–469, 2002.

[12] K. W. Park, P. K. Oh, and H. J. Lim, "The application of the CFD and Kriging method to an optimization of heat sink," *International Journal of Heat and Mass Transfer*, vol. 49, no. 19-20, pp. 3439–3447, 2006.

[13] S. N. Lophaven, H. B. Neilson, J. Sondergaard et al., "DACE a MATLAB kriging toolbox," Tech. Rep. IMM-TR-2002-12, Technical University of Denmark, 2002.

[14] S. Baluja, "Population-based incremental learning: a method for integrating genetic search based function optimization and competitive learning," Tech. Rep. CMU_CS_95_163, School of Computer Science, Carnagie Mellon University, Pittsburgh, Pa, USA, 1994.

[15] S. Bureerat and K. Sriworamas, "Population-based incremental learning for multiobjective optimisation," *Advances in Soft Computing*, vol. 39, pp. 223–232, 2007.

[16] S. Bandyopadhyay, S. Saha, U. Maulik, and K. Deb, "A simulated annealing-based multiobjective optimization algorithm: AMOSA," *IEEE Transactions on Evolutionary Computation*, vol. 12, no. 3, pp. 269–283, 2008.

[17] Y. Jin, "A comprehensive survey of fitness approximation in evolutionary computation," *Soft Computing*, vol. 9, pp. 3–12, 2005.

[18] R. L. Harder and R. N. Desmarais, "Interpolation using surface splines," *Journal of Aircraft*, vol. 9, no. 2, pp. 189–191, 1972.

[19] M. Farina and P. Amato, "Linked interpolation-optimization strategies for multicriteria optimization problems," *Soft Computing*, vol. 9, no. 1, pp. 54–65, 2005.

[20] Y. S. Ong, P. B. Nair, A. J. Keane, and K. W. Wong, "Surrogate-assisted evolutionary optimization frameworks for high-fidelity engineering design problems," in *Knowledge Incorporation in Evolutionary Computation, Studies in Fuzziness and Soft Computing*, Y. Jin, Ed., pp. 307–332, Springer, Berlin, Germany, 2004.

Hindawi Publishing Corporation
Journal of Applied Mathematics
Volume 2012, Article ID 161484, 11 pages
doi:10.1155/2012/161484

Research Article

Simulation of Thermal Flow Problems via a Hybrid Immersed Boundary-Lattice Boltzmann Method

J. Wu,[1] C. Shu,[2] and N. Zhao[1]

[1] *Department of Aerodynamics, College of Aerospace Engineering, Nanjing University of Aeronautics and Astronautics, Yudao Street, Nanjing 210016 Jiangsu, China*
[2] *Department of Mechanical Engineering, National University of Singapore, 10 Kent Ridge Crescent, Singapore 119260*

Correspondence should be addressed to J. Wu, wuj@nuaa.edu.cn

Received 20 December 2011; Revised 30 December 2011; Accepted 30 December 2011

Academic Editor: Fu-Yun Zhao

A hybrid immersed boundary-lattice Boltzmann method (IB-LBM) is presented in this work to simulate the thermal flow problems. In current approach, the flow field is resolved by using our recently developed boundary condition-enforced IB-LBM (Wu and Shu, (2009)). The nonslip boundary condition on the solid boundary is enforced in simulation. At the same time, to capture the temperature development, the conventional energy equation is resolved. To model the effect of immersed boundary on temperature field, the heat source term is introduced. Different from previous studies, the heat source term is set as unknown rather than predetermined. Inspired by the idea in (Wu and Shu, (2009)), the unknown is calculated in such a way that the temperature at the boundary interpolated from the corrected temperature field accurately satisfies the thermal boundary condition. In addition, based on the resolved temperature correction, an efficient way to compute the local and average Nusselt numbers is also proposed in this work. As compared with traditional implementation, no approximation for temperature gradients is required. To validate the present method, the numerical simulations of forced convection are carried out. The obtained results show good agreement with data in the literature.

1. Introduction

As a long-standing challenge in the computational fluid mechanics, the flow problems with complex geometry have been widely studied. In terms of grid applied, the numerical methods can be generally classified into two categories. In the traditional approach, the body-fitted mesh is employed to discretize the governing equation [1]. Thereafter, the boundary condition could be implemented directly. As a result, the solution of problems strongly

depends on the quality of generated mesh. Moreover, the mesh regeneration procedure is usually unavoidable when the object is not fixed. To relieve this cumbersome requirement, the alternative choice is to decouple the governing equation from the computational mesh. In this category, the most famous algorithm is the immersed boundary method (IBM) proposed by Peskin [2].

In IBM, the discretization of governing equation is performed on the Cartesian (Eulerian) mesh, and the boundary of object is represented through a set of Lagrangian points. Different from the body-fitted solver, the boundary condition in this method is depicted by introducing a body force (restoring force) into the governing equation, which replaces the effect of boundary on the surrounding flow field. Since the governing equation is independent of the boundary, IBM is extremely suitable for handling various flow problems with complex geometry.

To acquire accurate solution via IBM, the appropriate calculation of force density is of great importance. Up till now, there are several ways to fulfill this task. By treating the boundary as deformable with high stiffness, Peskin [2] firstly applied the Hook's law, associated with the use of free parameter, to compute the restoring force (named penalty method). Fadlun et al. [3] viewed the momentum equations as to be satisfied at boundary points and hence the force density could be subsequently computed (named direct forcing method). This approach has been widely used in current IBM application. Different from two methods introduced above, which are based on the Navier-Stokes (N-S) solver, another force calculation technique was proposed by Niu et al. [4] in the framework of lattice Boltzmann method (LBM) [5]. The concept of momentum exchange at the boundary is utilized in this approach (named momentum exchange method). Nonetheless, it should be stressed that the force density is calculated explicitly in the conventional methods. Consequently, the nonslip boundary condition cannot be guaranteed. Recently, we presented a boundary condition-enforced IB-LBM [6], in which the force density is raised from the velocity correction and is computed implicitly by enforcing the boundary condition. As compared to the conventional IBM, the nonslip boundary condition can be guaranteed in this method.

The idea of IBM has been extensively introduced into numerous isothermal flow problems. On the other hand, its application in thermal flow problems is limited and is still in progress. A few attempts have been made in this aspect [7–9]. Similar to the use of force density in isothermal flow problems, a heat source term is employed to meet the influence of boundary in thermal flow problems. However, same as the force calculation in conventional methods, the heat source term is computed explicitly in recent studies [7–9]. In this way, the thermal boundary condition cannot be accurately satisfied, which may affect the accuracy of solution. To address this problem, in this work, we develop a hybrid IB-LBM for simulation of thermal flow problems following the idea of velocity correction in [6]. In this method, the flow field is solved based on the IB-LBM in [6]. In the meanwhile, the temperature field is obtained by solving the conventional energy equation with additional heat source term, which is equivalent to temperature correction. With the temperature correction evaluated implicitly, the thermal boundary condition can be satisfied strictly. In addition, the Nusselt number is a crucial parameter in thermal flow problems. Based on the established temperature correction, in this paper, both the local and average Nusselt numbers can be efficiently computed. In this manner, the troublesome temperature gradient calculation at the boundary points could be eliminated. To validate the proposed algorithm, the forced convection from a stationary isothermal circular cylinder is simulated. The numerical results show good agreement with available data in the literature.

2. Methodology

2.1. Boundary Condition-Enforced Immersed Boundary-Lattice Boltzmann Method

For viscous incompressible flow problems with an immersed boundary, the governing equations in the framework of lattice Boltzmann equation (LBE) can be written as

$$f_\alpha(\mathbf{x}+\mathbf{e}_\alpha\delta t, t+\delta t) - f_\alpha(\mathbf{x},t) = -\frac{1}{\tau}\left(f_\alpha(\mathbf{x},t) - f_\alpha^{\mathrm{eq}}(\mathbf{x},t)\right) + F_\alpha\delta t, \tag{2.1}$$

$$F_\alpha = \left(1-\frac{1}{2\tau}\right)w_\alpha\left(\frac{\mathbf{e}_\alpha-\mathbf{u}}{c_s^2} + \frac{\mathbf{e}_\alpha\cdot\mathbf{u}}{c_s^4}\mathbf{e}_\alpha\right)\cdot\mathbf{f}, \tag{2.2}$$

$$\rho\mathbf{u} = \sum_\alpha \mathbf{e}_\alpha f_\alpha + \frac{1}{2}\mathbf{f}\delta t, \tag{2.3}$$

where f_α is the distribution function, f_α^{eq} is its corresponding equilibrium state, τ is the single relaxation parameter, $\mathbf{e}_\alpha$ is the lattice velocity, w_α are coefficients which depend on the selected lattice velocity model, and $\mathbf{f}$ is the force density which is distributed from the boundary force density. Here, the D2Q9 lattice velocity model is used, which is

$$\mathbf{e}_\alpha = \begin{cases} (0,0), & \alpha = 0, \\ (\pm1,0),(0,\pm1), & \alpha = 1\sim4, \\ (\pm1,\pm1), & \alpha = 5\sim8, \end{cases} \tag{2.4}$$

and the corresponding equilibrium distribution function is

$$f_\alpha^{\mathrm{eq}}(\mathbf{x},t) = \rho w_\alpha\left[1 + \frac{\mathbf{e}_\alpha\cdot\mathbf{u}}{c_s^2} + \frac{(\mathbf{e}_\alpha\cdot\mathbf{u})^2 - (c_s|\mathbf{u}|)^2}{2c_s^4}\right] \tag{2.5}$$

with $w_0 = 4/9$, $w_\alpha = 1/9$, ($\alpha = 1\sim4$), and $w_\alpha = 1/36$, ($\alpha = 5\sim8$). $c_s = 1/\sqrt{3}$ is the sound speed of this model. The relationship between the relaxation time and the kinematic viscosity of fluid is $\upsilon = (\tau - 0.5)c_s^2\delta t$.

In order to satisfy the nonslip boundary condition, the force density $\mathbf{f}$ in (2.2) and (2.3) should be set as unknown [6]. It can be calculated from the fluid velocity correction $\delta\mathbf{u}$. Furthermore, $\delta\mathbf{u}$ can be obtained from the boundary velocity correction $\delta\mathbf{u}_B$. The final expression for $\delta\mathbf{u}_B$ is

$$\mathbf{AX} = \mathbf{B}, \tag{2.6}$$

where

$$\mathbf{X} = \left\{ \delta\mathbf{u}_B^1, \delta\mathbf{u}_B^2, \ldots, \delta\mathbf{u}_B^m \right\}^T, \tag{2.7}$$

$$\begin{aligned} \mathbf{A} &= \begin{pmatrix} \delta_{11} & \delta_{12} & \cdots & \delta_{1n} \\ \delta_{21} & \delta_{22} & \cdots & \delta_{2n} \\ \vdots & \vdots & \ddots & \vdots \\ \delta_{m1} & \delta_{m2} & \cdots & \delta_{mn} \end{pmatrix} \begin{pmatrix} \delta_{11}^B & \delta_{12}^B & \cdots & \delta_{1m}^B \\ \delta_{21}^B & \delta_{22}^B & \cdots & \delta_{2m}^B \\ \vdots & \vdots & \ddots & \vdots \\ \delta_{n1}^B & \delta_{n2}^B & \cdots & \delta_{nm}^B \end{pmatrix}, \\ \mathbf{B} &= \begin{pmatrix} \mathbf{U}_B^1 \\ \mathbf{U}_B^2 \\ \vdots \\ \mathbf{U}_B^m \end{pmatrix} - \begin{pmatrix} \delta_{11} & \delta_{12} & \cdots & \delta_{1n} \\ \delta_{21} & \delta_{22} & \cdots & \delta_{2n} \\ \vdots & \vdots & \ddots & \vdots \\ \delta_{m1} & \delta_{m2} & \cdots & \delta_{mn} \end{pmatrix} \begin{pmatrix} \mathbf{u}_1^* \\ \mathbf{u}_2^* \\ \vdots \\ \mathbf{u}_n^* \end{pmatrix}. \end{aligned} \tag{2.8}$$

Here, m is the number of Lagrangian (boundary) points, and n is the number of surrounding Eulerian points. $\delta\mathbf{u}_B^l$ $(l = 1, 2, \ldots, m)$ is the unknown velocity correction vector at the boundary points. $\delta_{ij} = D_{ij}(\mathbf{x}_{ij} - \mathbf{X}_B^l)\Delta x \Delta y$ and $\delta_{ij}^B = D_{ij}(\mathbf{x}_{ij} - \mathbf{X}_B^l)\Delta s_l$. $D_{ij}(\mathbf{x}_{ij} - \mathbf{X}_B^l)$ is the delta function, which is expressed as

$$\begin{aligned} D_{ij}\left(\mathbf{x}_{ij} - \mathbf{X}_B^l\right) &= \delta\left(x_{ij} - X_B^l\right)\delta\left(y_{ij} - Y_B^l\right), \\ \delta(r) &= \begin{cases} \dfrac{1}{4h}\left(1 + \cos\left(\dfrac{\pi|r|}{2h}\right)\right), & |r| \le 2h, \\ 0, & |r| > 2h, \end{cases} \end{aligned} \tag{2.9}$$

and Δs_l is the arc length of boundary element. $\mathbf{U}_B^l$ is the boundary velocity. The intermediate fluid velocity $\mathbf{u}^*$ is calculated by

$$\mathbf{u}^* = \frac{1}{\rho}\sum_{\alpha} \mathbf{e}_\alpha f_\alpha. \tag{2.10}$$

By solving equation system (2.6), the unknown variables $\delta\mathbf{u}_B^l$ can be obtained. After that, the fluid velocity correction $\delta\mathbf{u}$ can be calculated by

$$\delta\mathbf{u} = \sum_{l} \delta\mathbf{u}_B^l D_{ij}\left(\mathbf{x}_{ij} - \mathbf{X}_B^l\right)\Delta s_l. \tag{2.11}$$

As shown in (2.3), the relationship between the force density $\mathbf{f}$ and the fluid velocity correction $\delta\mathbf{u}$ can be written as

$$\mathbf{f} = \frac{2\rho\delta\mathbf{u}}{\delta t}. \tag{2.12}$$

In the LBM, the macroscopic variables such as density and pressure are calculated by

$$\rho = \sum_{\alpha} f_{\alpha}, \qquad P = c_s^2\rho. \tag{2.13}$$

2.2. *Implicit Temperature Correction for Energy Equation*

After the flow field is accurately solved through the boundary condition-enforced IB-LBM [6], the temperature field can be obtained by using the conventional energy equation with additional heat source term, which can be written as

$$\rho c_p\left(\frac{\partial T}{\partial t} + (\mathbf{u}\cdot\nabla)T\right) = k\nabla^2 T + q, \tag{2.14}$$

where T is the temperature, c_p is the specific heat of the fluid, k is the thermal conductivity of the fluid, and q is the heat source density distributed from the boundary heat flux.

To solve (2.14), the fractional step technique is used. First, the energy equation without heat source density is solved, which is called Predictor step:

$$\rho c_p\left(\frac{\partial T}{\partial t} + (\mathbf{u}\cdot\nabla)T\right) = k\nabla^2 T. \tag{2.15}$$

The solution of (2.15) is regarded as intermediate temperature T^*. In the second step, or named Corrector step, the following equation is solved:

$$\rho c_p\frac{\partial T}{\partial t} = q. \tag{2.16}$$

Here, (2.16) means the effect of heat source on temperature field. Using the Euler explicit scheme, $\partial T/\partial t$ can be rewritten as $T^{n+1} - T^*/\delta t = \delta T/\delta t$, where T^{n+1} is the required temperature at next time step. Therefore, (2.16) becomes

$$q = \rho c_p\frac{\delta T}{\delta t}, \tag{2.17}$$

where δT is the temperature correction which determines the unknown variable q. It means that to calculate heat source term is equivalent to correcting the temperature field near the boundary. Similar to the implementation of velocity correction in IB-LBM [6], δT can further

be calculated from the boundary temperature correction δT_B. By enforcing the constant temperature boundary condition, δT_B can computed from the following equation system:

$$\mathbf{CY} = \mathbf{D}, \tag{2.18}$$

where

$$\mathbf{Y} = \left\{\delta T_B^1, \delta T_B^2, \ldots, \delta T_B^m\right\}^T, \tag{2.19}$$

$$\begin{aligned}
\mathbf{C} &= \begin{pmatrix} \delta_{11} & \delta_{12} & \cdots & \delta_{1n} \\ \delta_{21} & \delta_{22} & \cdots & \delta_{2n} \\ \vdots & \vdots & \ddots & \vdots \\ \delta_{m1} & \delta_{m2} & \cdots & \delta_{mn} \end{pmatrix} \begin{pmatrix} \delta_{11}^B & \delta_{12}^B & \cdots & \delta_{1m}^B \\ \delta_{21}^B & \delta_{22}^B & \cdots & \delta_{2m}^B \\ \vdots & \vdots & \ddots & \vdots \\ \delta_{n1}^B & \delta_{n2}^B & \cdots & \delta_{nm}^B \end{pmatrix}, \\
\mathbf{D} &= \begin{pmatrix} T_B^1 \\ T_B^2 \\ \vdots \\ T_B^m \end{pmatrix} - \begin{pmatrix} \delta_{11} & \delta_{12} & \cdots & \delta_{1n} \\ \delta_{21} & \delta_{22} & \cdots & \delta_{2n} \\ \vdots & \vdots & \ddots & \vdots \\ \delta_{m1} & \delta_{m2} & \cdots & \delta_{mn} \end{pmatrix} \begin{pmatrix} T_1^* \\ T_2^* \\ \vdots \\ T_n^* \end{pmatrix}.
\end{aligned} \tag{2.20}$$

Here, T_B^l is the specified boundary temperature. The parameters m, n, δ_{ij}, and δ_{ij}^B have the same meaning as those in equation system (2.6). After δT_B is obtained from equation system (2.18), the temperature correction δT can be calculated through

$$\delta T = \sum_l \delta T_B^l D_{ij}\left(\mathbf{x}_{ij} - \mathbf{X}_B^l\right)\Delta s_l. \tag{2.21}$$

Consequently, the corrected temperature can be computed by

$$T = T^* + \delta T. \tag{2.22}$$

2.3. Local and Average Nusselt Number Evaluation

In thermal flow problems, the Nusselt number is an important measurement parameter. The local Nusselt number Nu on the surface of boundary is defined as

$$\mathrm{Nu}(\mathbf{X}_B, t) = \frac{h(\mathbf{X}_B, t)L_c}{k}, \tag{2.23}$$

where h is the local convective heat transfer coefficient and L_c is the characteristic length. According to Newton's cooling law and Fourier's law, the heat conducted away from the boundary should be equal to the heat convection from the boundary, that is,

$$-k\frac{\partial T}{\partial n}(\mathbf{X}_B, t) = h(\mathbf{X}_B, t)(T_B - T_\infty), \tag{2.24}$$

where T_∞ is the free stream temperature. Substituting (2.24) into (2.23) gives

$$\mathrm{Nu}(\mathbf{X}_B, t) = -\frac{L_c}{T_B - T_\infty}\frac{\partial T}{\partial n}(\mathbf{X}_B, t). \tag{2.25}$$

Further averaging over the entire boundary, we can have the surface overall mean Nusselt number $\overline{\mathrm{Nu}}$

$$\overline{\mathrm{Nu}} = \frac{1}{L}\int \mathrm{Nu}\, ds = -\frac{L_c}{(T_B - T_\infty)L}\int \frac{\partial T}{\partial n}(\mathbf{X}_B, t) ds, \tag{2.26}$$

where L is the total length of boundary. Usually, the average Nusselt number can be used to estimate the rate of heat transfer from the heated surface.

As shown in (2.25) and (2.26), to evaluate the local and average Nusselt numbers, the calculation of temperature gradient at the boundary point is required. Since the temperature is located at the Eulerian mesh which is not coincided with boundary, we cannot calculate the boundary temperature derivatives directly. On the other hand, according to the Fourier's law, we can have the following expression for heat flux on the boundary Q:

$$Q(\mathbf{X}_B, t) = -k\frac{\partial T}{\partial n}(\mathbf{X}_B, t). \tag{2.27}$$

At the same time, similar to (2.17), the boundary heat flux can be calculated using the boundary temperature correction

$$Q = \rho c_p \frac{\delta T_B}{\delta t}. \tag{2.28}$$

Substituting (2.27) and (2.28) into (2.25) and (2.26), the expressions for the local and average Nusselt numbers can be rewritten as

$$\mathrm{Nu} = \frac{\rho c_p L_c}{k\delta t(T_B - T_\infty)}\delta T_B, \tag{2.29}$$

$$\overline{\mathrm{Nu}} = \frac{\rho c_p L_c}{k\delta t(T_B - T_\infty)L}\sum_l \delta T_B^l \Delta s_l. \tag{2.30}$$

As can be seen from (2.29) and (2.30), the local and average Nusselt numbers can be easily calculated by using the solved boundary temperature correction, which avoids the temperature gradient computation on the boundary.

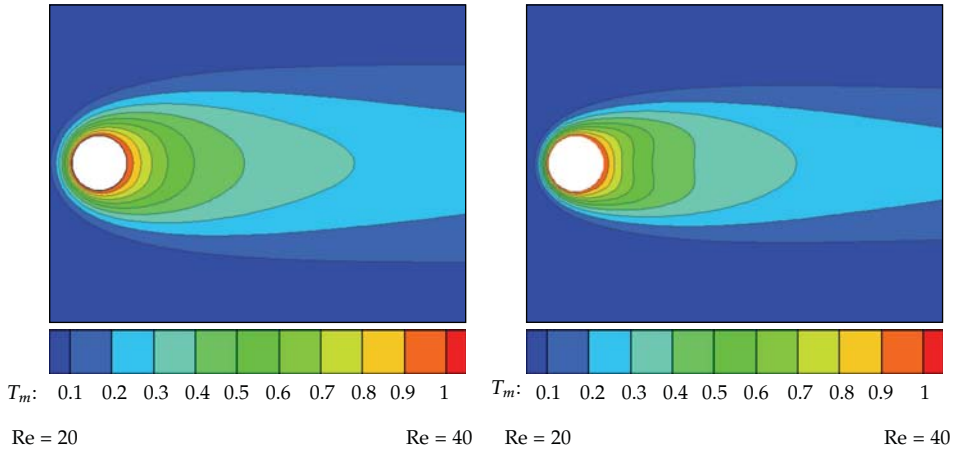

Figure 1: Temperature contours for steady forced convection from a stationary circular cylinder.

3. Results and Discussion

As a benchmark case, the forced convection from a stationary circular cylinder has been extensively simulated to validate the numerical methods. Both the experimental and numerical results are available in the literature [10–12]. To characterize this thermal flow problem, two nondimensional parameters are used: the Reynolds number $\mathrm{Re} = \rho U_\infty D/\mu$ and Prandtl number $\mathrm{Pr} = \mu c_p/k$. Here, U_∞ is the free stream velocity, D is the cylinder diameter, and μ is the dynamic viscosity. In current simulation, the Prandtl number is fixed at $\mathrm{Pr} = 0.7$. Meanwhile, several low Reynolds numbers are selected: $\mathrm{Re} = 20$, 40 (steady flow), and 80, 150 (unsteady flow). Since this is a one-way interaction problem, the velocity field can influence the temperature field while cannot be affected by the temperature field. As the developed IB-LBM can accurately simulate velocity field [6], we only focus on the temperature field in this case.

For the steady flow simulation, the computational domain is $60D \times 40D$ with the nonuniform mesh size of 321×241. The cylinder is located at $(20D, 20D)$. The region around the cylinder is $1.2D \times 1.2D$ with a finest and uniform mesh size of 49×49. To apply the IB-LBM on nonuniform mesh, the Taylor series expansion and least-squares-based LBM [13] are utilized. Figure 1 shows the temperature contours at $\mathrm{Re} = 20$ and 40. It can be seen from the figure that the isotherms cluster heavily in the front part of cylinder. When the Reynolds number is increased, the behavior of isotherm clustering is strengthened. The clustering of isotherm indicates that the temperature gradient is large there. As a result, the heat transfer rate near the front of cylinder is much larger than other regions. This phenomenon can be further verified via the local Nusselt number distribution on the surface of cylinder, as shown in Figure 2 for the case of $\mathrm{Re} = 20$. Without evaluation of temperature gradient on the boundary point, the local Nusselt number can be easily computed from the solved boundary temperature correction, as shown in (2.29). To make comparison, the result of Bharti et al. [12] is also involved. In this figure, $\theta = 0°$ means the front stagnation point of cylinder. From Figure 2, it can be found that the value of local Nusselt number located at $\theta = 0°$ is maximum and it decreases monotonously with respect to θ. Also can be seen from the figure is that the result of current simulation shows good agreement with that of Bharti et al. [12].

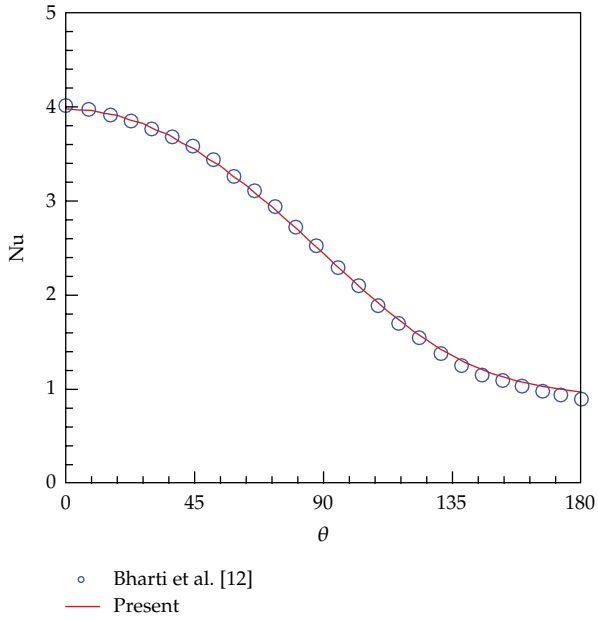

Figure 2: Local Nusselt number distribution on the surface of cylinder at Re = 20.

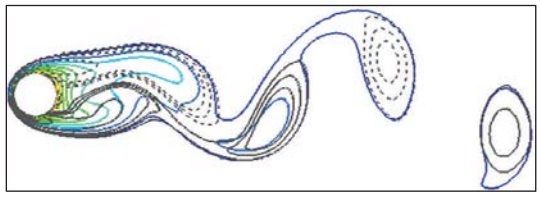

Re = 80

(a)

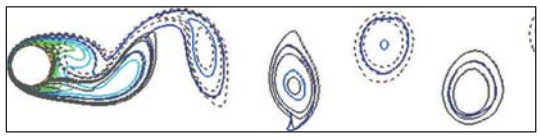

Re = 150

(b)

Figure 3: Instantaneous isotherms (colorful) and vorticity contours (gray) for unsteady forced convection from a stationary cylinder.

For the unsteady flow simulation, the computational domain is $50D \times 40D$ with the mesh size of 401×301. The region around the cylinder keeps $1.2D \times 1.2D$ with a uniform mesh size of 97×97. The cylinder is still located at $(20D, 20D)$. Figure 3 plots the isotherms as well as vorticity contours at Re = 80 and 150. The regular vortex shedding occurs at these two Reynolds numbers. Concurrently, the isotherms lose symmetry and start to display shedding behavior, which synchronously moves downstream with vortex.

To illustrate the performance of average Nusselt number calculation by using (2.30), the obtained numerical results for all Reynolds numbers considered here are shown in

Table 1: Nusselt number comparison at different Reynolds numbers.

References	Cases	Nu
Lange et al. [11]	Re = 20	2.409
	Re = 40	3.281
	Re = 80	4.571
	Re = 150	6.396
Bharti et al. [12]	Re = 20	2.465
	Re = 40	3.283
	Re = 80	—
	Re = 150	—
Present	Re = 20	2.472
	Re = 40	3.281
	Re = 80	4.611
	Re = 150	6.432

Table 1. To compare with available results in the literature, the numerical results of Lange et al. [11] and Bharti et al. [12] are also listed in the table. It is clear that the results from current method basically agree well with the reference data. Besides, the value of average Nusselt number increases with Reynolds number as expected.

4. Conclusion

In this paper, a hybrid immersed boundary-lattice Boltzmann method is developed to simulate the heat transfer problems. Employing the newly proposed IB-LBM [6], the nonslip boundary condition is enforced in simulation, and thus the velocity field can be accurately simulated. In the meanwhile, the temperature field is resolved by using the conventional energy equation with additional heat source term which mimics the influence of boundary on temperature field. Similar to the idea of velocity correction in [6], the heat source term is equivalent to the temperature correction and is set as unknown. By enforcing the thermal boundary condition, this unknown variable can be determined. Furthermore, utilizing the relationship between the temperature correction and heat flux, a simple approach for local and average Nusselt number evaluation is proposed. Different from the conventional way, there is no requirement for temperature gradient calculation.

The efficiency and capability of developed method as well as way to calculate the local and average Nusselt numbers are illustrated by the simulation of forced convection problems. The obtained numerical results show good agreement with available data in the literature. It is demonstrated that the present method has a promising potential for solving thermal flow problems with complex geometry.

References

[1] C. W. Hirt, A. A. Amsden, and J. L. Cook, "An arbitrary Lagrangian-Eulerian computing method for all flow speeds," *Journal of Computational Physics*, vol. 14, no. 3, pp. 227–253, 1974.

[2] C. S. Peskin, "Numerical analysis of blood flow in the heart," *Journal of Computational Physics*, vol. 25, no. 3, pp. 220–252, 1977.

[3] E. A. Fadlun, R. Verzicco, P. Orlandi, and J. Mohd-Yusof, "Combined immersed-boundary finite-difference methods for three-dimensional complex flow simulations," *Journal of Computational Physics*, vol. 161, no. 1, pp. 35–60, 2000.

[4] X. D. Niu, C. Shu, Y. T. Chew, and Y. Peng, "A momentum exchange-based immersed boundary-lattice Boltzmann method for simulating incompressible viscous flows," *Physics Letters A*, vol. 354, no. 3, pp. 173–182, 2006.

[5] S. Succi, *The Lattice Boltzmann Equation, For Fluid Dynamics and Beyond*, Oxford University Press, 2001.

[6] J. Wu and C. Shu, "Implicit velocity correction-based immersed boundary-lattice Boltzmann method and its applications," *Journal of Computational Physics*, vol. 228, no. 6, pp. 1963–1979, 2009.

[7] B. S. Kim, D. S. Lee, M. Y. Ha, and H. S. Yoon, "A numerical study of natural convection in a square enclosure with a circular cylinder at different vertical locations," *International Journal of Heat and Mass Transfer*, vol. 51, no. 7-8, pp. 1888–1906, 2008.

[8] D. L. Young, Y. J. Jan, and C. L. Chiu, "A novel immersed boundary procedure for flow and heat simulations with moving boundary," *Computers & Fluids*, vol. 38, no. 6, pp. 1145–1159, 2009.

[9] Z. Wang, J. Fan, K. Luo, and K. Cen, "Immersed boundary method for the simulation of flows with heat transfer," *International Journal of Heat and Mass Transfer*, vol. 52, no. 19-20, pp. 4510–4518, 2009.

[10] A. P. Hatton, D. D. James, and H. W. Swire, "Combined forced and natural convection with low-speed air flow over horizontal cylinders," *Journal of Fluid Mechanics*, vol. 42, pp. 14–31, 1970.

[11] C. F. Lange, F. Durst, and M. Breuer, "Momentum and heat transfer from cylinders in laminar crossflow at $10^{-4} \leq Re \leq 200$," *International Journal of Heat and Mass Transfer*, vol. 41, no. 22, pp. 3409–3430, 1998.

[12] R. P. Bharti, R. P. Chhabra, and V. Eswaran, "A numerical study of the steady forced convection heat transfer from an unconfined circular cylinder," *Heat and Mass Transfer*, vol. 43, no. 7, pp. 639–648, 2007.

[13] C. Shu, X. D. Niu, and Y. T. Chew, "Taylor-series expansion and least-squares-based lattice Boltzmann method: two-dimensional formulation and its applications," *Physical Review E*, vol. 65, no. 3, Article ID 036708, pp. 1–13, 2002.